

Intrabeam scattering in the LHC

Tom Mertens



CERN-THESIS-2011-042
17/06/2011



Departamento de Física e Astronomia
Faculdade de Ciências da Universidade do Porto
June/2011

Intrabeam scattering in the LHC

Relatório de Estágio do Mestrado em Física

In collaboration with CERN

Tom Mertens

Supervisors:

Miguel Sousa Da Costa

Departamento de Física e Astronomia

Faculdade de Ciências da Universidade do Porto

John Jowett

BE-ABP-LCU, CERN, Geneva

Departamento de Física e Astronomia
Faculdade de Ciências da Universidade do Porto

June/2011

Intrabeam scattering in the LHC

Tom Mertens

ABSTRACT. Intrabeam Scattering (IBS) is the process where particles within an accelerator beam elastically scatter off each other. The effect of IBS is not to be confused with the Coulomb repulsion due to the fields generated by the other particles in the beam. The Coulomb repulsion effects are referred to as space-charge effects in Accelerator Physics and become less important than IBS at high energies because of the $\frac{1}{\gamma^2}$ that occurs in the space-charge equations making IBS one of the most important causes of beam size growth. At high energies (for example at 7 TeV or the LHC nominal operation energy) IBS effects are counteracted by Radiation Damping effects, in some cases leading to decrease in beam sizes instead of beam growth. But at the time of writing the operation energies were still low enough to neglect Radiation Damping Effects in comparison with IBS effects (Radiation Lifetimes were a factor five to ten higher than the IBS Lifetimes in the cases presented at the end of this text). Because of its effect on beam size IBS is an important effect to consider in beam operation. In many cases, especially for heavy ions that have a large charge compared to protons, the IBS effect will be one of the main factors determining the beam lifetime and thus putting constraints on the beam operation. In this aspect it is important to have a good model for IBS to be able to predict what lifetimes can be expected for the beam under different circumstances.

In this text we will derive the equations for the IBS growth rates in the different planes that were presented in the article published by Bjorken and Mtingwa [14]. We will also give a short discussion of the other IBS models that were already used to simulate the IBS lifetimes in the LHC. Next to these models the Nagaitsev Model is introduced. Roderik Bruce and myself implemented this model in the simulation software during my internship at CERN. This Nagaitsev Model has the advantage that the calculations of the integrals, necessary for determining the IBS growth rates, can be done fairly quickly and the accuracy can be set in the software. A disadvantage of this model is that it does not take Vertical Dispersion into account.

After comparing the different models with each other on a test case we decided to use the Nagaitsev Model to do simulations and compared them with the data from the 2010 LHC operation. The comparison is mainly done for ions because there the IBS effect is the strongest, but in some sections I will deviate from that and also have a look at proton data. Future work is planned to compare simulations with proton data.

Simulations were done with a FORTRAN particle tracking code. This particle tracking software (PTS) was developed by Roderik Bruce (CERN/LUND university) and Mike Blaskiewicz (BNL) in collaboration with John Jowett (CERN) and was applied successfully to RHIC [4, 20] (Relativistic Heavy Ion Collider), it was also used to make predictions for the LHC.

Contents

Part 1. Accelerator Physics	9
0.1. List of abbreviations	10
Chapter 1. LHC: The machine	11
1.1. Introduction	11
1.2. General Layout	11
1.3. CERN Complex	13
Chapter 2. Transverse Beam Dynamics	15
2.1. The Coordinate System (Frenet-Serret)	15
2.2. Hamiltonian Mechanics	16
2.3. Magnetic Fields in the Frenet-Serret Coordinate System	18
2.4. Betatron Motion	20
2.5. Betatron Motion: Linear Approximation	20
2.6. Action-Angle Variables	26
2.7. Emittance considerations	27
2.8. The Dispersion Function	28
2.9. Magnet Errors : An example	30
2.10. Chromaticity Q'	32
2.11. Toy model accelerator	33
2.12. Summary	34
Chapter 3. Longitudinal Dynamics	37
3.1. Basic equations dynamics equation	37
3.2. The Accelerating Component: The RF Cavity	37
3.3. Transit Time Factor	37
3.4. Phase-Stability	38
3.5. Momentum Compaction Factor, Phase-slip Factor and the Transition Energy	39
3.6. Equations of motion	41
3.7. Synchrotron Hamiltonian and Synchrotron motion	43
3.8. Synchrotron symplectic mapping equations	47
3.9. Summary	47
Part 2. Intrabeam scattering models	49
Chapter 4. The Bjorken-Mtingwa Model	51
4.1. The particle distribution and used notations	51
4.2. Transition Rate for Two-Body Scattering	52
4.3. Rate equations	56
4.4. Growth Rates	64
Chapter 5. Alternatives to the Bjorken-Mtingwa Model	67
5.1. Introduction	67
5.2. The Piwinski Model	67

5.3. The Bane Model	69
5.4. The Nagaitsev Model	70
5.5. The Zimmerman Model	72
Part 3. Simulations	77
Chapter 6. Simulations based on MAD-X	79
6.1. Introduction MAD-X	79
6.2. Mathematica and MAD-X: Madtomma	80
6.3. IBS Simulations with MAD-X	81
6.4. Data Extraction from Measurement Devices and related issues	83
6.5. Comparing the simulations with data	89
6.6. Conclusions	92
Chapter 7. Particle Tracking Simulations	101
7.1. Introduction	101
7.2. Simulations	101
7.3. Comparing IBS algorithms	102
7.4. Comparing the simulations with data	102
7.5. Conclusions	105
Chapter 8. Final conclusions and acknowledgments	111
8.1. Summary and Final Conclusions	111
8.2. Acknowledgments	111
Bibliography	113
Part 4. Appendix	115
Appendix A. Canonical transformations	117
Appendix B. Betatron motion for off-momentum particles	119
Appendix C. Expression for the dispersion function	121
Appendix D. Simulations	123
D.1. Example of a Sequence File	123
D.2. Example of a MAD-X program	124
D.3. Part of Twiss.out File	124
D.4. Example of an input file for the PTS	126
D.5. Comparing simulation models (beam 2)	128
D.6. Additional comparisons of data with PTS simulations	129

Part 1

Accelerator Physics

0.1. List of abbreviations

GT	= Growth Times
GR	= Growth Rates
IBS	= Intrabeam Scattering
IR	= Insertion Region
IP	= Interaction Point
RF	= Radio Frequency
LSS	= Long Straight Section
DSL	= Dispersion Surpression Left
DSR	= Dispersion Surpression Righ
PTS	= Particle Tracking Simulation/Software
RHIC	= Relativistic Heavy Ion Collider
GeV	= Giga electron Volt
TeV	= Tera electron Volt
RMS	= Root Mean Square
MB	= Main Bend (dipole)
MQ	= Main Quadrupole
MQF	= Main Quadrupole Focusing
MQD	= Main Quadrupole Defocusing
BM	= Bjorken-Mtingwa
QFT	= Quantum Field Theory
CMS	= Center of Mass System
BQM	= Beam Quality Monitor
FBCT	= Fast Beam Current Transformer
BSRTS	= Beam Synchrotron Light Monitor
LHC	= Large Hadron Collider

CHAPTER 1

LHC: The machine

1.1. Introduction

The LHC is one of the latest additions to the available machines for high energy particle physics, originally designed as a Proton-Proton collider it also allows Lead-Lead collisions (and in a later stage might allow for Electron-Proton collisions and Proton-Lead collisions). This machine currently active at CERN (The European Organization for Nuclear Research) is built to create colliding beams of particles at energies (7 TeV [2]) and with luminosities ($1.0 \times 10^{34} [cm^{-2}s^{-1}]$ [2]) unavailable to physicists before. To achieve these high energies and high luminosities many challenges need(ed) to be overcome. Before giving an introduction in Accelerator Physics a short overview of the LHC as a machine is given in the following sections.

1.2. General Layout

The LHC is more or less a circular machine with a circumference of 26658.8832 meters, but only about a third of the ring is used for bending the particles in a circular trajectory. The rest of the ring is used for experimental areas, measurement devices and so on. Important to notice in table 1 is that there are eight insertion regions (IR) numbered from one to eight.

IR	Description
1	ATLAS, A Toroidal LHC ApparatuS
2	ALICE, A Large Ion Collider Experiment + injection Beam 1
3	Momentum cleaning (for machine protection)
4	RF-cavities (for acceleration and longitudinal focusing)
5	CMS, Compact Muon Solenoid
6	Beam dump: location for dumping the beam in case of failure
7	Betatron Cleaning (for machine protection)
8	LHC-b, study of CP violation in B hadron decays + injection Beam 2

TABLE 1. Interaction regions

The LHC can be considered to consist of eight octants that are similar in design (see Figure 1.2.1). Each octant is separated by an arc section used to bend the particles trajectories. The Dispersion Suppressor Left (DSL) and Dispersion Suppressor Right (DSR) sections are used to suppress the Dispersion in the Long Straight Sections (LSS, see section 2.8 for a discussion and definition of Dispersion). Each IR has its own specific design adapted to its purpose .



FIGURE 1.2.2. Left side IR2 (ALICE) [2]

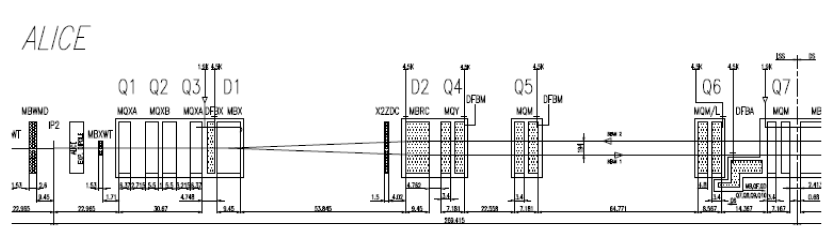


FIGURE 1.2.3. Right side IR2 (ALICE)[2]

1.3. CERN Complex

Particles are not accelerated from their production energy to their maximum energy in the LHC, they are injected in the LHC at an energy of 450 GeV. This means that particles will need to be accelerated in other accelerators before being injected in the LHC. Figure 1.3.1 shows the complete CERN complex of accelerators.

Protons coming from a source are first accelerated in the linear accelerator linac2 which then injects the protons in the booster ring. From the booster ring the protons move to the PS (Proton Synchrotron) before being injected in the SPS (Super Proton Synchrotron) and are then finally injected in the LHC. Ions are injected in LEIR (Low Energy Ion Ring) from linac 3, then move to the PS and the SPS before being injected in the LHC.

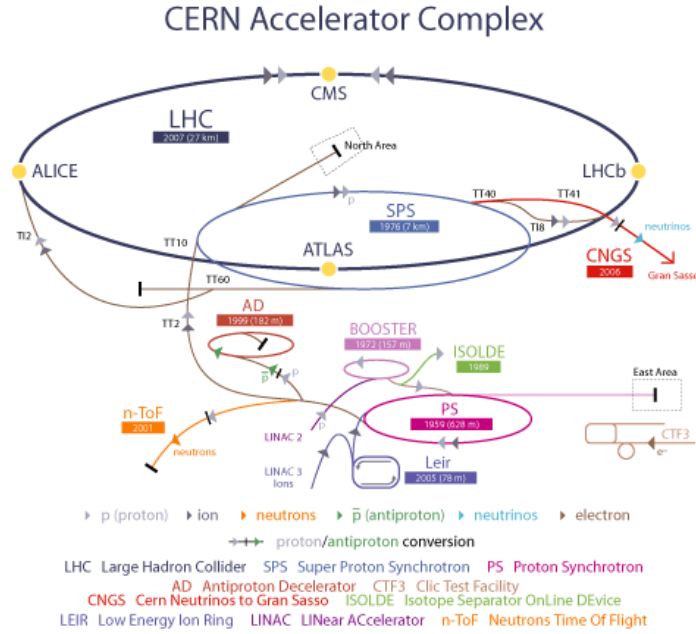


FIGURE 1.3.1. CERN Accelerator Complex

CHAPTER 2

Transverse Beam Dynamics

2.1. The Coordinate System (Frenet-Serret)

In this chapter a short treatment of the transverse beam dynamics, a description of the basic equations of motion in the plane transverse to the particle's trajectory, will be given. The coordinate system used in this text is shown in figure 2.1.1, where s is the curvilinear parameter. A coordinate system commonly used in Accelerator Physics which is basically a Frenet-Serret system. I will quickly review the basic equations for such a coordinate system.

Assume the position of the particle is given by the vector $\vec{r}_0(s)$, the coordinate system unit vectors are then given by

$$(2.1.1) \quad \hat{s}(s) = \frac{d\vec{r}_0(s)}{ds}$$

$$(2.1.2) \quad \hat{x}(s) = -\rho(s) \frac{d\hat{s}(s)}{ds}$$

$$(2.1.3) \quad \hat{y}(s) = \hat{x}(s) \times \hat{s}(s)$$

where $\rho(s)$ is the radius of curvature.

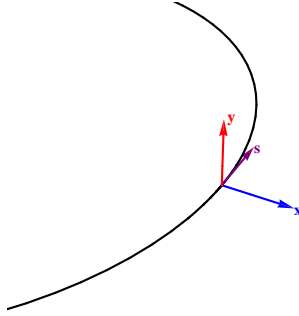


FIGURE 2.1.1. Coordinate system

Equations (2.1.4) and (2.1.5) are known as the Frenet-Serret Equations

$$(2.1.4) \quad \hat{x}'(s) = \frac{1}{\rho(s)} \hat{s}(s) + \tau(s) \hat{y}(s)$$

$$(2.1.5) \quad \hat{y}'(s) = -\tau(s) \hat{x}(s)$$

where $\tau(s)$ is the torsion, the hats refer to unit vectors in the respective directions and the primes refer to the derivatives with respect the curvilinear parameter s . The motion of a particle can be described in this Frenet-Serret coordinate system by

$$(2.1.6) \quad \vec{r}(s) = \vec{r}_0(s) + x\hat{x}(s) + y\hat{y}(s)$$

with $\vec{r}_0(s)$ the reference orbit or the ideal orbit. In this chapter the dynamics of the particles that deviate from this ideal orbit in the transverse plane will be treated.

2.2. Hamiltonian Mechanics

In this section an expression for the Hamiltonian is derived from which the equations of motion in the Frenet-Serret coordinate system then follow. This derivation is taken from [16].

The main advantage of a circular accelerator compared to a linear accelerator is that you can re-use the same accelerating component (RF cavities, see Section 3.3) for accelerating the particles to a higher energy. But, a circular machine means circular trajectories for the particles, so if the particles need to stay on a circular orbit a force to bend their trajectories will be needed. Since we are dealing with charged particles (Protons and Lead Ions) we can use the Lorentz force (Eq. (2.2.1)) to bend the particle trajectories.

$$(2.2.1) \quad \vec{F} = q(\vec{E} + \vec{v} \times \vec{B})$$

This Lorentz Force can be derived using the Lagrange's equations

$$(2.2.2) \quad \frac{d}{dt} \left(\frac{\partial L}{\partial \dot{q}} \right) - \frac{\partial L}{\partial q} = 0$$

from the Lagrangian L

$$(2.2.3) \quad L = -mc^2 \sqrt{1 - \frac{\vec{v}^2}{c^2}} - e\Phi + e\vec{v} \cdot \vec{A}$$

with ϕ the scalar potential and \vec{A} the vector potential of the Electro-Magnetic field (ie. $\vec{E} = -\nabla\phi - \frac{\partial \vec{A}}{\partial t}$ and $\vec{B} = \nabla \times \vec{A}$). Introducing the Canonical Momentum $\vec{P} = \frac{\partial L}{\partial \vec{v}} = \vec{p} + e\vec{A}$, where \vec{p} is the mechanical momentum, allows us to change to Hamiltonian Mechanics, with the Hamiltonian

$$(2.2.4) \quad H = \vec{P} \cdot \vec{v} - L = c \left[m^2 c^2 + (\vec{P} - e\vec{A})^2 \right]^{1/2} + e\phi,$$

resulting in the equations of motion (the overhead dot refers to the derivative with respect to time)

$$(2.2.5) \quad \dot{q}_i = \frac{\partial H}{\partial P_i}, \quad \dot{P}_i = -\frac{\partial H}{\partial q_i}.$$

Because the goal here is to express the equations of motion in a Frenet-Serret system an expression for the Hamiltonian in this coordinate system (s, x, y) is needed. The generating function F_3 ([16], Appendix A), shown in equation (2.2.6),

$$(2.2.6) \quad F_3(\vec{P}, s, x, y) = -\vec{P} \cdot [\vec{r}_0(s) + x\hat{x}(s)],$$

with \vec{P} the momentum in the Cartesian System leads to the following set of transformations

$$(2.2.7) \quad p_s = -\frac{\partial F_3}{\partial s} = \left(1 + \frac{x}{\rho}\right) \vec{P} \cdot \hat{s}$$

$$(2.2.8) \quad p_x = -\frac{\partial F_3}{\partial x} = \vec{P} \cdot \hat{x}$$

$$(2.2.9) \quad p_y = -\frac{\partial F_3}{\partial y} = \vec{P} \cdot \hat{y}.$$

Applying these transformations in expression (2.2.4) returns an expression for the Hamiltonian in the Frenet-Serret system.

$$(2.2.10) \quad H = e\phi + c \left(m^2 c^2 + \frac{(p_s - eA_s)^2}{\left(1 + \frac{x}{\rho}\right)^2} + (p_x - eA_x)^2 + (p_y - eA_y)^2 \right)^{\frac{1}{2}},$$

where

$$\begin{aligned}
 A_s &= \left(1 + \frac{x}{\rho}\right) \vec{A} \cdot \hat{s} \\
 A_x &= \vec{A} \cdot \hat{x} \\
 A_y &= \vec{A} \cdot \hat{y}
 \end{aligned}
 \tag{2.2.11}$$

and the resulting equations of motion become:

$$\begin{aligned}
 \dot{s} &= \frac{\partial H}{\partial p_s}, \quad \dot{p}_s = -\frac{\partial H}{\partial s}, \\
 \dot{x} &= \frac{\partial H}{\partial p_x}, \quad \dot{p}_x = -\frac{\partial H}{\partial x}, \\
 \dot{y} &= \frac{\partial H}{\partial p_y}, \quad \dot{p}_y = -\frac{\partial H}{\partial y}.
 \end{aligned}
 \tag{2.2.12}$$

In the equations (2.2.12) the independent variable is still the time t . We would like to use s as an independent variable. Using $\frac{dq}{dt} = \frac{dq}{ds} \frac{ds}{dt}$ the equations (2.2.12) can be rewritten as (the prime relates to the derivative with respect to s)

$$\begin{aligned}
 t' &= \frac{\partial p_s}{\partial H}, \quad H' = -\frac{\partial p_s}{\partial t}, \\
 x' &= -\frac{\partial p_s}{\partial p_x}, \quad p'_x = \frac{\partial p_s}{\partial x}, \\
 y' &= -\frac{\partial p_s}{\partial p_y}, \quad p'_y = \frac{\partial p_s}{\partial y}.
 \end{aligned}
 \tag{2.2.13}$$

In expressions (2.2.13) one can easily recognize the structure of the equations of motion from Hamiltonian Mechanics but with $-p_s$ as the new Hamiltonian \tilde{H} and with new phase-space coordinates $(x, p_x, y, p_y, t, -H)$. If we now assume time independent potentials for the electromagnetic fields, then the Hamiltonian is also time independent, but still a function of s . Since in this text we consider only circular accelerators, the Hamiltonian will be periodic!

$$\tilde{H} = -\left(1 + \frac{x}{\rho}\right) \left[\frac{(H - e\phi)^2}{c^2} - m^2 c^2 - (p_x - eA_x)^2 - (p_y - eA_y)^2 \right]^{\frac{1}{2}} - eA_s
 \tag{2.2.14}$$

With this new Hamiltonian the particle's energy is $E = H - e\phi$ and its momentum is $p = \sqrt{\frac{E^2}{c^2} - m^2 c^2}$, so that the new Hamiltonian can be written as

$$\tilde{H} = -\left(1 + \frac{x}{\rho}\right) \left[p^2 - (p_x - eA_x)^2 - (p_y - eA_y)^2 \right]^{\frac{1}{2}} - eA_s.
 \tag{2.2.15}$$

The transverse momenta p_x, p_y of the particles will be small in comparison to the total momenta. Keeping this in mind the Hamiltonian \tilde{H} can be expanded to first order in p (and keeping only linear terms : $\sqrt{1+x} \approx 1 + \frac{1}{2}x$) as shown in equation (2.2.16).

$$\tilde{H} \approx -p \left(1 + \frac{x}{\rho}\right) + \frac{1 + \frac{x}{\rho}}{2p} \left[(p_x - eA_x)^2 + (p_y - eA_y)^2 \right] - eA_s
 \tag{2.2.16}$$

Expressions (2.2.13) and expression (2.2.16) are respectively the equations of motion and the Hamiltonian in the Frenet-Serret coordinate system. We will use them in the next sections to describe the particles motion in the beam in the transverse directions.

2.3. Magnetic Fields in the Frenet-Serret Coordinate System

In this section we also follow [16] to derive the expressions of the \vec{E} and \vec{B} fields in the Frenet-Serret coordinate system. For the Frenet-Serret coordinate system the scale factors are:

$$(2.3.1) \quad h_s = 1 + \frac{x}{\rho}, \quad h_x = 1, \quad h_y = 1$$

With these scale factors and equations (2.2.11) the expression for magnetic field $\vec{B} = \nabla \times \vec{A}$ becomes

$$(2.3.2) \quad \nabla \times \vec{A} = \frac{1}{h_s} \left[\frac{\partial A_3}{\partial s} - \frac{\partial (h_s A_2)}{\partial y} \right] \hat{x} + \left[\frac{\partial A_1}{\partial y} - \frac{\partial A_3}{\partial x} \right] \hat{s} + \frac{1}{h_s} \left[\frac{\partial (h_s A_2)}{\partial x} - \frac{\partial A_1}{\partial s} \right] \hat{y},$$

where we used $A_1 = \vec{A} \cdot \hat{x}$, $A_2 = \vec{A} \cdot \hat{s}$, $A_3 = \vec{A} \cdot \hat{y}$. For accelerators the electric field is usually zero ($\phi = 0$) and the magnetic fields are transverse fields ($A_x = A_1 = 0 = A_y = A_3$). Under these conditions the magnetic field can be written as

$$(2.3.3) \quad \vec{B} = B_x(x, y) \hat{x} + B_y(x, y) \hat{y},$$

with

$$(2.3.4) \quad B_x = -\frac{1}{h_s} \frac{\partial (h_s A_2)}{\partial y} = -\frac{1}{h_s} \frac{\partial A_s}{\partial y}$$

$$(2.3.5) \quad B_y = \frac{1}{h_s} \frac{\partial (h_s A_2)}{\partial x} = \frac{1}{h_s} \frac{\partial A_s}{\partial x}$$

By using the Maxwell equation $\nabla \times \vec{B} = 0$ we arrive at expression (2.3.6) for A_s .

$$(2.3.6) \quad \frac{\partial}{\partial y} \frac{1}{h_s} \frac{\partial A_s}{\partial y} + \frac{\partial}{\partial x} \frac{1}{h_s} \frac{\partial A_s}{\partial x} = 0$$

As an example now assume straight geometry ($h_s = 1$) so that A_s can be written as a power series

$$(2.3.7) \quad A_s = B_0 \operatorname{Re} \left[\sum_{n=0}^{\infty} \frac{b_n + j a_n}{n+1} (x + jy)^{n+1} \right]$$

with j the imaginary number. The total magnetic field is given by (Bethe representation, minus sign for positive charges and plus sign for negative charges)

$$(2.3.8) \quad \begin{aligned} \frac{1}{B\rho} (B_y + j B_x) &= \mp \frac{1}{\rho} \sum_{n=0}^{\infty} (b_n + j a_n) (x + jy)^{n+1} \\ b_n &= \frac{1}{B_0 n!} \frac{\partial^n B_y}{\partial x^n} \Big|_{x=z=0} \\ a_n &= \frac{1}{B_0 n!} \frac{\partial^n B_x}{\partial x^n} \Big|_{x=z=0} \end{aligned}$$

The normalization constant B_0 is usually chosen so that $b_0 = 1$, thus $B_0 b_0 = -\frac{B\rho}{\rho}$. The term $B\rho$ is referred to as the magnetic rigidity and is equal to $\frac{p}{e}$. The coefficients a_n, b_n are referred to as the $2(n+1)^{th}$ multipole coefficients with b_0 the dipole coefficient, a_0 the dipole roll coefficient, b_1 the quadrupole coefficient, a_1 the skew quadrupole coefficient, and so on.

More general solutions (for non straight geometries) for equation (2.3.6) can also be found by use of power series but fall outside of the scope of this text. In figure 2.3.1 we show a schematic diagram of a LHC Dipole Magnet and in figure 2.3.2 a cross section of a LHC QM.

LHC DIPOLE : STANDARD CROSS-SECTION

CERN.AC/DI/MM - HE107 - 30.04.1999

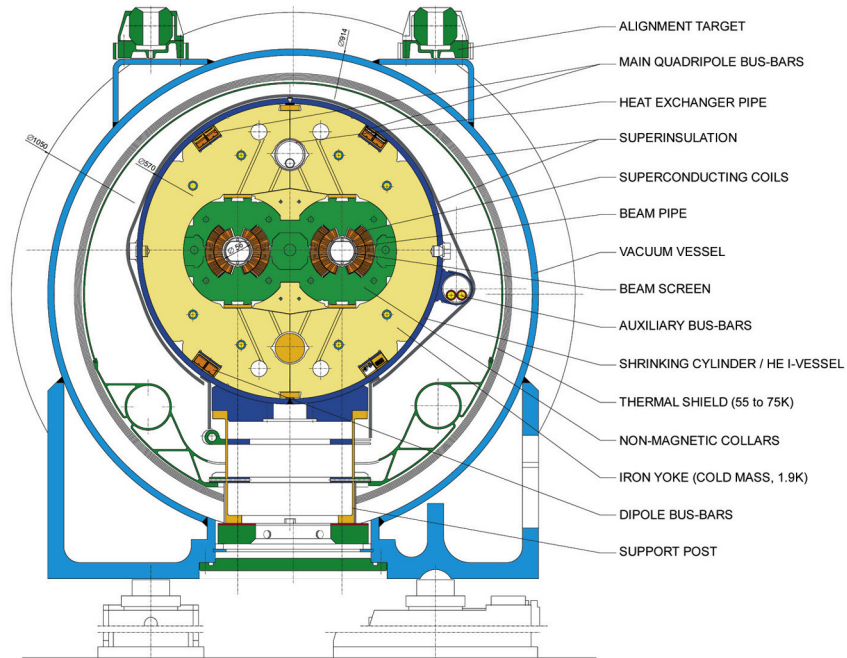
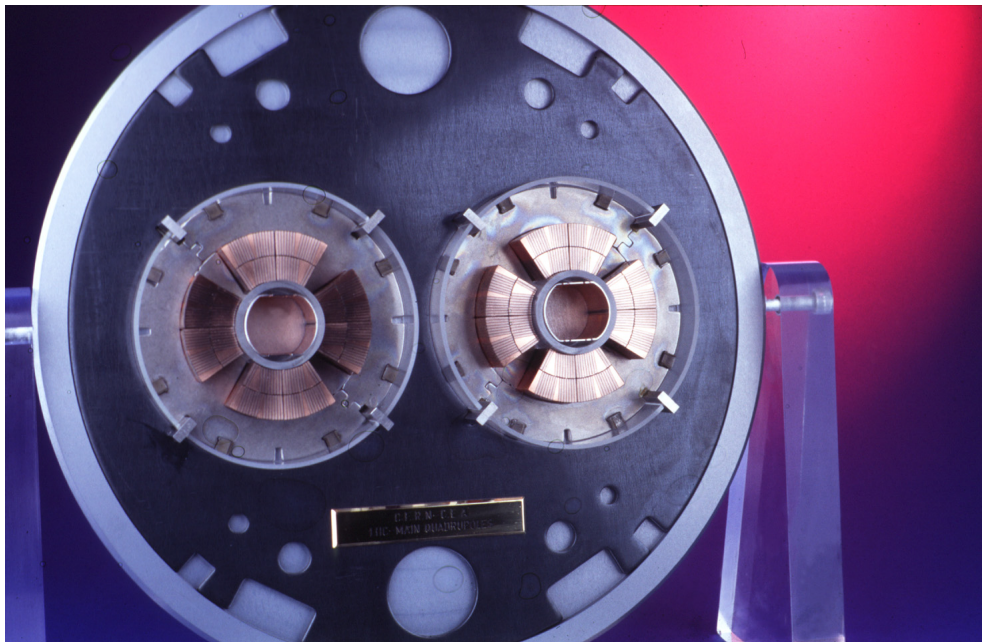


FIGURE 2.3.1. LHC dipole magnet (source : [2])

FIGURE 2.3.2. LHC Quadrupole Magnet (source : [HTTP://wwwae.ciemat.es/](http://wwwae.ciemat.es/))

2.4. Betatron Motion

Ignoring the effects of longitudinal motion (cfr. Chapter 3) for the moment the equations of motion (2.2.13) describe the motion of a particle in the transverse plane (xy-plane). This motion is referred to as Betatron Motion and has the linearized equations of motion

$$(2.4.1) \quad \begin{aligned} x'' - \frac{\rho + x}{\rho^2} &= \pm \frac{B_y}{B\rho} \frac{p_0}{p} \left(1 + \frac{x}{\rho}\right)^2, \\ y'' &= \mp \frac{B_x}{B\rho} \frac{p_0}{p} \left(1 + \frac{x}{\rho}\right)^2, \end{aligned}$$

where p_0 is the total momentum of a reference particle (= particle on the ideal orbit or reference orbit in the machine), p is the momentum of the particle of which we want to study the motion and $B\rho = \frac{p_0}{e} \geq 0$ with the used sign convention. In the equations (2.4.1) higher order terms have been neglected (only considering dipole and quadrupole fields, see section 2.5).

These equations belong to a class of equations known as the Hill's equations because the functions $K_x(s)$ and $K_y(s)$ are periodic (we only consider circular accelerators here so that $K_x(s+L) = K_x(s)$ and $K_y(s+L) = K_y(s)$).

Hill's equations¹ are used to describe systems that contain periodic focusing properties and have the general form

$$(2.4.2) \quad u''(s) + K(s)u = 0$$

where $K(s)$ describes the periodic focusing properties of the system. The expressions in (2.4.1) can be rewritten in this general form as is shown in (2.4.3) and (2.4.4) for both transverse directions.

$$(2.4.3) \quad x'' + K_x(s)x = 0, \quad K_x = \frac{1}{\rho^2} \mp \frac{B_1(s)}{B\rho},$$

$$(2.4.4) \quad y'' + K_y(s)y = 0, \quad K_y = \pm \frac{B_1(s)}{B\rho},$$

with $B_y = \mp B_0 + \frac{\partial B_y}{\partial x}x = \mp B_0 + B_1x$ and $B_x = \frac{\partial B_y}{\partial x}y = B_1y$. In the next section we will take a closer look at these equations and their solutions.

2.5. Betatron Motion: Linear Approximation

2.5.1. Matrix Formalism². With the periodic conditions $K_x(s+L) = K_x(s)$, $K_y(s+L) = K_y(s)$ and assuming the K_i to be constant ($K = K_x, K = K_y$) the solutions for (2.4.3) can be written as

$$(2.5.1) \quad x(s) = \begin{cases} a \cos(\sqrt{K}s + b) & K > 0 \\ as + b & K = 0 \\ a \cosh(\sqrt{-K}s + b) & K < 0 \end{cases}.$$

Similar expressions for $y(s)$ can be written down. The integration constants can be determined using $x'(s)$ and the initial conditions $x_0 = x(s_0)$, $x'_0 = x'(s_0)$. Let now

$$(2.5.2) \quad \mathbf{x}(s) = \begin{pmatrix} x(s) \\ x'(s) \end{pmatrix}$$

be the Betatron State Vector for the x-plane (consisting of the phase-space coordinates of the particle under consideration, a similar state vector can be written down for the y-plane). With this notation a matrix

¹The Hill's equations come from the study of the motion of the moon around the earth. These equations and their solutions are taken over from the study equations of motion in stellar physics.

²The idea of using a matrix formalism comes from Quantum Mechanics. When physicists were doing the first calculations on accelerators in the Manhattan Project they realized that the potentials looked a lot like a periodic potential in Quantum Mechanics, hence the Matrix Formalism.

formalism can be introduced by expressing the solutions of the Hill's equations as

$$(2.5.3) \quad \mathbf{x}(s) = M(s) \mathbf{x}(s_0)$$

where $M(s)$ is the Betatron Transfer Matrix.

Since the Wronskian W of two independent solutions does not depend on s it follows that $\frac{dW}{ds} = 0$. From this we have that $\det(M) = 1$ since $W(s) = \det(M) W(s_0)$.

Considering still a constant K in the Hill's equations we have three possible matrices $M(s)$:

$$(2.5.4) \quad M(s) = \begin{cases} \begin{pmatrix} \cos(\sqrt{K}l) & \frac{1}{\sqrt{K}} \sin(\sqrt{K}l) \\ -\sqrt{K} \sin(\sqrt{K}l) & \cos(\sqrt{K}l) \end{pmatrix} & K > 0, \text{ Focussing Quad., Dipole} \\ \begin{pmatrix} 1 & l \\ 0 & 1 \end{pmatrix} & K = 0, \text{ Drift Space} \\ \begin{pmatrix} \cosh(\sqrt{|K|}l) & \frac{1}{\sqrt{|K|}} \sinh(\sqrt{|K|}l) \\ \sqrt{|K|} \sinh(\sqrt{|K|}l) & \cosh(\sqrt{|K|}l) \end{pmatrix} & K < 0, \text{ Defocussing Quadrupole} \end{cases}$$

where $l = s - s_0$ is the length of the magnet or drift space.

As an example we will now apply this for a dipole of length l . For a dipole $K_x = \frac{1}{\rho^2}$, and with $\theta = \frac{l}{\rho}$ the orbiting angle the matrix M becomes

$$(2.5.5) \quad M(s, s_0) = \begin{pmatrix} \cos \theta & \rho \sin \theta \\ -\frac{1}{\rho} \sin \theta & \cos \theta \end{pmatrix}.$$

Once one has determined the transfer matrices for all the elements (dipoles, quadrupoles,...) in the accelerator the transfer matrices over any interval of s along the accelerator can be determined as a product of the transfer matrices of the elements in that interval

$$(2.5.6) \quad M(s_2, s_0) = M(s_2, s_1) M(s_1, s_0).$$

Notice that in the matrix M the second row is the derivative with respect to s of the first row. The notation shown in (2.5.7) can be often found in books or articles treating this subject.

$$(2.5.7) \quad M(s, s_0) = \begin{pmatrix} C(s, s_0) & S(s, s_0) \\ C'(s, s_0) & S'(s, s_0) \end{pmatrix}.$$

2.5.2. Stable orbital Betatron Motion. Remember that the considered accelerator is circular, hence M is periodic $M(s + L) = M(s)$. Using the notation $\mathbf{M} = M(L + s_0, s_0)$ for the transfer matrix of a full revolution (or over a periodic cell, if the accelerator is built of consecutive copies of such periodic cells) the Transfer Matrix for n revolutions becomes \mathbf{M}^n (\mathbf{M}^{Pn} , for the accelerator consisting of P periodic cells). The particles orbit will be stable if all the elements of the Transfer Matrix stay bounded as the number of revolutions increases. We have already explained that the determinant of the matrix M is unity, which also means that the eigenvalues of M will be each others reciprocal ($\lambda_1 = \frac{1}{\lambda_2}$). The characteristic eigenvalue equation for M is then

$$\lambda^2 - \text{Tr}(M) \lambda + 1 = 0.$$

Considering the case where $\text{Tr}(M) = 2 \cos \Phi$ (cfr. Eq. (2.5.5)), the solution for Φ is real if $|\text{Tr}(M)| \leq 2$. This means there exists a stability condition that needs to be satisfied to have a stable beam. Φ is called the Betatron Phase-Advance.

2.5.3. The Optical Functions (Courant-Snyder parameters /Twiss parameters). Returning to the Hill's equations (2.4.3), we now no longer consider K to be constant but to be a function of s (the periodicity condition is still valid $K_{x,y}(s+L) = K_{x,y}(s)$). Under these conditions a solution of the form

$$(2.5.8) \quad \begin{aligned} x(s) &= \sqrt{\epsilon\beta(s)} \cos(\psi(s) + \phi) \\ x'(s) &= -\frac{\sqrt{\epsilon}}{\sqrt{\beta(s)}} (\alpha(s) \cos(\psi(s) + \phi) + \sin(\psi(s) + \phi)) \quad \text{with } \alpha(s) = \frac{-\beta'(s)}{2} \end{aligned}$$

can be proposed [24] (similar equations hold in the y-plane), with ϵ and ϕ integration constants determined by the initial conditions. $\beta(s)$ is called the Beta-Function and describes the periodic focusing effects in the accelerator, this function is of course also periodic $\beta(L+s) = \beta(s)$. A plot of the Beta-Functions (the horizontal and the vertical) can be seen in figures 6.1.1 and 6.2.1. The Beta-function is important because it is related to the beam size, the maximum deviation from the reference orbit is given by the deviation $x(s) = \sqrt{\epsilon\beta(s)}$.

Considering the beam to be Gaussian in the plane under consideration (x or y plane) we usually assume $\sigma = \sqrt{\epsilon\beta(s)}$ with σ the standard deviation of the Gaussian distribution.

Inserting the proposed solution in equation (2.4.3) gives an expression for $\psi(s)$

$$(2.5.9) \quad \psi(s) = \int_0^s \frac{ds}{\beta(s)},$$

which is called the Phase-Advance. (Φ in 2.5.2).

The Tunes of the accelerator are then defined as

$$(2.5.10) \quad Q_{x,y} = \frac{1}{2\pi} \oint \frac{ds}{\beta_{x,y}(s)},$$

ie. the number of oscillations around the reference orbit in the x or y plane per full machine turn. The Tunes are important from a beam stability point of view, if a perturbation along the ring is in phase with the Betatron Oscillations of the particles this will cause a resonance in the machine and the particles trajectories will become unstable and be lost.

The parameter ϵ is called the emittance (for a more in depth discussion of the emittance concept see section 2.7) and can be calculated from the Hill's equations [5] from the expression

$$(2.5.11) \quad \epsilon_x = \gamma_x(s) x^2(s) + 2\alpha_x(s) x(s) x'(s) + \beta_x(s) x'^2(s) \quad \text{with} \quad \begin{cases} \alpha_x(s) = -\frac{1}{2}\beta'_x(s) \\ \gamma_x(s) = \frac{1+\alpha_x^2(s)}{\beta_x(s)} \end{cases}$$

where we stressed that the used parameters are in the x-plane. A similar expression can be written down in the vertical plane (y-plane). The parameters $\alpha(s), \beta(s), \gamma(s)$ are often referred to as the Courant-Snyder parameters, Twiss parameters or the Optical Functions. In this text we will refer to them as the Optical Functions. Notice that the emittance is a constant and that the equation describing it has the form of an ellipse in phase-space.

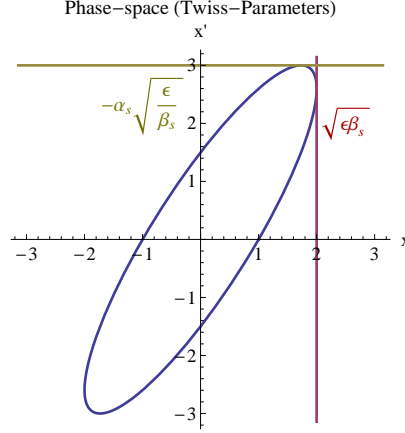


FIGURE 2.5.1. Example of a phase-space ellipse

The fact that the emittance is a constant means that a large beam size will give rise to a small beam divergence and vice versa. One can also define the admittance which is the area of the largest phase-space ellipse the accelerator can accept. If we define the half-aperture that is available in the accelerator by $a(s)$ then the admittance [9] is given by $\pi \frac{a(s)^2}{\beta} \Big|_{min}$.

Working with the Optical Functions is less handy than working with the matrix formalism from the previous section, it would be handy to also have a matrix formalism for the Optical Functions. To develop this matrix formalism we start by putting in some initial conditions into the proposed solutions of the Hill's equations (2.5.8). Under the assumptions $\psi(0) = 0$ and $s(0) = s_0$ these equations become

$$(2.5.12) \quad \cos \phi = \frac{x_0}{\sqrt{\epsilon \beta_0}},$$

$$(2.5.13) \quad \sin \phi = -\frac{1}{\epsilon} \left(x'_0 \sqrt{\beta_0} + \frac{\alpha_0 x_0}{\sqrt{\beta_0}} \right).$$

Inserting these results in (2.5.8) they can be rewritten as

$$(2.5.14) \quad \mathbf{x}(s) = M(s) \mathbf{x}(s_0),$$

with

$$(2.5.15) \quad M(s) = \begin{pmatrix} \sqrt{\frac{\beta_s}{\beta_0}} \cos(\psi_s) + \alpha_0 \sin(\psi_s) & \sqrt{\beta_s \beta_0} \sin(\psi_s) \\ \frac{(\alpha_0 - \alpha_s) \cos(\psi_s) - (1 + \alpha_0 \alpha_s) \sin(\psi_s)}{\sqrt{\beta_s \beta_0}} & \sqrt{\frac{\beta_s}{\beta_0}} \cos(\psi_s) - \alpha_0 \sin(\psi_s) \end{pmatrix}.$$

With the above matrix there is no longer a need for matrix multiplication if we want to know the phase-space parameters along the ring once they are known at one location in the machine (assuming the Optical Functions are known everywhere along the machine). Note that this matrix can also be written as

$$(2.5.16) \quad \begin{aligned} M(s, s_0) &= \begin{pmatrix} \sqrt{\beta_s} & 0 \\ -\frac{\alpha_s}{\sqrt{\beta_s}} & \frac{1}{\sqrt{\beta_s}} \end{pmatrix} \begin{pmatrix} \cos(\psi) & \sin(\psi) \\ -\sin(\psi) & \cos(\psi) \end{pmatrix} \begin{pmatrix} \frac{1}{\sqrt{\beta_0}} & 0 \\ \frac{\alpha_0}{\sqrt{\beta_0}} & \sqrt{\beta_0} \end{pmatrix} \\ &= B(s) \begin{pmatrix} \cos(\psi) & \sin(\psi) \\ -\sin(\psi) & \cos(\psi) \end{pmatrix} B^{-1}(s_0), \end{aligned}$$

with $\psi = \psi_s - \psi_0$ and where the matrix $B(s)$ is called the Betatron Amplitude Matrix. The effect of multiplying the Betatron State Vector with the matrix $M(s, s_0)$ can be interpreted as a coordinate rotation of the phase-space coordinates after normalization with the Betatron Amplitude Matrix, hence a rotation of the phase-space ellipse (see figures 2.5.2 and 2.5.3).

Using the same approach as before we can define a transfer matrix \mathbf{M} for a complete turn. Defining ψ_{turn} as

$$(2.5.17) \quad \psi_{turn} = \int_s^{s+L} \frac{ds}{\beta_s},$$

the expression for this matrix becomes

$$(2.5.18) \quad \mathbf{M} = \begin{pmatrix} \cos(\psi_{turn}) + \alpha_s \sin(\psi_{turn}) & \beta_s \sin(\psi_{turn}) \\ -\gamma_s \sin(\psi_{turn}) & \cos(\psi_{turn}) - \alpha_s \sin(\psi_{turn}) \end{pmatrix}.$$

Following the same reasoning as in section 2.5.2 again a stability condition emerges: $|Tr(\mathbf{M})| \leq 2$.

Fixed points of order n are points in phase-space that return on themselves after n turns, ie. $\mathbf{F}_2 = \mathbf{M}^n \mathbf{F}_1 = \mathbf{F}_1$. The orbit that corresponds to a fixed point of order one is called the closed orbit. The stability condition requires the existence of such fixed points.

The problem of describing the particles motions in the transverse planes is now reduced to finding the Optical Functions along the entire ring. The fact that the emittance is a constant of motion will turn out to be very helpful [5]. Consider the emittance at point s and at point s_0 . Both emittances at these locations will have to be equal since the emittance is a constant,

$$(2.5.19) \quad \begin{aligned} \epsilon &= \beta_s x'^2 + 2\alpha_s x x' + \gamma_s x^2 \\ &= \beta_0 x_0'^2 + 2\alpha_0 x_0 x_0' + \gamma_0 x_0^2, \end{aligned}$$

where

$$(2.5.20) \quad \begin{pmatrix} x(s) \\ x'(s) \end{pmatrix} = M \begin{pmatrix} x(s_0) \\ x'(s_0) \end{pmatrix}.$$

Inserting equation (2.5.20) in the expressions (2.5.19) and recollecting the terms results in

$$(2.5.21) \quad \begin{pmatrix} \beta \\ \alpha \\ \gamma \end{pmatrix}_2 = \begin{pmatrix} M_{11}^2 & -2M_{11}M_{12} & M_{12}^2 \\ -M_{11}M_{21} & M_{11}M_{22} + M_{12}M_{21} & -M_{12}M_{22} \\ M_{21}^2 & -2M_{21}M_{22} & M_{22}^2 \end{pmatrix} \begin{pmatrix} \beta \\ \alpha \\ \gamma \end{pmatrix}_1$$

The above matrix is completely determined by the focusing properties of the optical (dipoles, quadrupoles,...) components of the accelerator lattice. Note that in the above calculations we only considered the x-plane, similar calculations are of course valid in the y-plane. The sets of equations for both planes can be combined in one large 6×6 matrix. The matrix shown in (2.5.23) has zeros for the off-diagonal elements, this means that here we have assumed that there is no coupling between the horizontal and vertical plane. In reality however there will be at least some coupling between the two planes (for example a quadrupole rotated around its center axis can be a cause of coupling). This coupling can be described by replacing the zeros in (2.5.23) by the correct non-zero terms. Treatment of coupling falls outside of the scope of this text, so we will not go deeper into this subject here.

$$(2.5.22) \quad \begin{pmatrix} \beta \\ \alpha \\ \gamma \end{pmatrix}_x = T_x, \quad \begin{pmatrix} \beta \\ \alpha \\ \gamma \end{pmatrix}_y = T_y$$

$$(2.5.23) \quad \begin{pmatrix} T_x \\ T_y \end{pmatrix}_2 = \begin{pmatrix} M_x & 0 \\ 0 & M_y \end{pmatrix} \begin{pmatrix} T_x \\ T_y \end{pmatrix}_1$$

2.5.4. Linear Approximation. All of the calculations in this section up until now have been linear approximations. We hope to make this clear to the reader by use of an example of a non-linear case. Let me for instance consider the effects of a sextupole (with strength k_2) on a particles phase-space coordinates.

$$(2.5.24) \quad \begin{pmatrix} x \\ x' \\ y \\ y' \end{pmatrix}_{s_2} = \begin{pmatrix} x \\ x' \\ y \\ y' \end{pmatrix}_{s_1} + \begin{pmatrix} 0 \\ k_2(x_{s_1}y_{s_1}) \\ 0 \\ \frac{1}{2}k_2(x_{s_1}^2 - y_{s_1}^2) \end{pmatrix}_{s_2}$$

As the reader might notice it is impossible for equation (2.5.24) to be rewritten in the form of equation (2.5.14) by use of a matrix. Non-linear elements such as sextupoles can be handled in two ways. In the classical approach one would rewrite the Hill's equations taking these non-linear elements into account (they show up in the $K(s)$ factors) and try to solve the equations by pages of calculations using series expansions and approximating them to some desired order. In the modern approach one uses advanced mathematical tools such as Taylor Maps, Lie Transforms, Symplectic Integration and Differential Algebra. Unfortunately a treatment of these tools fall outside of the scope of this text due to time limitations. For an introduction to these tools and concepts I refer the reader to the CERN student lectures of the BE department created and presented by Werner Herr [12] and the references therein.

2.5.5. Examples of phase-space ellipse rotation.

2.5.5.1. *Drift space of length l .* A drift space is basically a straight section of beam pipe. The transformation for the Optical Functions through a drift space of length l can be written as

$$(2.5.25) \quad \begin{pmatrix} \beta(l) \\ \alpha(l) \\ \gamma(l) \end{pmatrix} = \begin{pmatrix} 1 & -2l & l^2 \\ 0 & 1 & -l \\ 0 & 0 & 1 \end{pmatrix} \begin{pmatrix} \beta(0) \\ \alpha(0) \\ \gamma(0) \end{pmatrix}.$$

This gives the following picture (the horizontal axis represents s for the positions of the ellipses in respect to each other and represents x for the considered ellipse, with the center of the ellipse representing $x = 0$) for the phase-space evolution.

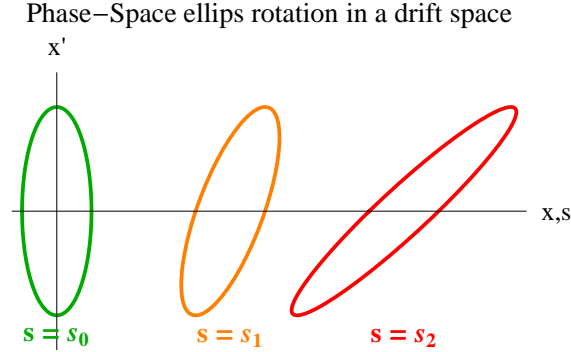


FIGURE 2.5.2. Rotation in phase-space for a drift space

Particles in the upper half of the ellipse will move to the right in phase-space while particles in the lower half will move to the left. Notice the growing beam size.

2.5.5.2. *Focusing Quadrupole of length l .* Again the transformation for the Optical Functions can be written down, using equation (2.5.4)) where $C = \cos$, $S = \sin$ and $\sqrt{K}l = m$ we have

$$(2.5.26) \quad \begin{pmatrix} \beta(l) \\ \alpha(l) \\ \gamma(l) \end{pmatrix} = \begin{pmatrix} C^2(m) & -\frac{2}{\sqrt{K}}C(m)S(m) & \frac{1}{K}S^2(m) \\ \sqrt{K}C(m)S(m) & C^2(m) - S^2(m) & -\frac{1}{\sqrt{K}}C(m)S(m) \\ KS^2(m) & 2\sqrt{K}C(m)S(m) & C^2(m) \end{pmatrix} \begin{pmatrix} \beta(0) \\ \alpha(0) \\ \gamma(0) \end{pmatrix}.$$

Figure 2.5.3 shows a plot of the evolution of the phase-space ellipse when passing a focusing quadrupole (again the horizontal axis represents s for the positions of the ellipses in respect to each other and represents x for the considered ellipse, with the center of the ellipse representing $x = 0$).

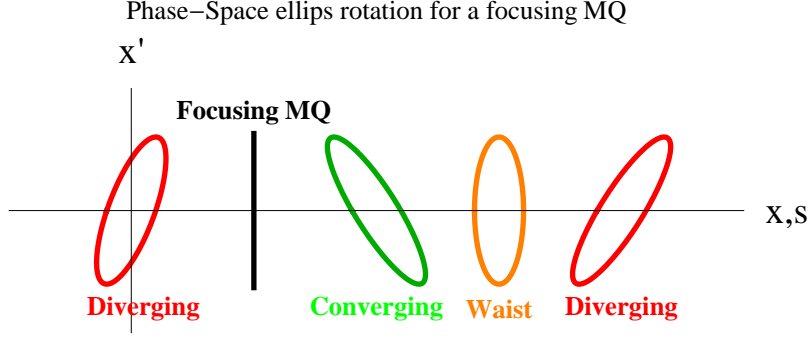


FIGURE 2.5.3. Rotation in phase-space for a focusing quadrupole

2.6. Action-Angle Variables

Let me start by restating the general form of the Hill's equation

$$(2.6.1) \quad u''(s) + K(s)u(s) = 0$$

and the proposed solution $u(s) = \sqrt{\epsilon\beta(s)} \cos(\psi(s) + \phi)$ where ϵ and ϕ are constants. After plugging in the proposed solution an equation of the form $a \cos x + b \sin x = 0$ is found. Since the cosine and sine can not be zero at the same time their coefficients have to be equal to zero. Putting these coefficients equal to zero results in two new equations (2.6.2) and (2.6.3)

$$(2.6.2) \quad \frac{1}{2} \left(\beta\beta'' - \frac{1}{2}\beta'^2 \right) - \beta^2\psi'^2 + \beta^2 K = 0,$$

$$(2.6.3) \quad \beta'\psi' + \beta\psi'' = 0.$$

After choosing the correct normalization for equation (2.6.3) we have

$$(2.6.4) \quad \beta\psi' = 1.$$

Putting this result back in equation (2.6.2) gives us

$$(2.6.5) \quad \frac{1}{2}\beta'' + \beta K - \frac{1}{\beta} \left(1 + \left(\frac{\beta'}{2} \right)^2 \right) = 0.$$

The Hill's equation (2.4.4) can be derived from the pseudo-Hamiltonian [16]

$$(2.6.6) \quad H = \frac{1}{2}u'^2 + \frac{1}{2}K(s)u^2,$$

with (u, u') as conjugate phase-space coordinates. Using equation (2.6.3) we can write

$$(2.6.7) \quad u' = -\frac{u}{\beta} \left(\tan \psi - \frac{\beta'}{2} \right),$$

under the assumption that β obeys equation (2.6.2). This hints in the direction of a generating function of the form

$$(2.6.8) \quad F_1(u, \psi) = \int_0^u u' du = -\frac{u^2}{2\beta} \left(\tan \psi - \frac{\beta'}{2} \right),$$

with $u' = \frac{\partial F_1}{\partial u}$ and the conjugate action variable

$$(2.6.9) \quad J = -\frac{\partial F_1}{\partial \psi} = \frac{1}{2\beta} \left(u^2 + (\beta u' + \alpha u)^2 \right) = \frac{1}{2}\epsilon,$$

where α is defined as in (2.5.11). Notice the relation to the emittance. Doing the canonical transformation we arrive at a new Hamiltonian \tilde{H}

$$(2.6.10) \quad \tilde{H} = H + \frac{\partial F_1}{\partial s} = \frac{J}{\beta},$$

and we have that $\psi' = \frac{\partial \tilde{H}}{\partial J} = \frac{1}{\beta(s)}$, consistent with (2.6.4). Since J is independent of ψ the action is an invariant

$$(2.6.11) \quad J' = -\frac{\partial \tilde{H}}{\partial \psi} = 0$$

and the transformations between the two sets of phase-space coordinates are given by the expressions in (2.6.12).

$$(2.6.12) \quad u = \sqrt{2\beta J} \cos \psi, \quad u' = -\sqrt{\frac{2J}{\beta}} (\sin \psi + \alpha \cos \psi)$$

Consider now the generating function F_2 given in formula (2.6.13)

$$(2.6.13) \quad F_2(\psi, \bar{J}) = \left(\psi + \int_0^s \frac{ds}{\beta} + \nu \theta \right) \bar{J}, \quad \text{with } \theta = \frac{s}{R}, \bar{J} = J$$

with $\theta = \frac{s}{R}$ the orbiting angle of the reference orbit in the accelerator [16] and ν the Betatron Oscillation Frequency. With this generating function the Hamiltonian becomes

$$\bar{H} = R\tilde{H} = \nu \bar{J},$$

and the conjugate phase-space coordinates are (ψ, \bar{J}) , the action-angle variables. These conjugate phase-space coordinates are often used in accelerator physics and are useful for analyzing resonances caused by non-linear elements.

2.7. Emittance considerations

In this section I would like to give some remarks on the concept of emittance following [16]. Particles in an accelerator beam have a certain distribution in phase-space. Usually a certain distribution is assumed that can be written down in an analytical form, such as for example a Gaussian distribution. Suppose we have a normalized distribution function $\rho(x, x')$ with $\int \rho(x, x') dx dx' = 1$. The first and second moments are then given by equations (2.7.1) where σ_x and $\sigma_{x'}$ are the RMS (Root Mean Square) beam widths. $\sigma_{xx'}$ is the correlation and r is called the correlation coefficient.

$$(2.7.1) \quad \begin{aligned} \langle x \rangle &= \int x \rho(x, x') dx dx' \\ \langle x' \rangle &= \int x' \rho(x, x') dx dx' \\ \sigma_x^2 &= \int (x - \langle x \rangle)^2 \rho(x, x') dx dx' \\ \sigma_{x'}^2 &= \int (x' - \langle x' \rangle)^2 \rho(x, x') dx dx' \\ \sigma_{xx'}^2 &= \int (x - \langle x \rangle) (x' - \langle x' \rangle) \rho(x, x') dx dx' = r \sigma_x \sigma_{x'} \end{aligned}$$

Now define the RMS beam emittance as in (2.7.2). When neglecting dissipation and diffusion losses and assuming the accelerator contains only linear elements such as dipoles and quadrupoles this RMS emittance is a conserved quantity. So the “emittance” ϵ that was put equal to twice the Betatron Action in equation (2.6.9) is not really correct, but still is often used in accelerator physics in this way (I will use it in this

way in the rest of this text). Using this last interpretation of the “emittance” the Betatron Oscillations of a particle can be described by equation (2.7.3).

$$(2.7.2) \quad \epsilon_{RMS} = \sqrt{\sigma_x^2 \sigma_{x'}^2 - \sigma_{xx'}^2} = \sigma_x \sigma_{x'} \sqrt{1 - r^2}$$

$$(2.7.3) \quad x(s) = \sqrt{\epsilon \beta} \cos[\nu \phi(s) + \delta]$$

The RMS beam size is given by $\sqrt{\beta(s)\epsilon}$ and its RMS divergence by $\sqrt{\gamma(s)\epsilon}$. Note that $\gamma = \frac{1+\alpha^2}{\beta}$, showing that in regions of the accelerator where β is large the particles will travel on a more or less parallel trajectory. This is a condition that is highly requested by the experiment groups in the LHC because of the improved accuracy on the transverse momentum measurements of the outgoing particles in the collisions at the different interaction points. At the time of writing of this text the β values at the interaction points were squeezed to 3.5 meter (for ATLAS and CMS) while requests are made for β values of 90 meter up to 2.6 kilometer. The reason for this squeeze is to increase luminosity at the interaction points with the low intensities (= number of particles in the beams) that were used in the LHC at the time of writing with respect to the nominal design intensities. At the moment of writing this was a trade-off to optimize the physics conditions in the experiments.

Returning to the emittance, one can define the so called σ -matrix (equation (2.7.4)) using the momenta in equations (2.7.1).

$$(2.7.4) \quad \sigma = \begin{pmatrix} \sigma_x^2 & \sigma_{xx'} \\ \sigma_{xx'} & \sigma_{x'}^2 \end{pmatrix} = \langle (\mathbf{X} - \langle \mathbf{X} \rangle) (\mathbf{X} - \langle \mathbf{X} \rangle)^T \rangle$$

where \mathbf{X} is the Betatron State Vector. Using the σ -matrix³ the RMS emittance can be written as $\epsilon_{RMS} = \sqrt{\det[\sigma]}$.

The concept of emittance is very handy in describing the motion of particles in the beam but one needs to be prudent of the used definition.

2.8. The Dispersion Function

Until now we only considered particles with a momentum equal to that of the reference particle (ideal particles or so called on-momentum particles). Let us now look what happens when particles have a small deviation from this reference impulse (Δp). (A treatment of the effects on the longitudinal motion of this is given in Chapter 3, but here we only consider the transverse effects for off-momentum particles. Calculations in this section are based on the references [5, 16].

From equation (2.5.11) we have that the emittance is equal to the area of the ellipse in phase-space. Since this is a constant of motion this area is constant as long as we are considering on-momentum particles and discard dissipative or dispersive phenomena. For off-momentum particles the emittance can no longer be considered as a constant of motion. The fact that the beam emittance is a constant for on-momentum particles originates in Liouville's Theorem:

$$(2.8.1) \quad \int pdq = \text{constant},$$

where (q, p) are the canonical phase-space coordinates. It is important to be aware that in the calculations that follow the factors β and γ refer to the relativistic factors and not to the Optical Functions ! Using

$$(2.8.2) \quad x' = \frac{dx}{ds} = \frac{dx}{dt} \frac{dt}{ds} = \frac{\beta_x}{\beta},$$

where β_x is the relativistic factor in the x-direction, Liouville's Theorem can be rewritten as

$$(2.8.3) \quad \int pdq = mc \int \gamma \beta_x dx = mc \gamma \beta \int x' dx$$

³The matrix formalism (see subsection 2.5.1) can also be applied to this σ -matrix

$$\sigma(s_2) = M(s_2, s_1) \sigma(s_1) M^T(s_2, s_1).$$

This means that the beam emittance is proportional to $\frac{1}{\beta\gamma}$

$$(2.8.4) \quad \epsilon = \int x' dx \propto \frac{1}{\beta\gamma}$$

and results in a more convenient parameter used in accelerator physics, the Normalized Beam Emittance ϵ_N :

$$(2.8.5) \quad \epsilon_N = \beta\gamma\epsilon,$$

which is a constant of motion even during acceleration (or for off-momentum particles). Defining δ as $\frac{\Delta p}{p_0}$ we can rewrite equation (2.4.1) to first order in $\frac{x}{\rho}$ as (see Appendix B for the derivation)

$$(2.8.6) \quad x'' + x \left(\frac{1 - \delta}{\rho^2 (1 + \delta)} - \frac{K(s)}{1 + \delta} \right) = \frac{\delta}{(1 + \delta)\rho},$$

a non-homogeneous differential equation. Remember that solutions of such a type of differential equation can be written as a sum of a particular solution for the complete non-homogeneous equation and a linear combination of the solutions for the homogeneous equation. The Dispersion Function $D(s)$ is then defined as this particular solution normalized to δ . Physically the Dispersion Function represents the orbit of a particle for which $\delta = 1$, meaning that it satisfies the equation of motion (to lowest order in δ)

$$(2.8.7) \quad D'' + K_x(s) D = \frac{1}{\rho}, \quad \text{with } K_x(s) = \frac{1}{\rho^2} - K(s)$$

and that it is also influenced by the focusing properties of the optical elements of the accelerator. The orbit of a general particle can then be written as $x(s) = D(s)\delta + x_\beta(s)$ where $x_\beta(s)$ is a linear combination of independent solutions of the homogeneous equations. Notice that due to the periodicity of all the functions involved the Dispersion Function also needs to be periodic. Similar equations can be written down in the y-plane.

The matrices defined in the matrix formalism section (2.5.1) can be extended to include the Dispersion, in this way we end up with a 3 x 3 transfer matrix (for each transverse plane) as can be seen in equation (2.8.8).

$$(2.8.8) \quad \begin{pmatrix} x \\ x' \\ \delta \end{pmatrix} = \begin{pmatrix} M_{11} & M_{12} & D \\ M_{21} & M_{22} & D' \\ 0 & 0 & 1 \end{pmatrix} \begin{pmatrix} x \\ x' \\ \delta \end{pmatrix}_0$$

Notice that the Dispersion contributes to the beam size, demonstrating that one will need to take measures to suppress the Dispersion at the interaction points.

An expression for the Dispersion is given in (2.8.9) (the prove can be found in Appendix C ,[5, 16])

$$(2.8.9) \quad D(s) = M_{22}(s) \int_{s_0}^s \frac{1}{\rho} M_{11}(\tilde{s}) d\tilde{s} - M_{11}(s) \int_{s_0}^s \frac{1}{\rho} M_{22}(\tilde{s}) d\tilde{s}$$

Below we show some examples of the Dispersion Function for some common optical elements:

(1) Drift space: Starting from the Transfer Matrix

$$(2.8.10) \quad M_d = \begin{pmatrix} 1 & l \\ 0 & 1 \end{pmatrix}$$

for a drift space and using equation (2.8.9) we can calculate the Dispersion Function.

$$(2.8.11) \quad D(s) = l \left(\frac{s_1 - s_0}{\rho} \right) - l \left(\frac{s_1 - s_0}{\rho} \right) = 0$$

We conclude that a drift space does not contribute to the dispersion.

(2) Dipole: Again starting from the Transfer Matrix

$$(2.8.12) \quad M_F = \begin{pmatrix} \cos(\sqrt{K}l) & \frac{1}{\sqrt{K}} \sin(\sqrt{K}l) \\ -\sqrt{K} \sin(\sqrt{K}l) & \cos(\sqrt{K}l) \end{pmatrix}, \quad \text{with } K = \frac{1}{\rho^2}$$

which can be simplified to

$$(2.8.13) \quad M_{dip} = \begin{pmatrix} \cos\left(\frac{l}{\rho}\right) & \rho \sin\left(\frac{l}{\rho}\right) \\ -\frac{1}{\rho} \sin\left(\frac{l}{\rho}\right) & \cos\left(\frac{l}{\rho}\right) \end{pmatrix}.$$

With this Transfer Matrix the Dispersion becomes

$$(2.8.14) \quad \begin{aligned} D(s) &= \rho \sin\left(\frac{l}{\rho}\right) \int_0^l \frac{1}{\rho} \cos\left(\frac{s}{\rho}\right) ds - \cos\left(\frac{l}{\rho}\right) \int_0^l \frac{1}{\rho} \sin\left(\frac{s}{\rho}\right) ds \\ &= \rho \sin\left(\frac{l}{\rho}\right) \left(\sin\left(\frac{l}{\rho}\right) - 0\right) + \rho \cos\left(\frac{l}{\rho}\right) \left(\cos\left(\frac{l}{\rho}\right) - 1\right) \\ &= \rho \sin^2\left(\frac{l}{\rho}\right) + \rho \cos^2\left(\frac{l}{\rho}\right) - \rho \cos\left(\frac{l}{\rho}\right) \\ &= \rho \left(1 - \cos\left(\frac{l}{\rho}\right)\right) \end{aligned}$$

We conclude that a dipole magnet does contribute to the dispersion. Notice that the dispersion is generated in the plane of bending, this means that in an ideal situation there will be no dispersion generated in the vertical plane (ideal Quadrupoles don't contribute to dispersion, as can be seen from the matrix (2.8.12)). Of course this is the ideal situation, in reality magnets are not ideal. Magnets have errors in their magnetic fields or are misaligned. For instance if a dipole would be rotated a little, with the rotation axis being in the direction of the beam, this would generate Dispersion in the horizontal and vertical plane.

The last example shows that the system is very sensitive to even the slightest misalignment or field error. We will have to deal with non-ideal situations, in the next section we will consider an example of a magnet error and the effect on the equations of motion.

2.9. Magnet Errors : An example

We will use the example of a quadrupole error to demonstrate some of the possible effects magnet errors can induce in the accelerator machine.

Let us start by taking a look at the ideal transfer matrices for a focusing quadrupole (focusing in the horizontal plane) in the thin lens approximation.⁴

$$(2.9.1) \quad M_x = \begin{pmatrix} 1 & 0 \\ \frac{1}{f} & 1 \end{pmatrix} \quad M_y = \begin{pmatrix} 1 & 0 \\ -\frac{1}{f} & 1 \end{pmatrix} \quad \text{with } f \text{ the focal length of the MQ.}$$

We now define the transfer matrix for a quadrupole error as

$$(2.9.2) \quad M_{error} = \begin{pmatrix} 1 & 0 \\ \Delta kds & 1 \end{pmatrix},$$

and using this, the complete MQ Transfer Matrix becomes

$$(2.9.3) \quad M_{MQ} = M_{error} M_{ideal}.$$

Using the the full turn transfer matrix in the Twiss form this results in the matrix M_{MQ} (see equation (2.9.4)).

$$(2.9.4) \quad \begin{aligned} M_{MQ} &= \begin{pmatrix} 1 & 0 \\ \Delta kds & 1 \end{pmatrix} \begin{pmatrix} \cos(\psi_0) + \alpha_s \sin(\psi_0) & \beta_s \sin(\psi_0) \\ -\gamma_s \sin(\psi_0) & \cos(\psi_0) - \alpha_0 \sin(\psi_0) \end{pmatrix} \\ &= \begin{pmatrix} \cos(\psi_0) + \alpha_s \sin(\psi_0) & \beta_s \sin(\psi_0) \\ \Delta kds (\cos(\psi_0) + \alpha_s \sin(\psi_0)) - \gamma_s \sin(\psi_0) & \Delta kds (\beta_s \sin(\psi_0)) + \cos(\psi_0) - \alpha_0 \sin(\psi_0) \end{pmatrix} \end{aligned}$$

⁴The thin lens approximation is valid if $f = \frac{1}{kl_q} \gg l_q$ with $k = \frac{B_1}{B\rho}$ (equation 2.4.3)

Now identify the trace of this matrix M_{MQ} with $2 \cos(\psi)$ where $\psi = \psi_0 + \Delta\psi$ ⁵

$$(2.9.5) \quad \text{Tr}(M_{MQ}) = 2 \cos(\psi) = \cos(\psi_0) + \frac{\Delta k ds}{2} \beta \sin(\psi_0).$$

This allows us to write equation (2.9.6) for the Tune shift.

$$(2.9.6) \quad \Delta\psi = \frac{\Delta k ds}{2} \beta.$$

In subsection 2.5.3 we introduced the Tune concept from the Phase Advance per turn by $\psi = 2\pi Q$ where Q is the tune. As is clear from equation (2.9.6) the magnet error induces a change in the phase advance per turn and thus also in the Tune. The Tune shift is given by equation (2.9.7).

$$(2.9.7) \quad \Delta Q = \int_{s_0}^{s_0+l} \frac{\Delta k(s)}{4\pi} \beta(s) ds$$

Note that the Tune shift is proportional to the Beta-Function, this will introduce further restrictions for the beam operation in areas with high β values. Next to the effects of these errors on the Tune they also have an effect on the Beta-Functions, this effect is referred to as Beta-Beating. The Beta-Beating effect is very important because it can lead to resonances as will demonstrated in the example below.

The magnet field errors for a focusing quadrupole will generate a Beta-Beating $\Delta\beta$ given by equation (2.9.8).

$$(2.9.8) \quad \Delta\beta(s_0) = \frac{\beta_0}{2 \sin(2\pi Q)} \int_{s_0}^{s_0+l} \beta(s) \Delta K \cos(2|\psi_{s_1} - \psi_{s_0}| - 2\pi Q) ds$$

For the proof of this we follow [5]. Start by splitting the accelerator ring in two parts, which gives leads to two transfer matrices A and B that when combined form the full turn transfer matrix.

$$(2.9.9) \quad M = BA$$

As a next step introduce a quadrupole error in between the two parts of the ring.

$$\begin{aligned} M^* &= \begin{pmatrix} m_{11}^* & m_{12}^* \\ m_{21}^* & m_{22}^* \end{pmatrix} \\ &= B \begin{pmatrix} 1 & 0 \\ -\Delta k ds & 1 \end{pmatrix} A \\ &= B \begin{pmatrix} a_{11} & a_{12} \\ -\Delta k ds a_{11} + a_{21} & -\Delta k ds a_{12} + a_{22} \end{pmatrix} \\ &= \begin{pmatrix} b_{11}a_{11} + b_{12}(-\Delta k ds a_{11} + a_{21}) & b_{11}a_{12} + b_{12}(-\Delta k ds a_{12} + a_{22}) \\ b_{21}a_{11} + b_{22}(-\Delta k ds a_{11} + a_{21}) & b_{21}a_{12} + b_{22}(-\Delta k ds a_{12} + a_{22}) \end{pmatrix} \end{aligned}$$

Remember from the previous sections that

$$\begin{aligned} m_{12} &= \beta_0 \sin(2\pi Q) \\ &= b_{11}a_{12} + b_{12}a_{22} \end{aligned}$$

This results in

$$(2.9.10) \quad m_{12}^* = \beta_0 \sin(2\pi Q) - a_{12}b_{12}\Delta k ds.$$

Since M^* is also for a full turn we can rewrite m_{12}^* as

$$(2.9.11) \quad m_{12}^* = (\beta_0 + d\beta) \sin(2\pi M(Q + dQ)).$$

Putting the last two equations equal

$$\begin{aligned} \beta_0 \sin(2\pi Q) - a_{12}b_{12}\Delta k ds &= (\beta_0 + d\beta) \sin(2\pi(Q + dQ)) \\ (2.9.12) \quad &= (\beta_0 + d\beta) (\sin(2\pi Q) \cos(2\pi dQ) + \cos(2\pi Q) \sin(2\pi dQ)). \end{aligned}$$

⁵Assuming $\Delta\psi$ very small so that $\cos(\psi) = \cos(\psi_0) + \frac{\Delta k ds}{2} \beta \sin(\psi_0)$

Now using $\cos(2\pi dQ) \cong 1$, $\sin(2\pi dQ) = 2\pi dQ$ and ignoring the second order terms we arrive at the following expression

$$(2.9.13) \quad -a_{12}b_{12}\Delta kds = \beta_0 2\pi dQ \cos(2\pi Q) + d\beta \sin(2\pi Q).$$

We can rewrite this last equation by introducing $dQ = \frac{\beta_1 \Delta kds}{4\pi}$ (where the 1 refers to the location of the error).

$$(2.9.14) \quad -a_{12}b_{12}\Delta kds = \frac{\beta_1 \Delta kds}{4\pi} \cos(2\pi Q) + d\beta \sin(2\pi Q).$$

Reordering the different terms gives us an expression for $d\beta_0$

$$(2.9.15) \quad d\beta_0 = -\frac{1}{2\pi \sin(2\pi Q)} (2a_{12}b_{12} + \beta_0 \beta_1 \cos(2\pi Q)) \Delta kds.$$

To arrive at the final result express the parameters a and b in terms of the Optical Functions.

$$(2.9.16) \quad a_{12} = \sqrt{\beta_0 \beta_1} \sin(\Delta\psi_{0 \rightarrow 1})$$

$$(2.9.17) \quad b_{12} = \sqrt{\beta_0 \beta_1} \sin(2\pi Q - \Delta\psi_{0 \rightarrow 1})$$

The final result of these calculations is represented by expression (2.9.18)

$$(2.9.18) \quad \Delta\beta(s_0) = \frac{\beta_0}{2 \sin(2\pi Q)} \int_{s_0}^{s_0+l} \beta(s) \Delta K \cos(2|\psi_{s_1} - \psi_{s_0}| - 2\pi Q) ds.$$

Notice that this contains a resonance factor $\sin(2\pi Q)$ as mentioned before.

It should be clear from the example described here that magnet errors can create very strong effects in the machine. These errors can come from very different causes: alignment errors, field errors, current instabilities during operation, and so on. But whatever their cause one will need to compensate for them during machine operation.

2.10. Chromaticity Q'

For a quadrupole the focusing strength is given by $k = \frac{g}{p/e}$. We also know that for any particle in the beam $p = p_0 + \Delta p$. By inserting the second equation in the first it becomes clear that the quadrupole acts on an off-momentum particle as if it has an error (see equation (2.10.1)).

$$(2.10.1) \quad k = \frac{e}{p_0} \left(1 - \frac{\Delta p}{p_0} \right) g$$

$$(2.10.2) \quad = k_0 + \Delta k$$

This “error” will generate a Tune spread given by equation (2.10.3)

$$(2.10.3) \quad \Delta Q = -\frac{1}{4\pi} \frac{\Delta p}{p_0} k_0 \beta(s) ds.$$

The Chromaticity Q' is then defined by this Tune spread normalized to $\frac{\Delta p}{p}$.

$$(2.10.4) \quad \Delta Q = Q' \frac{\Delta p}{p}$$

$$(2.10.5) \quad = -\frac{1}{4\pi} \oint k(s) \beta(s) ds$$

As in section 2.9 on magnet errors the Tune spread generates a resonance factor for $\beta(s)$, which is related to the beam size by $\sigma = \sqrt{\beta\epsilon}$. If stable beams are desired we will need to keep the machine away from these resonant Tunes ($mQ_x + nQ_y + lQ_s \notin \mathbb{Z}$). Note that Chromaticity is generated by the machine itself, the moment focusing elements (factor $k(s)$) are introduced in the accelerator Chromaticity is also introduced. Hence we need ways to correct for this, which is usually done by introducing sextupoles in the machine. This adds to the Chromaticity as

$$(2.10.6) \quad Q' = -\frac{1}{4\pi} \oint (k(s) - mD(s)) \beta(s) ds,$$

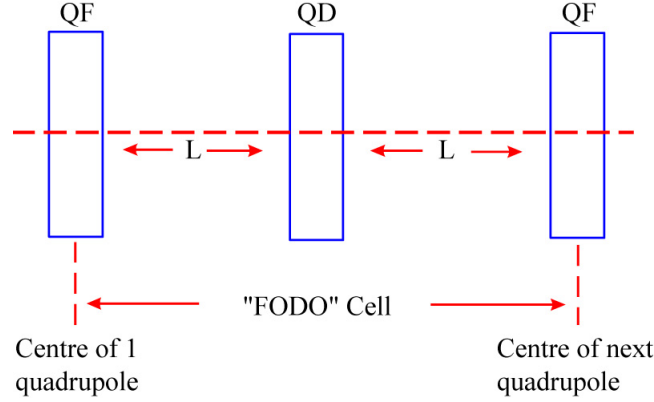


FIGURE 2.11.1. Fodo-cell

with $B_x = gxy$, $B_y = \frac{1}{2}g(x^2 - y^2)$ and $m = \frac{gx}{p/e}$. Re-investigating the expansion for the magnetic fields $B = B_0 + x \frac{\partial B}{\partial x} + x^2 \frac{\partial^2 B}{\partial x^2} + \dots$ reveal that dipole errors need to be corrected with quadrupoles, quadrupole errors need to be corrected with sextupoles, and so on...

This does not mean that it is impossible to build a working machine, but it does mean that construction and operation of an accelerator is far from obvious. To estimate the influence of these resonant effects and magnet errors (some influence the beam more than others) accelerator physicists depend highly on simulations because a full analytical treatment is obviously impossible.

2.11. Toy model accelerator

In this final section of the chapter on transverse beam dynamics I would like to show the behavior of a beam in a toy model accelerator to give the reader an idea of how drift spaces, dipoles and quadrupoles influence the beam size and the particles transverse phase-space coordinates. This toy model is far from realistic but it does show some of the beam behavior that can be seen in real machines.

My toy model accelerator is constructed of four dipole magnets and four so called Fodo-cells. A Fodo cell is a combination of three MQ's and two drift spaces separating the three MQ's (figure 2.11.1). A Fodo-cell has two focusing and one defocusing MQ in one of the transverse planes. As by construction this means that in the other transverse plane the Fodo-cell has two defocusing and one focusing MQ. If one chooses the length of the drift spaces and the strengths of the MQ's correctly the Fodo-cell will have a focusing effect in both transverse planes.

The dipoles and Fodo-cells are separated by drift spaces in my toy model (figure 2.11.2.). To generate the beam in my toy model I used a Gaussian distribution in all the transverse phase-space coordinates of two thousand particles. In figure 2.11.3 I show the beam and the phase-space coordinates in both transverse planes before and after a drift space. It is clear that the beam size is increasing. In figure 2.11.4 I show the same plots for a bending magnet. It should be clear that the ellipses are rotating in phase-space. Figure 2.11.5 shows again the same plots for the used Fodo-cell. Although the beam size is larger after the Fodo-cell the phase-space plots show that the beam is converging (the ellipses rotate to the right, thus reducing the beam size). Figure 2.11.6 compares the beam after one turn and after five hundred turns with the initial beam. These plots show that the beam is stable. To conclude the sets of plots I show in figure 2.11.7 the phase-space trajectories for two particles in the beam, as expected they describe ellipses. An interesting observation to make is the difference in the Tunes for both planes. In the y-plane the particles almost follow a periodic set of points in phase-space demonstrating that the decimal part of the tune $decimal[Q_y] \approx decimal[\frac{2\pi}{n}]$ with n an integer while in the x-plane this is not the case.

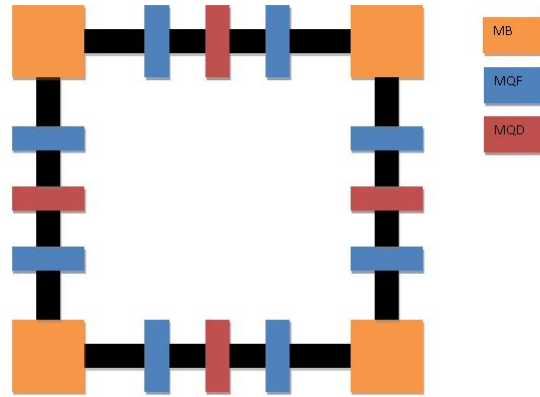


FIGURE 2.11.2. Toy Model Accelerator

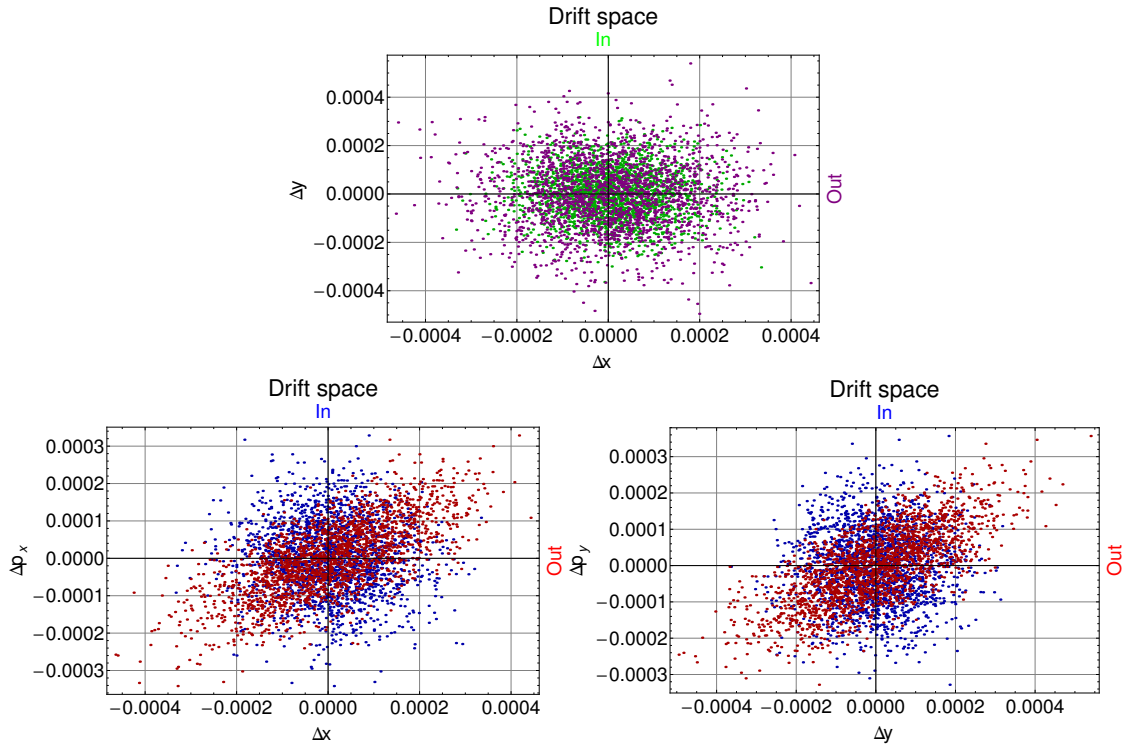


FIGURE 2.11.3. Drift space

2.12. Summary

In this chapter I gave a short introduction to transverse beam dynamics. I started by defining the coordinate system used throughout this text (a Frenet-Serret system) and derived an expression for the Hamiltonian describing the transverse dynamics in this system (equation 2.2.16). This Hamiltonian depends on the magnetic fields produced by the different elements in the accelerator so that there was a need to also express these fields in the Frenet-Serret coordinates where the Bethe representation was used (equations 2.3.8). After having derived these expressions for the fields I restricted myself to the linear terms to derive

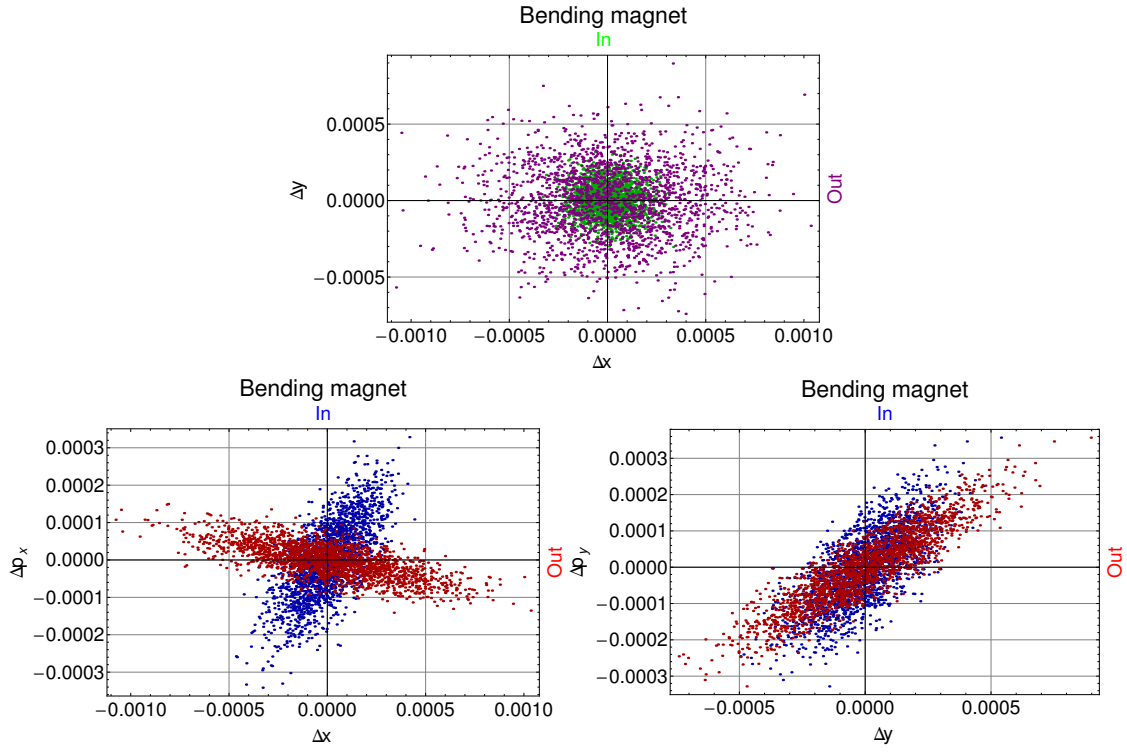


FIGURE 2.11.4. Bending Magnet

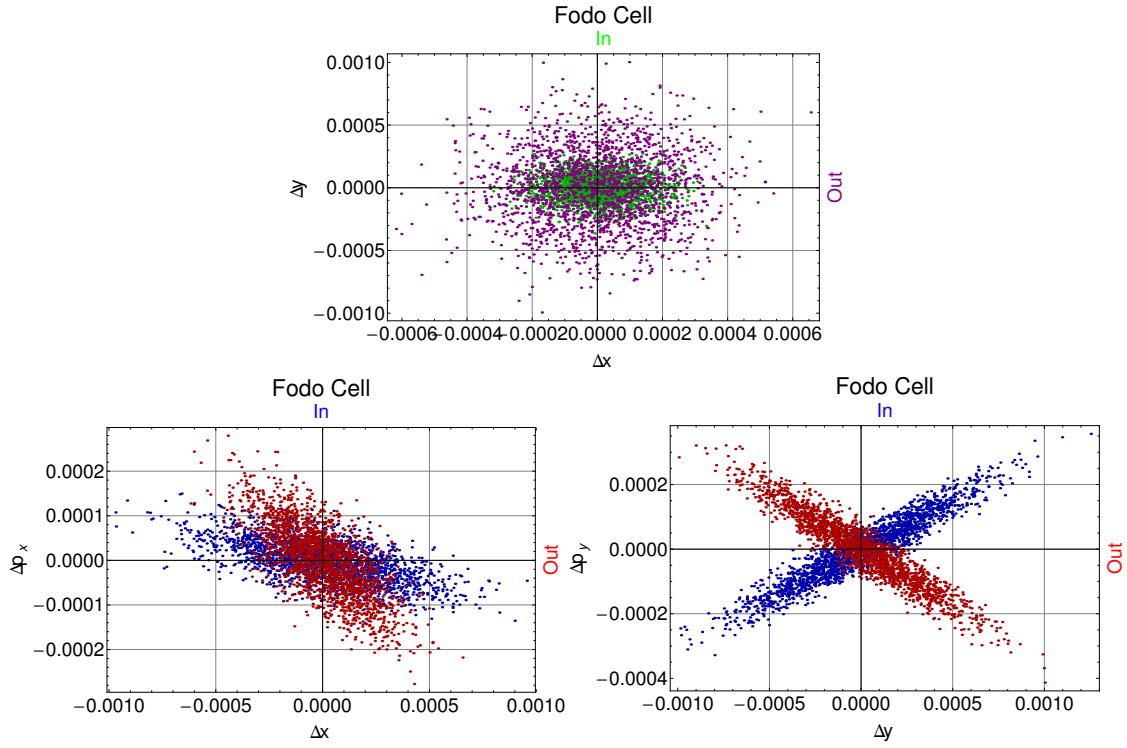


FIGURE 2.11.5. FODO-cell

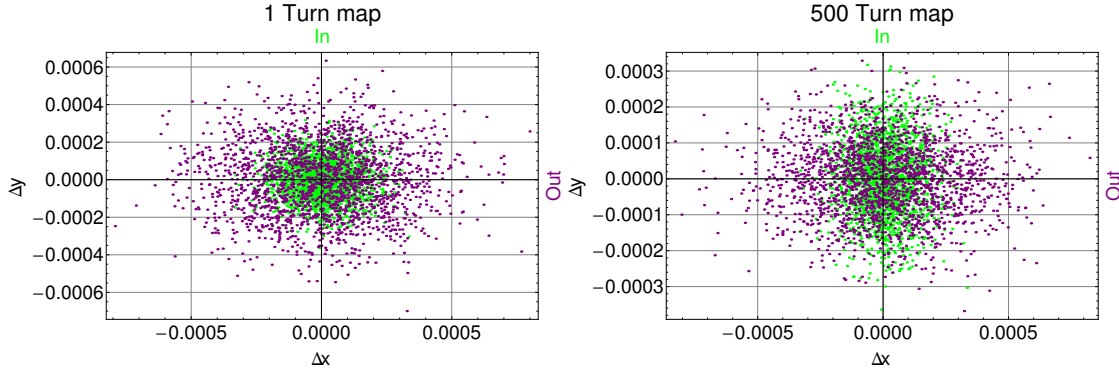


FIGURE 2.11.6. Beam after 1 and after 500 turns

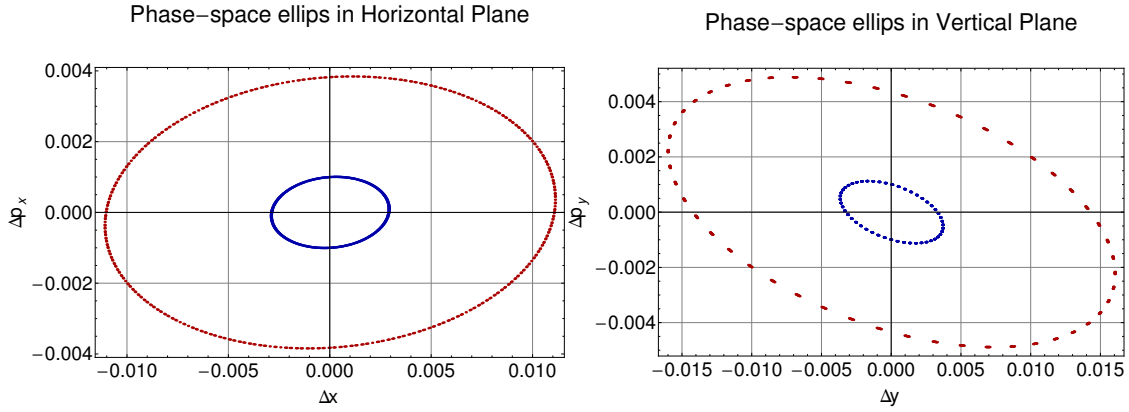


FIGURE 2.11.7. Phase-space trajectories of two particles

the equations describing the Betatron motion, a set of second order differential equations shown in 2.4.1. These equations turn out to be of the class of Hill's equations (equation 2.4.2 shows the general form of this type of equations). The solutions of the Hill's equations then allowed to introduce a matrix formalism to calculate changes along the accelerator ring of the transverse phase-space coordinates. Using this matrix formalism a stability condition for the Betatron motion was derived putting limits on the allowed values of the elements in the transfer matrices. The solutions of the Hill's equations defined the Optical Functions, which are also known as the Twiss parameters or Courant-Snyder parameters (equations 2.5.8), and the beam emittance. Using these Optical Functions the concept of Phase-Advance and Tune were introduced (equations 2.5.9 and 2.5.10). It was shown that the matrix formalism can be extended to these Optical Functions. Some examples of the phase-space behavior of a particle in the beam are shown in subsection 2.5.5. After introducing the Action-Angle variables I discussed the beam emittance a little bit more in depth because different definitions exist in the literature. Next the Dispersion Function was introduced (equation 2.8.9) and its contribution to the transverse coordinates discussed. In section 2.9 a short discussion of the effects of magnet errors was given by using the example of a quadrupole error. This allowed to introduce the concepts Tune-shift (equation 2.9.7), Beta-beating (equation 2.9.18) and Chromaticity (equation 2.10.6). I concluded this chapter on transverse dynamics by demonstrating the behavior of a simulated beam in the most basic parts of a circular accelerator by use of a Toy Model accelerator.

CHAPTER 3

Longitudinal Dynamics

3.1. Basic equations dynamics equation

For accelerating particles electric fields are used over magnetic fields since static magnetic fields are unable to deliver work. The set of equations (3.1.1) give some basic relations between the dynamic parameters that are relevant for describing the longitudinal motion of particles in an accelerator beam.

$$\begin{aligned}
 \frac{d\vec{p}}{dt} &= e\vec{E} \\
 E^2 &= m^2c^4 + p^2c^2 \\
 2EdE &= 2pd p \\
 dE &= \frac{p}{E} dp \\
 E &= \gamma m_0 c^2 \\
 p &= \gamma m_0 v \\
 v &= \frac{pc^2}{E}
 \end{aligned}
 \tag{3.1.1}$$

3.2. The Accelerating Component: The RF Cavity

The purpose of an accelerator is to accelerate particles but until now we have only discussed elements in an accelerator that are passive in the sense that they do not accelerate the particles. The accelerating parts in most synchrotron's today are Resonant Radio Frequency Cavities. As the the name already states, these cavities are designed to resonate at a certain frequency. In the LHC superconducting RF Cavities are used operating at voltages as high as sixteen Mega Volts and operating at frequencies around 400.8 Mega Hertz. With this frequency for the electric fields in the cavities the revolution frequency for the particles is 11245 Hertz at collision energy.

The fact that such high voltage fields are used and that the operating frequencies are so high makes the design of RF Cavities very difficult and requires specific knowledge. It is a separate field in accelerator physics and a treatment of this subject falls outside of this text. In figure 3.2.1 I show a diagram of one of the superconducting cavities of the LHC and how they are implemented in the machine.

3.3. Transit Time Factor

The time a particle takes to go through an RF Cavity will strongly effect the field that it will see because the fields in the RF Cavity are time dependent. In the study of the particles motion in the following sections (based on calculations and discussions in [16, 23, 9]) the approximation that the field is homogeneous and constant at a certain moment in time (pointing in the s direction) is made. For simplicity only the ground tone is considered to be present in the RF Cavity¹ so that the field in one of the cavities can be expressed

¹An RF cavity is basically an RF resonator, so next to the ground tone, usually one also has to deal with all the different allowed harmonics.

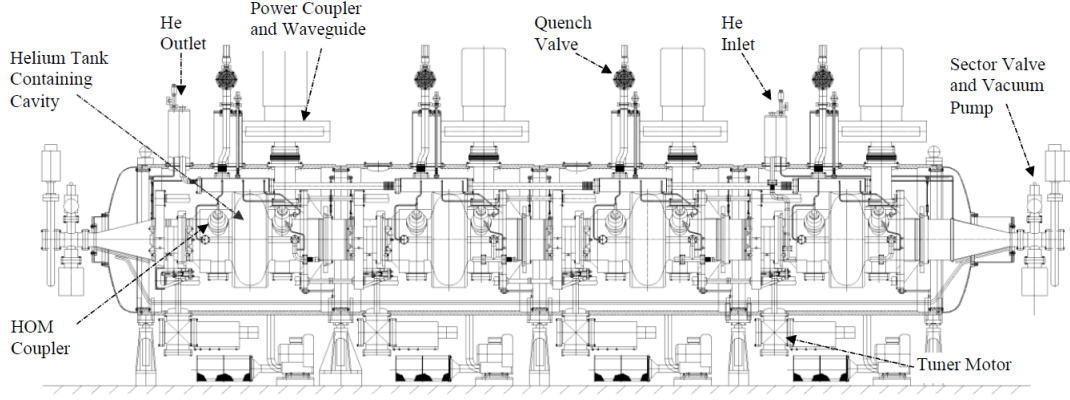


FIGURE 3.2.1. RF Cavity (from [2] Chapter 6)

as in expression (3.3.1).

$$\begin{aligned}
 E_s &= E_0 \sin(\omega t + \phi_s) \\
 (3.3.1) \quad &= \frac{V}{g} \sin(\omega t + \phi_s),
 \end{aligned}$$

with g the gap width of the cavity, $\omega = h\omega_0$ where h is the harmonic number and $\omega_0 = \frac{\beta_0 c}{R_0}$ (the zero is referring to the synchronous particle, see section 3.4). Assume a particle passes $s = 0$, the center of the cavity, at the times $t = nT_0 + [-\frac{g}{2}\beta_0 c, \frac{g}{2}\beta_0 c]$ in the positive s direction (assume the particle has unit charge e). We now want to calculate the energy gain for this particle, we do this by integrating over the field the particle sees during the time it passes through the cavity.

$$(3.3.2) \quad \Delta E = \frac{eV}{g} \beta_0 c \int_{-\frac{g}{2}\beta_0 c}^{\frac{g}{2}\beta_0 c} \sin(h\omega_0 t + \phi_s) dt$$

$$(3.3.3) \quad = eVT \sin \phi_s, \text{ with } T \text{ the Transit Time Factor}$$

Notice that for the Transit Time Factor defined in equation (3.3.3) we have $0 < T < 1$. Cavities are usually designed to have a T value around 0.6. Changing to the general case and using a complex phasor notation, the energy gain can be written as in equation (3.3.4).

$$(3.3.4) \quad \Delta E = e \left| \int_{-\frac{g}{2}\beta_0 c}^{\frac{g}{2}\beta_0 c} E_s(t) \exp(jh\omega_0 t) dt \right| \sin \phi_s, j^2 = -1$$

$$(3.3.5) \quad T = \frac{\sin\left(\frac{hg}{2R_0}\right)}{\left(\frac{hg}{2R_0}\right)},$$

with ϕ_s the phase of the particle with respect to the RF field. For small gap widths (g) T is close to 1.

3.4. Phase-Stability

To explain the concept of phase-stability we start by considering a series of RF cavities operating in 2π -mode. For cavities operating in 2π -mode the field is the same in the different cavities at each moment in time. We now want to investigate the effects of the phase ϕ of the waveform in the cavities when the particle enters the cavity on the particles behavior.

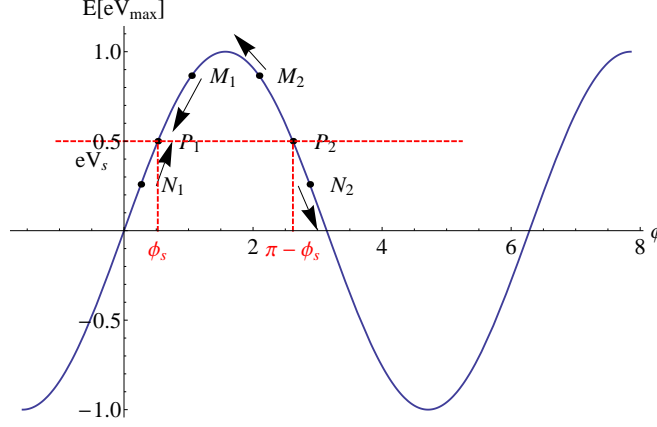


FIGURE 3.4.1. Phase-Stability

In figure 3.4.1 one can see that there exists a ϕ_s so that the particle sees the same field in each cavity, ie. the particles movement through the cavities is synchronized with the RF field in the cavities. The orbit of such a particle is called the synchronous orbit, and such a particle is referred to as a synchronous particle. Considering now a particle entering the first cavity at point M_1 in figure 3.4.1. This particle is spatially behind the synchronous particle seen from the RF cavity. The plot shows that this particle sees a larger accelerating field compared to the synchronous particle so that it is accelerated more than the synchronous particle. As a consequence the point M_1 will move towards point p_1 when the particle moves through the cavities. Applying a similar reasoning to the particle in point N_1 gives a similar result, the point N_1 will move to the point p_1 . This effect is called The Principle of Phase-Stability.

Now applying a similar reasoning to p_2 , with M_2 and N_2 show that the point p_2 is an unstable point, the points M_2 and N_2 will move away from it (below transition energy, above transition energy it will be the other way around, see section 3.5 for a discussion of this).

Important to note is that particles with a non-synchronous phase around the point p_1 will overshoot this point and thus will oscillate around the stable point or synchronous particle (see section 3.7 on The Synchrotron Motion).

The Principle of Phase-Stability should make it clear that when one would put a continuous beam in the accelerator the RF cavities will automatically transform the continuous beam into a bunched beam.

Important to remember from this section is that there exists a particle, the synchronous particle, that is synchronized with the RF wave field that has a frequency of $\omega_{rf} = h\omega_0$ with ω_0 defined as in section 3.3 and h is an integer, called the harmonic number of the accelerator. In this way the synchronous particle sees the RF cavity field at the same phase angle on every pass (ϕ_s). In the next sections we will study the behavior of particles that deviate slightly from the synchronous particle with respect to the phase of the fields in the cavities.

3.5. Momentum Compaction Factor, Phase-slip Factor and the Transition Energy

Deviations from the ideal orbit in one of the transverse directions will give rise to a change in the orbit length per turn. The deviation of the orbit length with respect to the ideal orbit length can be given by equation (3.5.1) (see section 2.8, [16, 23]).

$$(3.5.1) \quad \Delta L = \oint \frac{x}{\rho} ds = \left[\oint \frac{D(s)}{\rho} ds \right] \delta$$

with $\delta = \frac{\Delta p}{p_0}$. From this we can define The Momentum Compaction Factor α_c

$$(3.5.2) \quad \alpha_c \equiv \frac{1}{L_0} \frac{d\Delta L}{d\delta} = \frac{1}{L_0} \oint \frac{D(s)}{\rho(s)} ds.$$

The revolution period of a particle is $T = \frac{L}{\nu}$, with L the path length for one complete turn in the machine and ν the speed of the particle in the lab frame. Comparing the deviation of the revolution period for an off-momentum particle with the revolution period of an on-momentum particle allows to define the phase-slip factor η and the Transition Energy γ_T .

$$(3.5.3) \quad \frac{\Delta T}{T_0} = \frac{\frac{L}{\nu} - \frac{L_0}{\nu_0}}{\frac{L_0}{\nu_0}} = \frac{\nu_0 L}{L_0 \nu} - 1 = \frac{\nu_0 L - \nu L_0 + L_0 \nu_0 - L_0 \nu_0}{L_0 \nu}$$

$$(3.5.4) \quad = \frac{\Delta L}{L_0} - \frac{\Delta \beta}{\beta}$$

From equation (3.5.2) we have that

$$(3.5.5) \quad \frac{\Delta L}{L_0} = \alpha_c \delta$$

and using

$$(3.5.6) \quad cp = \beta E$$

$$(3.5.7) \quad cdp = E d\beta + \beta dE$$

$$(3.5.8) \quad \frac{dp}{p} = \frac{d\beta}{\beta} + \frac{dE}{E}$$

together with

$$(3.5.9) \quad \frac{dE}{E} = \beta^2 \frac{dp}{p}$$

$$(3.5.10) \quad \frac{d\beta}{\beta} = \frac{1}{\gamma^2} \frac{dp}{p}$$

$$(3.5.11) \quad \gamma = \frac{E}{mc^2}$$

finally results in expression (3.5.14) for the Phase-slip Factor η .

$$(3.5.12) \quad \frac{\Delta T}{T_0} = \left(\alpha_c - \frac{1}{\gamma^2} \right) \frac{dp}{p}$$

$$(3.5.13) \quad = \eta \delta$$

$$(3.5.14) \quad \eta = \left(\alpha_c - \frac{1}{\gamma^2} \right) = \frac{\frac{\Delta T}{T_0}}{\frac{dp}{p}}$$

Expressing this last equation in revolution frequencies and pulsations instead of revolution periods:

$$(3.5.15) \quad \frac{\Delta T}{T_0} = \frac{\frac{1}{f} - \frac{1}{f_0}}{\frac{1}{f_0}} = \frac{f_0 - f}{f} = -\frac{\Delta f}{f} = -\frac{\Delta \omega}{\omega_0},$$

$$(3.5.16) \quad \frac{\Delta \omega}{\omega_0} = -\eta \delta.$$

Notice the special value for γ or energy where the Phase-slip Factor vanishes, this is called the Transition Energy γ_T so that we can write expression (3.5.19) for the Phase-slip Factor.

$$(3.5.17) \quad \alpha_c = \frac{1}{\gamma_T^2}$$

$$(3.5.18) \quad \gamma_T = \frac{1}{\sqrt{\alpha_c}}$$

$$(3.5.19) \quad \eta = \frac{1}{\gamma_T^2} - \frac{1}{\gamma^2}$$

These are a nice set of equations and definitions but what do they mean?

From equation (3.5.5) it is clear that the Momentum Compaction Factor α_c relates the normalized change in path length for an off-momentum particle with the normalized deviation of the momentum of that particle with respect to an on-momentum particle.

The Phase-slip Factor η divides the off-momentum particles in two behavior classes. Below transition energy ($\eta < 0$) the revolution period is mainly determined by the speed of the particle, while for particle above transition energy ($\eta > 0$) the revolution period is mainly determined by the path length of the particle's trajectory. Looking at equation (3.5.16) shows for example that above transition particles with higher energy than the on-momentum particle will take longer to complete a turn with respect to the on-momentum particle. This is because Dispersion (see section 2.8) forces the particle with higher energy to have a larger bending radius and thus to have a longer orbit per machine turn.

3.6. Equations of motion

Here the acceleration rate equation (based on [23, 16]) for the synchronous particle will be derived from equation (3.3.4) leading to the equations of motion. From the relation between frequency and pulsation $f = \frac{\omega_0}{2\pi}$ we have the revolution frequency for the synchronous particle and the synchronous particles energy gain on each passage through the cavity is given by $eV \sin \phi_s$. Additionally we have assumed a small cavity gap so that the Transit Time Factor is close to one ($T \approx 1$). The energy gain per time can then be expressed in the form of equation (3.6.1).

$$(3.6.1) \quad \dot{E}_0 = \frac{\omega_0}{2\pi} eV \sin \phi_s,$$

with the overhead dot referring to the derivative with respect to time as before. The question is now, how to describe the motion of particles that deviate slightly from the synchronous particle, an off-momentum particle. To tackle this problem we introduce the parameters

$$(3.6.2) \quad \omega = \omega_0 + \Delta\omega$$

$$(3.6.3) \quad \phi = \phi_0 + \Delta\phi$$

$$(3.6.4) \quad \theta = \theta_0 + \Delta\theta$$

$$(3.6.5) \quad p = p_0 + \Delta p$$

$$(3.6.6) \quad E = E_0 + \Delta E$$

for such particles, where the parameters with the subscript zero refer to these parameters for the synchronous particle. From top to bottom they are the revolution frequency, the phase angle, the azimuthal orbital angle, the momentum and the energy of the considered particle. The equation that relates the orbital angle to the phase angle is given by

$$(3.6.7) \quad \Delta\omega = \frac{d}{dt} \Delta\theta = -\frac{1}{h} \frac{d}{dt} \Delta\phi = -\frac{1}{h} \frac{d\phi}{dt}.$$

The acceleration of an off-momentum particle is then given by

$$(3.6.8) \quad \dot{E} = \frac{\omega}{2\pi} eV \sin \phi.$$

Now doing some arithmetic

$$(3.6.9) \quad \frac{\dot{E}}{\omega} - \frac{\dot{E}_0}{\omega_0} = \frac{1}{2\pi} (\sin \phi - \sin \phi_0)$$

$$(3.6.10) \quad = \frac{1}{\omega_0} \left(\frac{\omega_0}{\omega} \dot{E} - \dot{E}_0 \right)$$

$$(3.6.11) \quad = \frac{1}{\omega_0} \left(\Delta \dot{E} - \frac{\omega - \omega_0}{\omega_0} \dot{E} \right)$$

$$(3.6.12) \quad = \frac{1}{\omega_0} \Delta \dot{E} - \dot{E} \frac{\Delta \omega}{\omega_0^2}$$

$$(3.6.13) \quad \approx \frac{1}{\omega_0} \Delta \dot{E} + \left[\dot{E} \frac{\Delta \left(\frac{1}{\omega_0} \right)}{\Delta E} \right] \Delta E + \dots$$

$$(3.6.14) \quad = \frac{d}{dt} \left(\frac{\Delta E}{\omega_0} \right)$$

gives us the equation of motion for the energy difference normalized to the revolution pulsation of the synchronous particle:

$$(3.6.15) \quad \frac{d}{dt} \left(\frac{\Delta E}{\omega_0} \right) = \frac{1}{2\pi} (\sin \phi - \sin \phi_0).$$

Defining the fractional off-momentum δ as $\delta = \frac{\Delta p}{p_0} = \frac{\omega_0 \Delta E}{\beta^2 E \omega_0}$, we can also write

$$(3.6.16) \quad \dot{\delta} = \frac{\omega_0}{2\pi \beta^2 E} eV (\sin \phi - \sin \phi_0)$$

Since the phase of a particle with respect to the RF field will determine its behavior with respect to the synchronous particle we would like to have an equation of motion for the particles phase ϕ . From equation (3.6.7)

$$(3.6.17) \quad \dot{\phi} = -h (\omega - \omega_0).$$

Using expression (3.6.18) for the angular velocity we can write expression (3.6.19) for the normalized pulsation change of the off-momentum particle.

$$(3.6.18) \quad \frac{\omega R}{\omega_0 R_0} = \frac{\beta}{\beta_0}$$

$$(3.6.19) \quad \frac{\Delta \omega}{\omega_0} = \frac{\beta R_0}{\beta_0 R} - 1$$

Expanding the mean radius R in a Taylor series in function of the normalized momentum deviation with respect to the synchronous particle $\left(\delta = \frac{\Delta p}{p_0} \right)$

$$(3.6.20) \quad R = R_0 (1 + \alpha_0 \delta + \alpha_1 \delta^2 + \dots)$$

$$(3.6.21) \quad \alpha_p = \frac{1}{R_0} \frac{dR}{d\delta} = \alpha_0 + 2\alpha_1 \delta + \dots$$

Rewriting the fractional off-momentum as

$$(3.6.22) \quad \delta = \frac{\Delta p}{p_0} = \frac{\beta \gamma}{\beta_0 \gamma_0} - 1$$

and using the relations between the relativistic parameters γ and β they can be expressed in function of the fractional off-momentum

$$(3.6.23) \quad \frac{\gamma}{\gamma_0} = \sqrt{1 + 2\beta_0^2 \delta + \beta_0^2 \delta^2}$$

$$(3.6.24) \quad \frac{\beta}{\beta_0} = \frac{1 + \delta}{\sqrt{1 + 2\beta_0^2 \delta + \beta_0^2 \delta^2}} = 1 + \frac{1}{\gamma_0^2} \delta - \frac{3\beta_0^2}{2\gamma_0^2} \delta^2 + \dots$$

Using equations (3.6.24) and (3.6.23) we can write the normalized pulsation change in function of the Phase-slip Factor

$$(3.6.25) \quad \frac{\Delta\omega}{\omega_0} = -\eta(\delta)\delta = -(\eta_0 + \eta_1\delta + \dots)\delta,$$

where

$$(3.6.26) \quad \eta_0 = \alpha_0 - \frac{1}{\gamma_0^2} \quad \eta_1 = \frac{3\beta_0^2}{2\gamma_0^2} + \alpha_1 - \alpha_0\eta_0.$$

This shows that equation (3.5.16) for the change in pulsation is only a linear approximation.

$$(3.6.27) \quad \Delta\omega = -\eta_0\omega_0\delta.$$

Using expression (3.6.27) in equation (3.6.17) the time evolution of the phase angle becomes

$$(3.6.28) \quad \dot{\phi} = h\omega_0\eta\delta = \frac{h\omega_0^2\eta}{\beta^2 E} \left(\frac{\Delta E}{\omega_0} \right)$$

Notice that $\left(\phi, \frac{\Delta E}{\omega_0}\right)$ or (ϕ, δ) are conjugate phase-space coordinates. With these phase-space coordinates the Synchrotron (or longitudinal) equations of motion can be summarized as

$$(3.6.29) \quad \begin{aligned} \frac{d}{dt} \left(\frac{\Delta E}{\omega_0} \right) &= \frac{eV}{2\pi} (\sin \phi - \sin \phi_0) \\ \dot{\phi} = h\omega_0\eta\delta &= \frac{h\omega_0^2\eta}{\beta^2 E} \left(\frac{\Delta E}{\omega_0} \right) \end{aligned}$$

3.7. Synchrotron Hamiltonian and Synchrotron motion

The equations of motion (3.6.29) can be derived from the following Hamiltonians (respectively expressed in the phase-space coordinate $\left(\phi, \frac{\Delta E}{\omega_0}\right)$ and (ϕ, δ) with time as the independent variable)

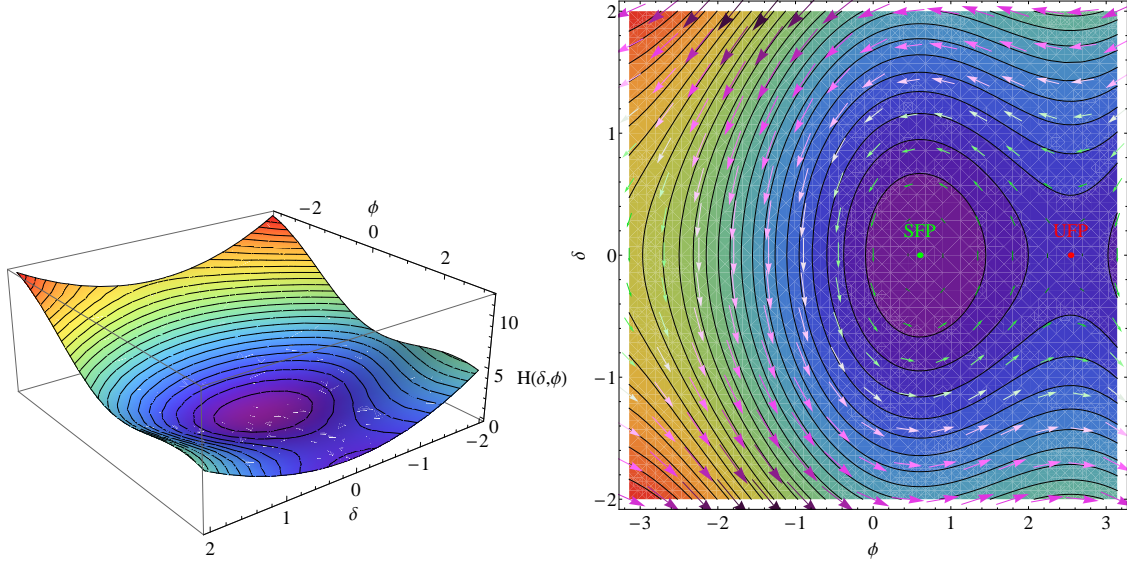
$$(3.7.1) \quad H = \frac{1}{2} \frac{h\omega_0^2\eta}{\beta^2 E} \left(\frac{\Delta E}{\omega_0} \right)^2 + \frac{eV}{2\pi} (\cos \phi - \cos \phi_s + (\phi - \phi_s) \sin \phi_s)$$

$$(3.7.2) \quad H = \frac{h\omega_0\eta_0}{2} \delta^2 + \frac{\omega_0 eV}{2\pi \beta^2 E} (\cos \phi - \cos \phi_s + (\phi - \phi_s) \sin \phi_s)$$

These Hamiltonians are time dependent during acceleration but if the acceleration rate is slow they can be considered to be quasi-static. The synchrotron motion corresponding to this quasi-static Hamiltonian is called adiabatic synchrotron motion. In this text we will only discuss adiabatic synchrotron motion. Figure 3.7.1 shows a surface plot for the Hamiltonian shown in equation (3.7.2). It also shows the particles trajectories in phase-space for different values of the Hamiltonian, the arrows are the phase-space velocities. These trajectories are the longitudinal equivalent of the phase-space ellipses that showed up in chapter 2 on transverse dynamics.

The Hamiltonian shows two fixed points ($\dot{\delta} = 0$ and $\dot{\phi} = 0$), namely the points $(\phi_s, 0)$ and $(\pi - \phi_s, 0)$. The first fixed point is the stable one (SFP). In the synchrotron phase-space particle close to the stable fixed point will describe more or less ellipses around this point, but the phase-space trajectories around the unstable fixed point (UFP) are hyperbola. This means the synchrotron phase-space is divided in stable and unstable regions showing a bunched beam (as we have explained in section 3.4 on phase stability). The phase-space trajectory that passes through the unstable fixed point is called the separatrix and is the separating curve between the stable and unstable region. The area in phase-space enclosed by this separatrix is called the bucket area and the maximum momentum deviation on the separatrix orbit is called the bucket height. The Hamiltonian of the separatrix goes through the unstable fixed point and therefore can be written as

$$(3.7.3) \quad H_{sep} = \frac{\omega_0 eV}{2\pi \beta^2 E} (-2 \cos \phi_s + (\pi - 2\phi_s) \sin \phi_s),$$

FIGURE 3.7.1. Surface and Contour Plot of $H(\delta, \phi)$

resulting in equation (3.7.4) for its trajectory in phase-space.

$$(3.7.4) \quad \delta_{sep}^2 + \frac{eV}{\pi\beta^2 E h \eta} (\cos \phi + \cos \phi_s - (\pi - \phi - \phi_s) \sin \phi_s) = 0.$$

The two turning points for this trajectory are $\pi - \phi_s$ and ϕ_t , with $\cos \phi_t + \phi_t \sin \phi_s = -\cos \phi_s + (\pi - \phi_s) \sin \phi_s$. The bucket area is defined as

$$(3.7.5) \quad \tilde{A}_B = \oint \delta_{sep}(\phi) d\phi.$$

For the separatrix this becomes

$$(3.7.6) \quad \tilde{A}_B = \frac{4}{\sqrt{2}} \sqrt{\frac{eV}{2\pi\beta^2 E h |\eta|}} \int_{\phi_t}^{\pi - \phi_s} \sqrt{-\frac{|\eta|}{\eta} (\cos \phi + \cos \phi_s - (\pi - \phi - \phi_s) \sin \phi_s)} d\phi$$

Important to note is that the bucket area vanishes for a synchronous phase of $\frac{\pi}{2}$. It is much more convenient and common to express the bucket area in the $(\phi, \frac{\Delta E}{\omega_0})$ phase-space coordinates

$$(3.7.7) \quad A_B = \frac{\beta^2 E}{\omega_0} \tilde{A}_B \approx h \Delta t \Delta E.$$

Equation (3.7.7) describes the bucket area around the entire ring thus the area of one bucket is $\Delta t \Delta E$, where Δt is the bucket length in seconds and ΔE is the buckets energy height in electron Volt. The bucket area is expressed in electron Volt Seconds (eVs). Let us take a closer look at this bucket.

The length of the bucket is

$$(3.7.8) \quad L_b = |(\pi - \phi_s - \phi_t)|$$

and the maximum height is

$$(3.7.9) \quad \delta_B = \sqrt{\frac{2eV}{\pi\beta^2 E h |\eta|} \left| \cos \phi_s - \frac{\pi - 2\phi_s}{2} \sin \phi_s \right|}.$$

To discuss the dynamics further we will consider small amplitude oscillations and large amplitude oscillations. We will start with small amplitude oscillations which means that the phase-angle is very close to

the synchronous phase-angle ($\phi \approx \phi_s$). Starting from Simpson's Formula

$$(3.7.10) \quad \sin \phi - \sin \phi_s = 2 \cos \left(\frac{\phi + \phi_s}{2} \right) \sin \left(\frac{\phi - \phi_s}{2} \right)$$

and using the small amplitude assumption to simplify formula (3.7.10) to

$$(3.7.11) \quad \sin \phi - \sin \phi_s = \cos \phi_s (\phi - \phi_s).$$

we can rewrite the equation of motion (3.6.29) for the phase angle as

$$(3.7.12) \quad \ddot{\phi} = \frac{d^2}{dt^2} (\phi - \phi_s) = \frac{h\omega_0^2 e V \eta_0 \cos \phi_s}{2\pi\beta^2 E} (\phi - \phi_s).$$

One immediately recognizes the harmonic oscillator. To have stable oscillations the term $\frac{h\omega_0^2 e V \eta_0 \cos \phi_s}{2\pi\beta^2 E}$ has to be less than zero. This leads to the stability condition

$$(3.7.13) \quad \eta_0 \cos \phi_s < 0,$$

since all the other parameters are positive. Below transition energy ($\eta_0 < 0$) the synchronous phase has to be $0 < \phi_s < \frac{\pi}{2}$ and above transition $\frac{\pi}{2} < \phi_s < \pi$ (as was explained in figure 3.4.1). Define the synchrotron angular frequency as in equation (3.7.14)

$$(3.7.14) \quad \Omega_s^2 = \frac{h\omega_0^2 e V |\eta_0 \cos \phi_s|}{2\pi\beta^2 E},$$

and the Synchrotron Tune as in equation (3.7.15).

$$(3.7.15) \quad Q_s = \frac{\omega_s}{\omega_0} = \sqrt{\frac{h e V |\eta_0 \cos \phi_s|}{2\pi\beta^2 E}}.$$

With these definitions the equations of motion around the stable fixed point for small oscillations can be rewritten as

$$(3.7.16) \quad \phi - \phi_s = \hat{\phi} \cos(\Omega_s t + \chi)$$

$$(3.7.17) \quad \delta = -\frac{Q_s}{h|\eta|} \hat{\phi} \sin(\Omega_s t + \chi)$$

$$(3.7.18) \quad \frac{\hat{\delta}}{\hat{\phi}} = \sqrt{\frac{e V |\cos \phi_s|}{2\pi\beta^2 E h |\eta|}} = \frac{Q_s}{h|\eta|}$$

with $\hat{\phi}$ and $\hat{\delta}$ the maximum amplitudes. In phase-space this is an ellipse with area $\pi \hat{\delta} \hat{\phi}$ so that we can write

$$(3.7.19) \quad \tilde{A} = \pi \hat{\delta} \hat{\phi} = h A \left(\frac{\omega_0}{\beta^2 E} \right)$$

for the bucket area. Particles in the bunches in the LHC are mainly distributed in a Gaussian way. A two dimensional Gaussian distribution can be written as

$$(3.7.20) \quad \rho(\delta, \phi) = \frac{1}{2\pi\sigma_\delta\sigma_\phi} \exp \left(-\frac{1}{2} \left(\frac{\phi^2}{\sigma_\phi^2} + \frac{\delta^2}{\sigma_\delta^2} \right) \right),$$

where σ_δ and $\sigma_\phi = \omega_{rf} \sigma_t$ are the RMS momentum spread and RMS bunch length (σ_t is the bunch length expressed in seconds and the subscript RF refers to the Radio Frequency of the Cavity). The corresponding RMS phase-space bucket area is $\tilde{A}_{RMS} = \pi\sigma_\delta\sigma_\phi$. The area containing 95% of the particles (2σ) is related to the RMS bucket area by $\tilde{A}_{95} = 6\tilde{A}_{RMS}$. Although it is correct that the factor six makes sure that 95% of the particles are in the phase-space bucket area, in practice one uses in many situations a factor four, this comes from the fact that the bucket area is multiplied by 4 if one goes from σ to 2σ for both sigmas. This area contains only about 86% of the particles instead of 95%. In this text we will use the factor 4 because

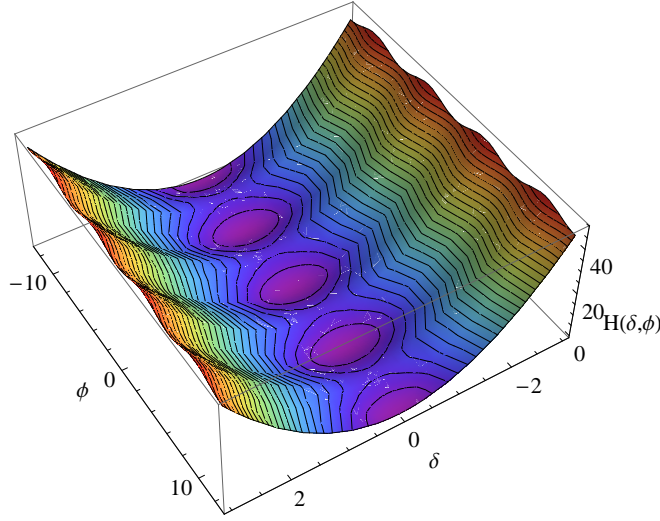


FIGURE 3.7.2. RF buckets

the simulation software and matching² is based on the area with the factor 4 and the longitudinal emittance in the LHC is defined as in equation

$$(3.7.21) \quad \epsilon_s = 4\pi\sigma_t\sigma_\delta E_0.$$

Combining the equations (3.7.19) and (3.7.18) we can rewrite the maximum momentum spread and maximum bunch length in function of the bucket area.

$$(3.7.22) \quad \hat{\delta} = A^{1/2} \left(\frac{\omega_0}{\pi\beta^2 E} \right)^{1/2} \left(\frac{heV |\cos \phi_s|}{2\pi\beta^2 E |\eta|} \right)^{1/4}$$

$$(3.7.23) \quad \hat{\phi} = h A^{1/2} \left(\frac{\omega_0}{\pi\beta^2 E} \right)^{1/2} \left(\frac{heV |\cos \phi_s|}{2\pi\beta^2 E |\eta|} \right)^{-1/4}$$

Consider now large amplitude oscillations. We still consider the Hamiltonian to be quasi-static.

$$(3.7.24) \quad H(\phi, \delta) = H_0.$$

H_0 can be calculated from equation (3.7.2)

$$(3.7.25) \quad H_0 = \frac{1}{2} h \omega_0 \eta \hat{\delta}^2 = \frac{\omega_0 eV}{2\pi\beta^2 E} \left(\cos \hat{\phi} - \cos \phi_s + (\hat{\phi} - \phi_s) \sin \phi_s \right)$$

Figure 3.7.2 shows the surface plot for this Hamiltonian for different RF buckets where we stitched the Hamiltonians of the different buckets together to form a continuous surface. The Hamiltonian H_0 is linear in $\hat{\phi}$ so that if the value of H_0 is high enough a particle can jump to another bucket or get lost. By use of equation (3.6.29) the synchrotron period for large amplitude particles can be calculated as

$$(3.7.26) \quad T = \oint \left(2h\omega_0\eta \left(H_0 - \frac{\omega_0 eV}{2\pi\beta^2 E} (\cos \phi - \cos \phi_s + (\phi - \phi_s) \sin \phi_s) \right) \right)^{-1/2} d\phi$$

²In creating the particle distributions for the simulations their longitudinal distribution needs to match the bucket area, otherwise the simulation will lose to many particles in the first part of the simulations. This matching also needs to be done in reality when the bunches are injected in the LHC from the SPS. If these bunches are mismatched at injection some of the particles will be outside of the separatrix area and thus have unstable trajectories in phase-space creating losses that can result in beam dumps which is sometimes the case. Beam dumps can be triggered automatically by the machine protection system if the losses are creating damage to the machine or by the operator if he/she decides that the quality of the beam is too low. Since this mismatching can lead to large initial losses large efforts are put into injection studies.

and the angular frequency then becomes

$$(3.7.27) \quad \omega = \frac{2\pi}{T}.$$

3.8. Synchrotron symplectic mapping equations

In chapter 2 we used a matrix formalism to calculate the changes in the phase-space coordinates along the ring. Unfortunately for the longitudinal phase-space coordinates this is not possible. To track the longitudinal changes we need the more general concept of a map [16, 12]. Without going further into detail we here state a possible set of mapping equations for the longitudinal phase-space coordinates where the RF cavities are considered as localized and very short.

$$(3.8.1) \quad \delta_{n+1} = \delta_n + \frac{eV}{\beta^2 E} (\sin \phi_n - \sin \phi_s)$$

$$(3.8.2) \quad \phi_{n+1} = \phi_n + 2\pi h \eta (\delta_{n+1}) \delta_{n+1}$$

An important property of these mapping equations is that they satisfy the symplectic condition and thus preserve the Hamiltonian Invariant. Although the concept of maps is beyond the scope of this text we state these mapping equations here because they are implemented in the particle tracking code to simulate the synchrotron motion in the LHC.

$$(3.8.3) \quad \text{Jacobian} = \frac{\partial (\delta_{n+1}, \phi_{n+1})}{\partial (\delta_n, \phi_n)} = 1$$

3.9. Summary

In this chapter I gave a short introduction to longitudinal dynamics in an accelerator. After some basic relativistic dynamics equations I shortly described an RF cavity and introduced the Transit Time (equations (3.3.5)) and the Principle of Phase Stability. Parameters as the Momentum Compaction Factor (equation (3.5.2)), the Phase-slip Factor (equation (3.5.14)) and the Transition Energy (equation (3.5.17)) were introduced before deriving the longitudinal equations of motion (equations (3.6.29)). The longitudinal equations of motion can be derived from the Hamiltonians shown in expressions (3.7.2) and (3.7.1) depending on the choice of longitudinal phase-space coordinates. The behavior of particles with these Hamiltonians, considering them to be quasi-static, was discussed. This discussion lead to the concept of an RF bucket and its area in phase-space which is related to the longitudinal emittance (equation (3.7.21)). This chapter was concluded by defining synchrotron symplectic mapping equations used in the particle tracking software to update the longitudinal phase-space coordinates of the particles in the simulations.

Part 2

Intrabeam scattering models

CHAPTER 4

The Bjorken-Mtingwa Model

A large number of charged particles confined in a small space, such as can be found in a bunch in the LHC beam, will Coulomb scatter off each other. This scattering is referred to as *Intrabeam scattering*. This effect occurs next to a space-charge effect, caused by the repulsion between particles due to the Coulomb Field they generate, but the treatment of space-charge effects is beyond the scope of this text and becomes less relevant at higher energies as can be seen for example from expression 4.0.1 for the space-charge force on a parallel co-moving particle in a cylindrical beam with diameter a .

$$(4.0.1) \quad \vec{F} = \begin{cases} \frac{e^2 N}{2\pi\epsilon_0 a^2 \gamma^2} \vec{r} & r \leq a \\ \frac{e^2 N}{2\pi\epsilon_0 r^2 \gamma^2} \vec{r} & r > a \end{cases}$$

Intrabeam scattering (IBS) affects the overall beam parameters such as the emittance and bunch length, it has a large impact on beam operation and lifetime. In their article [14] Bjorken and Mtingwa (BM) calculate the change of such parameters by deriving a rate equation for a “random” function f starting from the Leading Order terms in perturbation theory for Quantum Electro-Dynamics. Their calculations are not completely general, since they assume the particles are distinguishable, hence treating them as classical particles. In the sections below I tried to go through BM’s entire calculations, basically rewriting their article but completing it with most of the calculations they did not write out in the publication. There are some assumptions and notations in BM’s calculations that are not always clear and I tried to clarify them where necessary.

4.1. The particle distribution and used notations

As is often done in accelerator physics, a Gaussian distribution in phase-space is assumed, motivated by the fact that one can usually solve the equations analytically for Gaussian distributions and that this often leads to good first estimates for the parameters under investigation. So let us assume for the distribution of particles (in canonical phase-space coordinates)

$$(4.1.1) \quad \rho(x, p) = \frac{N}{\Gamma} \exp[-S(x, p)],$$

where

$$(4.1.2) \quad \Gamma = \int d^3x d^3p \exp[-S(x, p)],$$

is a normalization constant and S is related to the action (see equation (2.6.9)) so that we have a Multivariate Gaussian Distribution [13] (elliptic form in phase-space), its most general form is shown in equation (4.1.3)

$$(4.1.3) \quad S(x, p) = \frac{1}{2} A_{ij} \delta p_i \delta p_j + B_{ij} \delta p_i \delta x_j + \frac{1}{2} C_{ij} \delta x_i \delta x_j.$$

S can be divided in the contributions from the different planes

$$(4.1.4) \quad S(\mathbf{x}, \mathbf{p}) = S^{(h)} + S^{(v)} + S^{(l)} = S^{(x)} + S^{(y)} + S^{(s)},$$

where (notice the similarity now with expression (2.6.12) for the action)

$$(4.1.5) \quad S^{(x)} = \frac{\beta_x}{2\epsilon_x} x_\beta'^2 - \frac{\beta_x'}{2\epsilon_x} x_\beta x_\beta' + \frac{1}{2\epsilon_x \beta_x} \left(1 + \frac{\beta_x'^2}{4} \right) x_\beta^2,$$

$$(4.1.6) \quad S^{(y)} = \frac{\beta_y}{2\epsilon_y} y_\beta'^2 - \frac{\beta_y'}{2\epsilon_y} y_\beta y_\beta' + \frac{1}{2\epsilon_y \beta_y} y_\beta^2,$$

$$(4.1.7) \quad S^{(s)} = \begin{cases} \frac{\delta^2}{2\sigma_D^2} & \text{for unbunched beams} \\ \frac{\delta^2}{\sigma_D^2} + \frac{(s-\bar{s})^2}{2\sigma_s^2} & \text{for bunched beams} \end{cases}$$

with σ_x, σ_y and σ_s respectively the RMS beam widths in the two transverse planes and the bunch length in a bunched beam. σ_D is the width of the horizontal Dispersion. It is important to keep in mind the definition used for emittance, because this is not always clear. Here the ϵ_i are the RMS emittances as defined for distributions in section 2.7

$$(4.1.8) \quad \epsilon_x = \frac{\sigma_x^2}{\beta_x},$$

$$(4.1.9) \quad \epsilon_y = \frac{\sigma_y^2}{\beta_y},$$

$$(4.1.10) \quad \sigma_D = \frac{\sigma_p}{\bar{p}},$$

$$(4.1.11) \quad x_\beta = x - D(s) \delta,$$

$$(4.1.12) \quad x_\beta' = x' - D'(s) \delta,$$

with σ_p the momentum spread, D the horizontal Dispersion Function, \bar{p} the reference momentum and

$$(4.1.13) \quad x' \equiv \frac{\delta p_x}{\bar{p}},$$

$$(4.1.14) \quad y' \equiv \frac{\delta p_y}{\bar{p}},$$

$$(4.1.15) \quad \delta \equiv \frac{\delta p_s}{\bar{p}}.$$

4.2. Transition Rate for Two-Body Scattering

To be able to quantize the effect of IBS on the beam size we need to take a little detour to Quantum Field Theory (QFT). The goal of this section is to get to the transition rate shown in equation (4.2.1) for the scattering process $p_1 + p_2 \rightarrow p_1' + p_2'$:

$$(4.2.1) \quad \frac{dN}{dt} = \frac{1}{2} \int d^3x \frac{d^3p_1}{\gamma_1} \frac{d^3p_2}{\gamma_2} \rho(x, p_1) \rho(x, p_2) |\mathcal{M}|^2 \frac{d^3p_1'}{\gamma_1'} \frac{d^3p_2'}{\gamma_2'} \frac{\delta^{(4)}(p_1' + p_2' - p_1 - p_2)}{(2\pi)^2},$$

with

$$(4.2.2) \quad \mathcal{M} = \frac{4\pi\alpha}{q^2},$$

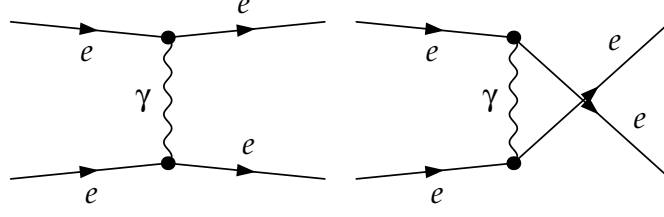


FIGURE 4.2.1. Feynman Diagrams

$$(4.2.3) \quad q_\mu = (p'_1 - p_1)_\mu,$$

and

$$(4.2.4) \quad q^2 \equiv -Q^2 < 0.$$

we start this calculation from the S-matrix element for Rutherford scattering of an electron in a coulomb field, following the approach¹ taken by Bjorken and Drell in [3]. Identifying this coulomb field with the one emanating from a proton enables me to calculate the scattering of electrons in the coulomb field of a proton at low energies so that the composite structure of the proton can be neglected. The argumentation here is that in a beam of particles the particles momenta in the frame of the beam are small compared to the momenta needed to detect the internal structure of the proton. As a last step we will then assume that the calculated event rate is also valid for low energy elastic proton-proton scattering (replacing of course charge and mass of the electron by that of a proton, i.e. replacing the electron current by a proton current).

The S-matrix element is given by equation (4.2.5).

$$(4.2.5) \quad S_{fi} = -ie \int d^4x \bar{\psi}_f(x) \not{A}(x) \psi_i(x)$$

The Coulomb potential of the proton can be written as [3, 10, 17]

$$(4.2.6) \quad \square A^\mu(x) = J^\mu(x),$$

assuming the Lorentz gauge $\partial_\mu A^\mu(x) = 0$ and where $J^\mu(x)$ is the proton current. An expression for the Coulomb Field obeying this equation can be found using Green's Functions

$$(4.2.7) \quad D_F(x-y) = \int \frac{d^4q}{(2\pi)^4} \exp[-iq(x-y)] D_F(q^2),$$

with q the momentum transfer between the colliding particles and

$$(4.2.8) \quad D_F(q^2) = -\frac{1}{q^2 + i\epsilon}$$

$$(4.2.9) \quad \square D_F(x-y) = \delta^4(x-y).$$

The proton Coulomb Field can then be written as

$$(4.2.10) \quad A^\mu(x) = \int d^4y D_F(x-y) J^\mu(y).$$

¹Of course the formula could also be attained by immediately writing down the proton currents.

Putting expression (4.2.10) back in the S-matrix element (4.2.5) results in

$$(4.2.11) \quad S_{fi} = -i \int d^4x d^4y [e \bar{\psi}_f(x) \gamma_\mu \psi_i(x)] D_F(x-y) J^\mu(y).$$

Considering the form of the electron current, propose a proton current of the form

$$(4.2.12) \quad J^\mu(y) = -\sqrt{\frac{M^2}{E_f E_i}} \frac{e_p}{V} \exp[i(p_f - p_i)y] \bar{u}(p_f, s_f) \gamma^\mu u(p_i, s_i),$$

with e_p the proton charge and M the proton's mass. With this choice for the proton current (and using $\bar{\psi}_f = \sqrt{\frac{m}{E_f V}} \bar{u}(p_f, s_f) \exp[ip_f x]$ for the electron) the S-matrix element becomes

$$(4.2.13) \quad S_{fi} = -\frac{ie^2}{V^2} (2\pi)^4 \delta^4(p'_2 - p_2 + p'_1 - p_1) \sqrt{\frac{m^2}{E'_1 E_1}} \sqrt{\frac{M^2}{E'_2 E_2}} [\bar{u}(p'_1, s'_1) \gamma_\mu u(p_1, s_1)] \frac{1}{(p'_1 - p_1)^2 + i\epsilon} [\bar{u}(p'_2, s'_2) \gamma^\mu u(p_2, s_2)],$$

where the p_i , $i = 1, 2$, refer to the momenta (the prime is for the final states and 1,2 respectively refer to the electron and proton), m is the mass of the electron and M the mass of the proton. The u 's refer to the Dirac spinors and the s_i , $i = 1, 2$, refer to the spin states of the spinors.

This formula is symmetric for the electron and the proton, so if we would have started from the scattering of a proton in the field of an electron this would have resulted in the same formula. As long as the momentum transfer between the proton and electron is small enough we can consider the proton as a point like particle. The elementary transition rate per unit volume can now be written as **[3, 10, 17]**

$$(4.2.14) \quad \begin{aligned} w_{fi} &= \frac{|S_{fi}|^2}{VT} \\ &= (2\pi)^4 \delta^4(p'_1 + p'_2 - p_1 - p_2) \frac{1}{V^4} \frac{m^2}{E'_1 E_1} \frac{M^2}{E'_2 E_2} |\mathcal{M}_{fi}|^2, \end{aligned}$$

with

$$(4.2.15) \quad |\mathcal{M}_{fi}|^2 = [\bar{u}(p'_1, s'_1) \gamma_\mu u(p_1, s_1)] \frac{e^2}{q^2 + i\epsilon} [\bar{u}(p'_2, s'_2) \gamma^\mu u(p_2, s_2)],$$

and where I used the trick

$$(4.2.16) \quad \begin{aligned} \left[(2\pi)^4 \delta^4(p'_1 + p'_2 - p_1 - p_2) \right]^2 &= (2\pi)^4 \delta^4(0) (2\pi)^4 \delta^4(p'_1 + p'_2 - p_1 - p_2) \\ &= (2\pi)^4 \left[\frac{1}{(2\pi)^4} \int \exp[-ipx] d^4x \right]_{p=0} (2\pi)^4 \delta^4(p'_1 + p'_2 - p_1 - p_2) \\ &= \int 1. d^4x (2\pi)^4 \delta^4(p'_1 + p'_2 - p_1 - p_2) \\ &= VT (2\pi)^4 \delta^4(p'_1 + p'_2 - p_1 - p_2). \end{aligned}$$

to calculate the squares of the Delta Functions. The total event rate $\frac{dN}{dt}$ is then equal to the integral over the number of final states times the particle density times the number of target particles divided by the volume. Noting that the number of states in the interval $d^3p'_1 d^3p'_2$ is just $V \frac{d^3p'_1}{(2\pi)^3} V \frac{d^3p'_2}{(2\pi)^3}$ this results in expression (4.2.17) for the total event rate.

$$(4.2.17) \quad \begin{aligned} \frac{dN}{dt} &= \int d^3x \rho_1(x, t) \rho_2(x, t) \int \frac{mM}{E_1 E_2} |\mathcal{M}_{fi}|^2 (2\pi)^4 \delta^4(p'_1 + p'_2 - p_1 - p_2) \frac{m d^3p'_1}{(2\pi)^3 E'_1} \frac{M d^3p'_2}{(2\pi)^3 E'_2} \\ &= \int d^3x \frac{d^3p_1}{\gamma_1} \frac{d^3p_2}{\gamma_2} \rho_1(x, p_1) \rho_2(x, p_2) |\mathcal{M}_{fi}|^2 (2\pi)^4 \delta^4(p'_1 + p'_2 - p_1 - p_2) \frac{m d^3p'_1}{(2\pi)^3 E'_1} \frac{M d^3p'_2}{(2\pi)^3 E'_2} \end{aligned}$$

²With the normalization $\bar{\psi}_f = \sqrt{\frac{m}{E_f V}} \bar{u}(p_f, s_f) \exp[ip_f x]$, the number of target particles per unit volume is just $\frac{1}{V}$.

In this last equation $E = \gamma m$ was used and a Fourier transformation was made to convert the time coordinate into the momentum coordinate, absorbing the extra terms in the particle density distributions ρ_i , $i = 1, 2$. Since we are treating non polarized beams here we need to average over the initial spin states and sum over the final spin states. The matrix element can now be simplified to equation (4.2.18).

$$\begin{aligned}
|\mathcal{M}_{fi}|^2 &= \frac{1}{4} \sum_{s_{f1}, s_{f2}, s_{i1}, s_{i2}} \left| [\bar{u}(p'_1, s'_1) \gamma^\mu u(p_1, s_1)] \frac{e^2}{q^2 + i\epsilon} [\bar{u}(p'_2, s'_2) \gamma_\mu u(p_2, s_2)] \right|^2 \\
&= \frac{1}{4} \sum_{s_{f1}, s_{f2}, s_{i1}, s_{i2}} \left([\bar{u}(p'_1, s'_1) \gamma^\mu u(p_1, s_1)] \frac{e^2}{q^2 + i\epsilon} [\bar{u}(p'_2, s'_2) \gamma_\mu u(p_2, s_2)] \right)^\dagger \\
&\quad \left([\bar{u}(p'_1, s'_1) \gamma^\nu u(p_1, s_1)] \frac{e^2}{q^2 + i\epsilon} [\bar{u}(p'_2, s'_2) \gamma_\nu u(p_2, s_2)] \right) \\
&= \frac{1}{4} \sum_{s_{f1}, s_{f2}, s_{i1}, s_{i2}} \left([(\bar{u}(p'_1, s'_1))_a (\gamma^\mu)_{ab} (u(p_1, s_1))_b] \frac{e^2}{q^2 + i\epsilon} [(\bar{u}(p'_2, s'_2))_c (\gamma_\mu)_{cd} (u(p_2, s_2))_d] \right)^\dagger \\
&\quad \left([(\bar{u}(p'_1, s'_1))_a (\gamma^\nu)_{ab} (u(p_1, s_1))_b] \frac{e^2}{q^2 + i\epsilon} [(\bar{u}(p'_2, s'_2))_c (\gamma_\nu)_{cd} (u(p_2, s_2))_d] \right) \\
&= \frac{1}{4} \frac{e^4}{q^4} \text{Tr} \left[\frac{\not{p}'_1 + m}{2m} \gamma^\mu \frac{\not{p}_1 + m}{2m} \gamma^\nu \right] \text{Tr} \left[\frac{\not{p}'_2 + M}{2M} \gamma_\mu \frac{\not{p}_2 + M}{2M} \gamma_\nu \right] \\
&= \frac{e^4}{64q^4 m^2 M^2} \text{Tr} [\not{p}'_1 \gamma^\mu \not{p}_1 \gamma^\nu + m^2 \gamma^\mu \gamma^\nu] \text{Tr} [\not{p}'_2 \gamma_\mu \not{p}_2 \gamma_\nu + M^2 \gamma_\mu \gamma_\nu] \\
&= \frac{e^4}{4q^4 m^2 M^2} [p'_1{}^\mu p_1{}^\nu + p'_1{}^\nu p_1{}^\mu - g^{\mu\nu} (p'_1 p_1 - m^2)] [p'_2{}_\mu p_{2\nu} + p'_{2\nu} p_{2\mu} - g_{\mu\nu} (p'_2 p_2 - M^2)] \\
(4.2.18) \quad &= \frac{e^4}{2q^4 m^2 M^2} [(p'_1 p'_2) (p_1 p_2) + (p'_1 p_2) (p_1 p'_2) - m^2 (p'_1 p_1) - M^2 (p'_2 p_2) + 2m^2 M^2],
\end{aligned}$$

where the Latin indices a, b, c, d refer to the elements in the vectors and matrices. After working out the dagger operation this leads to the traces. By use of the property of Dirac spinors (see [17, 10, 3]) that is shown in equation (4.2.19)

$$(4.2.19) \quad \sum_s u_\alpha(p, s) \bar{u}_\beta(p, s) = (\not{p} + m)_{\alpha\beta}$$

the equations can be simplified further. Now assuming that the scattering particles are of the same kind, that small angle scattering is dominant and that the scattering is elastic (hence $E'_1 = E'_2 = E_1 = E_2$) we end up with expression (4.2.20) for the matrix element in the center of mass system (CMS)

$$(4.2.20) \quad |\mathcal{M}_{fi}|^2 = \frac{e^4}{q^4} = \frac{(4\pi\alpha)^2}{q^4},$$

with α the electromagnetic coupling constant. Assuming that we can distinguish the particles ³, we need to add a factor $\frac{1}{2}$. This comes from the fact that when we consider the particles to be distinguishable we count the possible Feynman diagrams (see Figure 4.2.1) twice by doing the sum over the final state spins. As such, instead of considering $|\mathcal{M}_a + \mathcal{M}_b|^2$, $2|\mathcal{M}_a|^2$ was used. The mixing term is neglected because we are only considering Leading Order contributions, the total event rate (equation (4.2.17)) can then be expressed as shown in equation (4.2.21)

$$(4.2.21) \quad \frac{dN}{dt} = \frac{1}{2} \int d^3x \frac{d^3p_1}{\gamma_1} \frac{d^3p_2}{\gamma_2} \rho_1(x, p_1) \rho_2(x, p_2) |\mathcal{M}_{fi}|^2 (2\pi)^4 \delta^4(p'_1 + p'_2 - p_1 - p_2) \frac{d^3p'_1}{(2\pi)^3 E'_1} \frac{d^3p'_2}{(2\pi)^3 E'_2}.$$

³Particles are considered as classical particles in a bunch by BM. A treatment considering the particles with Fermi or Bose-Einstein statistics can be found in reference [19]. The conclusion in this reference is that the quantum corrections due to Fermi or Bose-Einstein statistics can be neglected for current accelerators.

4.3. Rate equations

Since we are interested in changes of functions of momentum deviations, $f(\bar{p} + \delta p)$, a rate of change equation is needed. In general we can write this immediately from the transition rate equations from previous section:

$$(4.3.1) \quad \frac{d\langle f(p) \rangle}{dt} = \frac{N}{2\Gamma^2} \int d^3x \frac{d^3p_1}{\gamma_1} \frac{d^3p_2}{\gamma_2} \exp(-S(x, p_1) - S(x, p_2)) |\mathcal{M}|^2 \\ (f(p'_1) - f(p_1) + f(p'_2) - f(p_2)) \frac{d^3p'_1}{\gamma'_1} \frac{d^3p'_2}{\gamma'_2} \frac{\delta^{(4)}(p'_1 + p'_2 - p_1 - p_2)}{(2\pi)^2}.$$

Note that the expectation values obey

$$(4.3.2) \quad \langle f(p'_1) - f(p_1) \rangle = \langle f(p'_2) - f(p_2) \rangle,$$

which leads to

$$(4.3.3) \quad \frac{d\langle f(p) \rangle}{dt} = \frac{N}{\Gamma^2} \int d^3x \frac{d^3p_1}{\gamma_1} \frac{d^3p_2}{\gamma_2} \exp(-S(x, p_1) - S(x, p_2)) |\mathcal{M}|^2 (f(p'_1) - f(p_1)) \\ \frac{d^3p'_1}{\gamma'_1} \frac{d^3p'_2}{\gamma'_2} \frac{\delta^{(4)}(p'_1 + p'_2 - p_1 - p_2)}{(2\pi)^2}.$$

Let us take a look at small momentum deviations from the reference momentum \bar{p} . In the scattering process earlier we had that

$$(4.3.4) \quad p'_1 = p_1 + q.$$

Applying a Taylor expansion to the function f around p_1 results in

$$(4.3.5) \quad f(p'_1) - f(p_1) = q_i \left. \frac{\partial f}{\partial p_i} \right|_{p=p_1} + \frac{q_i q_j}{2} \left. \frac{\partial^2 f}{\partial p_i \partial p_j} \right|_{p=p_1} + \dots$$

Introducing the parameters $\xi = p_1 + p_2 - 2\bar{p}$ (the sum of the momentum deviations with respect to the reference particle) and $\Delta = \frac{1}{2}(p_1 - p_2)$ the initial momenta of the colliding particles can be expressed as

$$(4.3.6) \quad p_1 = \bar{p} + \frac{\xi}{2} + \Delta = \bar{p} + \delta_1,$$

$$(4.3.7) \quad p_2 = \bar{p} + \frac{\xi}{2} - \Delta = \bar{p} + \delta_2.$$

The Taylor expansion to second order for f then becomes

$$(4.3.8) \quad f(p'_1) - f(p_1) = q_i \left(\frac{\xi_j}{2} + \Delta_j + \frac{q_j}{2} \right) \left. \frac{\partial^2 f}{\partial p_i \partial p_j} \right|_{\bar{p}},$$

where we used the expressions $q_i = p'_{1,i} - p_{1,i}$, $i = x, y, s$ for the components of the momentum transfer between the two particles and

$$(4.3.9) \quad \left. \frac{\partial f}{\partial p_i} \right|_{p=p_1} = \left. \frac{\partial f}{\partial p_i} \right|_{p=\bar{p}} + (p_1 - \bar{p})_i \left. \frac{\partial^2 f}{\partial p_i \partial p_j} \right|_{p=\bar{p}} + \dots,$$

$$(4.3.10) \quad p_1 - \bar{p} = \frac{\xi}{2} + \Delta,$$

$$(4.3.11) \quad \left. \frac{\partial f}{\partial p_i} \right|_{p=\bar{p}} = 0.$$

Expressing the exponent of the exponential under the integral in equation (4.1.3) in the new parameters ξ and Δ results in expression (4.3.12).

$$\begin{aligned}
S(\mathbf{x}, \delta_1) + S(\mathbf{x}, \delta_2) &= \frac{1}{2} A_{ij} \left(\frac{\xi_i}{2} + \Delta_i \right) \left(\frac{\xi_j}{2} + \Delta_j \right) + B_{ij} x_i \left(\frac{\xi_j}{2} + \Delta_j \right) + \frac{1}{2} C_{ij} x_i x_j \\
&\quad + \frac{1}{2} A_{ij} \left(\frac{\xi_i}{2} - \Delta_i \right) \left(\frac{\xi_j}{2} - \Delta_j \right) + B_{ij} x_i \left(\frac{\xi_j}{2} - \Delta_j \right) + \frac{1}{2} C_{ij} x_i x_j \\
&= \frac{1}{2} A_{ij} \frac{\xi_i \xi_j}{2} + B_{ij} x_i \xi_j + C_{ij} x_i x_j + A_{ij} \Delta_i \Delta_j \\
(4.3.12) \quad &= S \left(\sqrt{2} \mathbf{x}, \frac{\boldsymbol{\xi}}{\sqrt{2}} \right) + \tilde{S}(\boldsymbol{\Delta}),
\end{aligned}$$

with

$$(4.3.13) \quad \tilde{S}(\boldsymbol{\Delta}) = A_{ij} \Delta_i \Delta_j.$$

Using equations (4.3.12) and (4.3.13) the rate equation can be rewritten as

$$(4.3.14) \quad \frac{d \langle f(p) \rangle}{dt} = \frac{4\alpha^2 N}{\gamma^2 \Gamma^2} \int d^3 x d^3 \xi d^3 \Delta \exp \left(-S \left(\sqrt{2} \mathbf{x}, \frac{\boldsymbol{\xi}}{\sqrt{2}} \right) - \tilde{S}(\boldsymbol{\Delta}) \right).$$

$$(4.3.15) \quad \int \frac{d^3 p'_1}{\gamma'_1} \frac{d^3 p'_2}{\gamma'_2} \frac{q_i \left(\frac{\xi_i}{2} + \Delta_j + \frac{q_j}{2} \right)}{(q^2)^2} \frac{\partial^2 f}{\partial p_i \partial p_j} \bigg|_{\bar{p}} \delta^{(4)}(p'_1 + p'_2 - W),$$

where

$$(4.3.16) \quad W_\mu = (p_1 + p_2)_\mu,$$

$$(4.3.17) \quad \Delta_\mu = \frac{1}{2} (p_1 - p_2)_\mu$$

(the momenta here are considered as 4-vectors). These new symbols have the properties:

$$(4.3.18) \quad \Delta \cdot W = p_1^2 - p_2^2 = m^2 - m^2 = 0 \quad (\text{assuming scattering of identical particles}),$$

$$(4.3.19) \quad \Delta^2 = -|\boldsymbol{\Delta}|^2 < 0,$$

$$(4.3.20) \quad W^2 + 4\Delta^2 = 2p_1^2 + 2p_2^2 = 4m^2.$$

Integrating over x and ξ leads to

$$(4.3.21) \quad \frac{d \langle f(p) \rangle}{dt} = \frac{4\alpha^2 N}{\gamma^2 \tilde{\Gamma}} \int d^3 \Delta \exp \left(-\tilde{S}(\boldsymbol{\Delta}) \right) \frac{\partial^2 f}{\partial p_i \partial p_j} \left(I_i \Delta_j + \frac{I_{ij}}{2} \right),$$

where

$$\begin{aligned}
I_\mu &= \int \frac{d^3 p'_1}{\gamma'_1} \frac{d^3 p'_2}{\gamma'_2} \frac{q_\mu}{q^4} \delta^{(4)}(p'_1 + p'_2 - p_1 - p_2), \\
I_{\mu\nu} &= \int \frac{d^3 p'_1}{\gamma'_1} \frac{d^3 p'_2}{\gamma'_2} \frac{q_\mu q_\nu}{q^4} \delta^{(4)}(p'_1 + p'_2 - p_1 - p_2), \\
\tilde{\Gamma} &= \begin{cases} \Gamma & \text{for bunched beams} \\ \frac{\Gamma}{\sqrt{2}} & \text{for unbunched beams} \end{cases}.
\end{aligned}$$

Although Bjorken and Mtingwa claim that the integration over x and ξ is straightforward I disagree. Therefore I will expand the integral into its constituents and do some of the calculations explicitly to show how the transition from equation (4.3.15) to equation (4.3.21) is done. Let me start by looking at the contribution of

$$\int d^3 x d^3 \xi \exp \left(-S \left(\sqrt{2} \mathbf{x}, \frac{\boldsymbol{\xi}}{\sqrt{2}} \right) \right) \cdot \left(\frac{\xi_x + \xi_y + \xi_s}{2} \right),$$

where all the other integrals are independent of the variables x and ξ thus can be combined in a constant factor. The main goal here is to show that this contribution disappears. To do the actual calculation I split

this integral up into its components in the different planes (Frenet-Serret coordinates in the beam frame, thus with respect to the reference particle):

$$\begin{aligned}
IX &= \int dx d\xi_x \exp \left(-S \left(\sqrt{2}\mathbf{x}, \frac{\boldsymbol{\xi}}{\sqrt{2}} \right) \right)_{x, \xi_x} \cdot \left(\frac{\xi_x}{2} \right) \\
&= \int dx d\xi_x \exp \left(\frac{1}{2} A_{xx} \frac{\xi_x \xi_x}{2} + B_{xx} x \xi_x + \frac{1}{2} C_{xx} x^2 \right) \cdot \left(\frac{\xi_x}{2} \right) \\
&= \frac{1}{2} \int dx \exp \left[\frac{1}{2} C_{xx} x^2 \right] \int d\xi_x \xi_x \exp \left[\frac{1}{2} A_{xx} \frac{\xi_x \xi_x}{2} + B_{xx} x \xi_x \right] \\
&= \frac{1}{2} \int dx \exp \left[\frac{1}{2} C_{xx} x^2 \right] \int d\xi_x \xi_x \exp \left[\left(\frac{\sqrt{A_{xx}} \xi_x}{2} + \frac{\sqrt{B_{xx}} x}{\sqrt{C_{xx}}} \right)^2 - \frac{B_{xx} x^2}{A_{xx}} \right] \\
&= \frac{1}{2} \int dx \exp \left[\frac{1}{2} C_{xx} x^2 - \frac{B_{xx} x^2}{A_{xx}} \right] \int d\xi_x \xi_x \exp \left[\left(\frac{\sqrt{A_{xx}} \xi_x}{2} + \frac{\sqrt{B_{xx}} x}{\sqrt{C_{xx}}} \right)^2 \right].
\end{aligned}$$

The second integral in the last equality is now the integral between symmetric boundaries of an odd function, although shifted over $\frac{\sqrt{B_{xx}} x}{\sqrt{C_{xx}}}$. But since the integration boundaries are $(-\infty, \infty)$ we can ignore this and thus the integral vanishes as claimed by Bjorken and Mtingwa⁴. Similar integrations are valid in the y and s plane. The factor for unbunched beams comes from the fact that the distribution along the s direction is homogeneous and that the δ is replaced by $\frac{\xi}{\sqrt{2}}$ in the exponential (see equations (4.1.7)), doubling the sigma for the Gaussian. Together with the definition of Γ , this leads to the factor $\frac{1}{\sqrt{2}}$.

Let us now assume to be in the center of mass reference frame in which $\boldsymbol{\Delta} = (0, 0, |\boldsymbol{\Delta}|)$, and since we are only considering elastic scattering of identical particles ($E'_1 = E_1 = E'_2 = E_2$) [15] this gives for the temporal part of the integrals

$$I_0 = I_{00} = I_{0i} = 0,$$

so we can write

$$I_\mu = \Delta_\mu I(\Delta^2)$$

and

$$(4.3.22) \quad I_{\mu\nu} = \left(-g_{\mu\nu} + \frac{W_\mu W_\nu}{W^2} - \frac{\lambda(\Delta^2) \Delta_\mu \Delta_\nu}{|\Delta^2|} \right) \tilde{I}(\Delta^2)$$

$$(4.3.23) \quad g_{\mu\nu} = \begin{pmatrix} 1 & 0 & 0 & 0 \\ 0 & -1 & 0 & 0 \\ 0 & 0 & -1 & 0 \\ 0 & 0 & 0 & -1 \end{pmatrix},$$

where now only I, λ and \tilde{I} need to be determined. The only term for I_μ that remains in the CMS is I_3 . To calculate I_3 we first need to use some trigonometry.

⁴The matrices A, B and C are diagonal matrices, as can be seen immediately from equations 4.1.5, 4.1.6 and 4.1.7. This is not true in the case of coupling between the planes: in this case there will be an additional linear term so that just the translation distance is changed, but the final integral will still evaluate to zero.

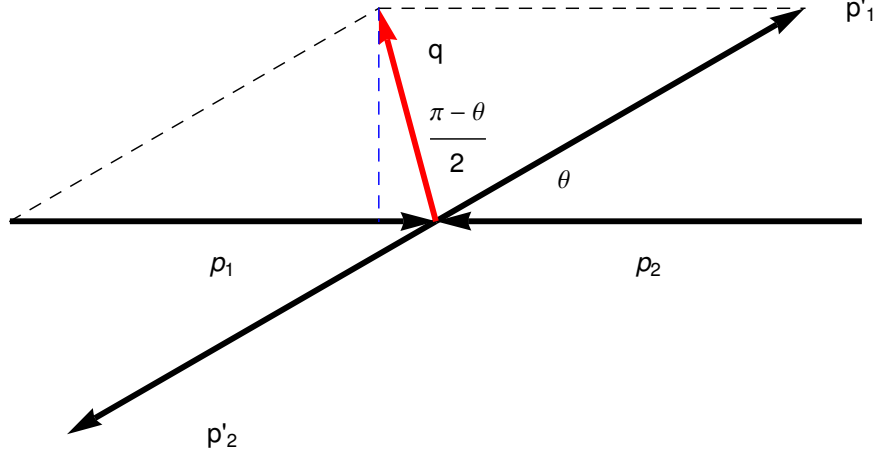


FIGURE 4.3.1. Collision in the center of mass system

Figure 4.3.1 shows the collision in the center of mass system where

$$(4.3.24) \quad |\mathbf{\Delta}|_{CMS} = \frac{1}{2} |\mathbf{p}_1 - \mathbf{p}_2| = \frac{2p}{2} = p = \Delta_3,$$

with p the magnitude of the 3-vectors of the particles in the CMS. In this system the vector \mathbf{q} can be written as ([15], see figure 4.3.1)

$$(4.3.25) \quad \mathbf{q} = \left(q \sin \left(\frac{\pi - \theta}{2} \right) \cos \phi, q \sin \left(\frac{\pi - \theta}{2} \right) \sin \phi, -q \cos \left(\frac{\pi - \theta}{2} \right) \right)$$

with ϕ and θ the scattering angles. The magnitude of the vector \mathbf{q} can be written down using the cosine rule for triangles

$$(4.3.26) \quad q^2 = p^2 + p^2 - 2pp \cos \theta$$

$$(4.3.27) \quad = 2p^2 (1 - \cos \theta)$$

$$(4.3.28) \quad q = \sqrt{2}p \sqrt{1 - \cos \theta}$$

Putting this in the expression for the \mathbf{q}

$$\begin{aligned} \mathbf{q} &= \left(\sqrt{2}p \sqrt{1 - \cos \theta} \cos \frac{\theta}{2} \cos \phi, \sqrt{2}p \sqrt{1 - \cos \theta} \cos \frac{\theta}{2} \sin \phi, -\sqrt{2}p \sqrt{1 - \cos \theta} \sin \frac{\theta}{2} \right) \\ &= \left(\sqrt{2}p \sqrt{1 - \cos \theta} \sqrt{\frac{1 + \cos \theta}{2}} \cos \phi, \sqrt{2}p \sqrt{1 - \cos \theta} \sqrt{\frac{1 + \cos \theta}{2}} \sin \phi, \right. \\ &\quad \left. -\sqrt{2}p \sqrt{1 - \cos \theta} \sqrt{\frac{1 - \cos \theta}{2}} \right) \\ (4.3.29) \quad &= (p \sin \theta \cos \phi, p \sin \theta \sin \phi, -p (1 - \cos \theta)), \end{aligned}$$

and $q_0 = 0$ (assuming that there is only momentum transfer in the scattering process). Let us now calculate the integral I_3 which is given by

$$(4.3.30) \quad I_3 = \int \frac{d^3 p'_1}{\gamma'_1} \frac{d^3 p'_2}{\gamma'_2} \frac{q_3}{q^4} \delta^{(4)}(p'_1 + p'_2 - p_1 - p_2).$$

Considering the collisions in the CMS to be non-relativistic ($v \ll c$), thus assuming

$$(4.3.31) \quad \gamma'_1 = \gamma'_2 = 1,$$

and putting this in expression (4.3.30) for I_3 together with expression (4.3.29) for \mathbf{q} leads to

$$(4.3.32) \quad I_3 = \int d^3 p'_1 d^3 p'_2 \frac{p(\cos \theta - 1)}{(2p^2(1 - \cos \theta))^2} \delta^{(4)}(p'_1 + p'_2 - W),$$

where W is defined as before. Doing the integration over p'_2 and taking into account that we consider $E'_1 = E'_2$ results in equation (4.3.33) for the integral I_3

$$(4.3.33) \quad I_3 = \Delta_3 I(\Delta^2) = \int \frac{d^3 p'_1 p(\cos \theta - 1) \delta(2E'_1 - W_0)}{(2p^2(1 - \cos \theta))^2}.$$

Inserting now

$$(4.3.34) \quad d^3 p'_1 = 2\pi p'_1 E'_1 dE'_1 d(\cos \theta)$$

in the integration and using equation (4.3.24) ($E'_1 \approx m$ and $p'_1 = p$, considering non-relativistic elastic scattering) this results in

$$(4.3.35) \quad pI(\Delta^2) \simeq -\pi m \int_{\cos \theta_{max}}^{\cos \theta_{min}} d(\cos \theta) \frac{1}{4p^2(1 - \cos \theta)},$$

where we also used $\delta(ax) = \frac{\delta(x)}{|a|}$. Following [15] we define the parameter

$$(4.3.36) \quad \begin{aligned} (\log) &= \frac{1}{2} \int_{\cos \theta_{max}}^{\cos \theta_{min}} d(\cos \theta) \frac{1}{(1 - \cos \theta)} \\ &= \frac{1}{2} \ln \left(\frac{1 - \cos \theta_{max}}{1 - \cos \theta_{min}} \right) \\ &\approx \ln \left(\frac{\theta_{max}}{\theta_{min}} \right), \end{aligned}$$

where the last approximation comes from Taylor expanding the cosines. The problem of this integral is that a scatter angle $\theta_{min} = 0$ makes this integral divergent, representing the scattering of two particles with an infinite distance between them. This represents thus the scattering of a particle in the Coulomb Field produced by a particle at distance infinity and includes thus the assumption from Classical Electro-Dynamics that the Coulomb field of a particle extends to infinity. These minimum and maximum scatter angles are related to the impact parameter b , which, considering non-relativistic Coulomb scattering, is given by

$$(4.3.37) \quad b(\theta) = \frac{m\alpha}{|\mathbf{p}|^2} \cot \left[\frac{\theta}{2} \right] \approx \frac{2m\alpha}{\theta |\mathbf{p}|^2},$$

where \mathbf{p} is the momentum of the particles in the CMS. The choice of what to use here for the minimum and maximum values of the scatter angles is a point of possible discussion. For instance, do we include scattering with an impact parameter bigger than the beam size, or not? Bjorken and Mtingwa⁵ fixed the value of the parameter to be 20 ($(\log) = 20$), but a different choice can be found in for example [15]. We will restrict ourselves here to the choice of Bjorken and Mtingwa.

From (4.3.35) we have

$$(4.3.38) \quad I(\Delta^2) \simeq \frac{-\pi m}{4|\Delta^2|^{3/2}} \ln \left(\frac{\theta_{max}}{\theta_{min}} \right) = \frac{-\pi m}{4|\Delta^2|^{3/2}} (\log),$$

and from the previous calculations and definitions it is straightforward to see that

$$(4.3.39) \quad I_{33} \sim \int d(\cos \theta) \frac{(1 - \cos \theta)^2}{(1 - \cos \theta)^2} \ll (\log)$$

⁵We also assumed the value of this parameter to be 20 in the Particle Tracking Simulations using the Nagaitsev Model (see 5.4).

and does not contain a factor (\log) . Approximating this to zero and comparing with equation (4.3.22) we can conclude that

$$\lambda = 1,$$

from which it follows that

$$(4.3.40) \quad I_{11} = \tilde{I}(\Delta^2)$$

$$(4.3.41) \quad = \int d^3 p'_1 \frac{\delta(2E'_1 - W) p^2 \sin^2 \theta \cos^2 \phi}{(2p^2 (1 - \cos \theta))^2}$$

$$(4.3.42) \quad \simeq \frac{-\pi m}{4|\Delta^2|^{1/2}} (\log).$$

The above results can be summarized as

$$(4.3.43) \quad I_\mu = \frac{-\pi m}{2|\Delta^2|^{3/2}} \Delta_\mu (\log)$$

$$(4.3.44) \quad I_{\mu\nu} = \left(-g_{\mu\nu} + \frac{W_\mu W_\nu}{W^2} - \frac{\Delta_\mu \Delta_\nu}{|\Delta^2|} \right) \frac{\pi m}{2|\Delta^2|^{1/2}} (\log)$$

We now want to return to the laboratory coordinate system. For small quantities we can assume

$$(4.3.45) \quad \frac{\mathbf{W}}{\sqrt{W^2}} = \boldsymbol{\beta} \gamma,$$

with $\boldsymbol{\beta}$ the mean velocity of the particles in the lab system, resulting in

$$(4.3.46) \quad \begin{aligned} I_i \Delta_j + \frac{1}{2} I_{ij} &= \frac{\pi (\log) m}{4|\Delta^2|^{1/2}} \left(-\frac{2\Delta_i \Delta_j}{|\Delta^2|} + \left(\delta_{ij} + \gamma^2 \beta_i \beta_j - \frac{\Delta_i \Delta_j}{|\Delta^2|} \right) \right) \\ &= \frac{\pi (\log) m}{4|\Delta^2|^{1/2}} \left(\delta_{ij} - \frac{3\Delta_i \Delta_j}{|\Delta^2|} + \gamma^2 \beta_i \beta_j \right). \end{aligned}$$

Now we need to know the value of $|\Delta^2|$ in the lab system. But we know that

$$(4.3.47) \quad |\Delta^2| = |\boldsymbol{\Delta}|^2 - \Delta_0^2,$$

and

$$(4.3.48) \quad \boldsymbol{\Delta} \cdot \mathbf{W} = \Delta_0 W_0 - \boldsymbol{\Delta} \cdot \mathbf{W} = 0,$$

so that we can write

$$(4.3.49) \quad \Delta_0 = \frac{\boldsymbol{\Delta} \cdot \mathbf{W}}{W_0} = \boldsymbol{\Delta} \cdot \boldsymbol{\beta}$$

and

$$(4.3.50) \quad |\Delta^2| = |\boldsymbol{\Delta}|^2 - |\boldsymbol{\Delta} \cdot \boldsymbol{\beta}|^2.$$

Putting all of this in the rate equation (equation (4.3.21)) we finally arrive at an expression for the rate equation in the lab system

$$(4.3.51) \quad \frac{d \langle f(p) \rangle}{dt} = \frac{\pi m \alpha^2 N (\log)}{\gamma^2 \tilde{\Gamma}} \int \frac{d^3 \Delta \exp(-\tilde{S}(\boldsymbol{\Delta}))}{\sqrt{|\boldsymbol{\Delta}|^2 - |\boldsymbol{\Delta} \cdot \boldsymbol{\beta}|^2}} \frac{\partial^2 f}{\partial p_i \partial p_j} \left(\delta_{ij} - \frac{3\Delta_i \Delta_j}{(|\boldsymbol{\Delta}|^2 - |\boldsymbol{\Delta} \cdot \boldsymbol{\beta}|^2)} + \gamma^2 \beta_i \beta_j \right).$$

Changing the variables to

$$(4.3.52) \quad \begin{aligned} \Delta_x &= \frac{1}{2} p \theta_x \\ \Delta_s &= \frac{\gamma}{2} p \theta_s \\ \Delta_y &= \frac{1}{2} p \theta_y \end{aligned}$$

takes care of the Lorentz contraction in the longitudinal direction when transforming to the beam rest system. Now define

$$(4.3.53) \quad \tilde{S}(\Delta) = A_{ij} \Delta_i \Delta_j = \frac{\theta_i \theta_j}{4} L_{ij},$$

with

$$(4.3.54) \quad L_{ij} = L_{ij}^{(h)} + L_{ij}^{(l)} + L_{ij}^{(v)},$$

where

$$(4.3.55) \quad L^{(h)} = \frac{\beta_x}{\epsilon_x} \begin{pmatrix} 1 & -\gamma\phi & 0 \\ -\gamma\phi & \frac{\gamma^2 D^2}{\beta_x^2} & 0 \\ 0 & 0 & 0 \end{pmatrix}$$

$$(4.3.56) \quad L^{(l)} = \begin{cases} \frac{\gamma^2}{\sigma_D^2} \begin{pmatrix} 0 & 0 & 0 \\ 0 & 1 & 0 \\ 0 & 0 & 0 \end{pmatrix} & \text{unbunched} \\ \frac{2\gamma^2}{\sigma_{\eta D}^2} \begin{pmatrix} 0 & 0 & 0 \\ 0 & 1 & 0 \\ 0 & 0 & 0 \end{pmatrix} & \text{bunched} \end{cases},$$

$$(4.3.57) \quad L^{(v)} = \frac{\beta_y}{\epsilon_y} \begin{pmatrix} 0 & 0 & 0 \\ 0 & 0 & 0 \\ 0 & 0 & 1 \end{pmatrix},$$

and

$$(4.3.58) \quad \phi = D' - \frac{\beta'_x D}{2\beta_x},$$

with D the Dispersion in the horizontal plane (x-plane). In the above definitions horizontal-vertical coupling, transverse-longitudinal coupling and vertical Dispersion are assumed not to be present. The mathematical treatment of the rate equations including coupling is beyond the scope of this text and can be found in [15]. Using

$$(4.3.59) \quad K_{ij} = \frac{\pi m \alpha^2 N (\log)}{4\gamma^2 \tilde{\Gamma}} \int \frac{d^3 \theta \exp(-\theta_i \theta_j L_{ij}/4)}{(\theta_x^2 + \theta_y^2 + \theta_z^2)^{3/2}} (\delta_{ij} \theta^2 - 3\theta_i \theta_j)$$

and

$$(4.3.60) \quad [Df] = p^2 \begin{pmatrix} \frac{\partial^2 f}{\partial p_x^2} & \frac{\partial^2 f}{\partial p_x \partial p_y} & \gamma \frac{\partial^2 f}{\partial p_x \partial p_z} \\ \frac{\partial^2 f}{\partial p_x \partial p_y} & \frac{\partial^2 f}{\partial p_y^2} & \gamma \frac{\partial^2 f}{\partial p_y \partial p_z} \\ \gamma \frac{\partial^2 f}{\partial p_x \partial p_z} & \gamma \frac{\partial^2 f}{\partial p_y \partial p_z} & \gamma^2 \frac{\partial^2 f}{\partial p_z^2} \end{pmatrix}$$

we can now write down the diffusion equation (4.3.61).

$$(4.3.61) \quad \frac{d \langle f(p) \rangle}{dt} = K_{ij} [D_{ij} f].$$

We will now simplify this diffusion equation. Starting from the equality

$$(4.3.62) \quad \frac{1}{(\theta^2)^{3/2}} = \int_0^\infty \frac{d\lambda \lambda^{1/2}}{4\sqrt{\pi}} \exp(-\lambda \theta^2/4)$$

we can simplify K_{ij} to

$$(4.3.63) \quad K_{ij} = \frac{\pi m \alpha^2 N (\log)}{4\gamma^2 \tilde{\Gamma}} \int \frac{d^3 \theta d\lambda \lambda^{1/2} \exp\left[\frac{-\lambda \theta^2}{4}\right] \exp(-\theta_i \theta_j L_{ij}/4)}{4\sqrt{\pi}} (\delta_{ij} \theta^2 - 3\theta_i \theta_j).$$

Then applying

$$(4.3.64) \quad \theta_i \theta_j \exp(-(\theta_k L_{kl} \theta_l)/4) = -4 \frac{\partial \exp(-(\theta_k L_{kl} \theta_l)/4)}{\partial L_{ij}}$$

to K_{ij} results in equation (4.3.65).

$$(4.3.65) \quad \begin{aligned} K_{ij} &= \frac{\pi m \alpha^2 N (\log)}{4\gamma^2 \tilde{\Gamma}} \int \frac{d^3 \theta d\lambda \lambda^{1/2} \exp\left[\frac{-\lambda \theta^2}{4}\right]}{4\sqrt{\pi}} \left(-4\delta_{ij} \frac{\partial \exp(-(\theta_k L_{kl} \theta_l)/4)}{\partial L_{ij}} + 12 \frac{\partial \exp(-(\theta_k L_{kl} \theta_l)/4)}{\partial L_{ij}} \right), \\ K_{ij} &= \frac{\pi m \alpha^2 N (\log)}{4\gamma^2 \tilde{\Gamma}} \int \frac{d^3 \theta d\lambda \lambda^{1/2}}{4\sqrt{\pi}} \left(-4\delta_{ij} \frac{\partial \exp(-(\lambda \theta_i \theta_i + \theta_i L_{ii} \theta_i)/4)}{\partial L_{ij}} + 12 \frac{\partial \exp(-(\lambda \theta_k \theta_k + \theta_k L_{kl} \theta_l)/4)}{\partial L_{ij}} \right), \\ K_{ij} &= \frac{\pi m \alpha^2 N (\log)}{4\gamma^2 \tilde{\Gamma}} \int \frac{d^3 \theta d\lambda \lambda^{1/2}}{4\sqrt{\pi}} \left(-4\delta_{ij} \frac{\partial \exp(-Tr[L + \lambda I]/4)}{\partial L_{ij}} + 12 \frac{\partial \exp(-(\theta_k (L + \lambda I)_{kl} \theta_l)/4)}{\partial L_{ij}} \right). \end{aligned}$$

Now doing the integration over the Gaussian by using the formula for the integral of a Multivariate Normal Distribution [13]

$$(4.3.66) \quad \int_{-\infty}^{\infty} \exp \left[-\frac{1}{2} \sum_{i,j=1}^n A_{ij} x_i x_j \right] d^n x = \sqrt{\frac{(2\pi)^n}{\det A}}$$

gives for K_{ij}

$$(4.3.67) \quad K_{ij} = \frac{\pi m \alpha^2 N (\log)}{4\gamma^2 \tilde{\Gamma}} \int \frac{d\lambda \lambda^{1/2}}{4\sqrt{\pi}} \left(-4\delta_{ij} \frac{\partial \left[\sqrt{\frac{2^3 (2\pi)^3}{\det[Tr(L + \lambda I)]}} \right]}{\partial L_{ij}} + 12 \frac{\partial \left[\sqrt{\frac{2^3 (2\pi)^3}{\det[L + \lambda I]}} \right]}{\partial L_{ij}} \right).$$

Using ⁶

$$(4.3.68) \quad \frac{\partial}{\partial L_{ij}} \det(L + \lambda I) = \left(\frac{1}{L + \lambda I} \right)_{ij} \det(L + \lambda I),$$

we can calculate the derivatives in equation (4.3.67).

$$(4.3.69) \quad \begin{aligned} \frac{\partial \left[\sqrt{\frac{2^3 (2\pi)^3}{\det[L + \lambda I]}} \right]}{\partial L_{ij}} &= 8\pi\sqrt{\pi} \frac{\partial}{\partial L_{ij}} \left(\sqrt{\frac{1}{\det[L + \lambda I]}} \right) \\ &= 8\pi\sqrt{\pi} \left(\frac{-1}{2} \right) \frac{1}{\sqrt{\det[L + \lambda I]}^3} \frac{\partial \det[L + \lambda I]}{\partial L_{ij}} \\ &= -4\pi\sqrt{\pi} \frac{1}{\sqrt{\det[L + \lambda I]}^3} \left(\frac{1}{L + \lambda I} \right)_{ij} \det[L + \lambda I] \\ &= -4\pi\sqrt{\pi} \left(\frac{1}{L + \lambda I} \right)_{ij} \frac{1}{\sqrt{\det[L + \lambda I]}} \end{aligned}$$

and

$$(4.3.70) \quad \frac{\partial \left[\sqrt{\frac{2^3 (2\pi)^3}{\det[Tr(L + \lambda I)]}} \right]}{\partial L_{ij}} = -4\pi\sqrt{\pi} Tr \left(\frac{1}{L + \lambda I} \right) \frac{1}{\sqrt{\det Tr[L + \lambda I]}}.$$

⁶This comes from: $\det[L + \lambda I] = \sum_j (L + \lambda I)_{ij} \text{Cofactor}(L + \lambda I)_{ij}$

Because the delta function δ_{ij} selects the trace, we can again put the factor $\frac{1}{\sqrt{\det[L+\lambda I]}}$ in front, finally resulting in expression (4.3.71) for K_{ij} .

$$(4.3.71) \quad K_{ij} = \frac{\pi m \alpha^2 N (\log)}{4 \gamma^2 \tilde{\Gamma}} \int_0^\infty \frac{d\lambda \lambda^{1/2}}{(\det(L + \lambda I))^{1/2}} \left(\delta_{ij} \text{Tr} \left(\frac{1}{L + \lambda I} \right) - 3 \left(\frac{1}{L + \lambda I} \right)_{ij} \right).$$

4.4. Growth Rates

In the previous part we determined the diffusion equations for a random function f . Since we are interested in emittance growths we now consider

$$(4.4.1) \quad S_{(x,p)}^{(a)} = \frac{1}{\epsilon_a} \left(\frac{1}{2} \sigma_{ij}^{(a)} \delta p_i \delta p_j + \text{terms in } \delta x \delta p \text{ and in } (\delta x)^2 \right),$$

where the a is referring to the different planes s, x, y and the parameter σ_{ij} only depends on the lattice parameters (Twiss parameters or Optical Functions) and the energy. A straightforward calculation shows that $\langle \epsilon_a S^{(a)} \rangle = \epsilon_a$, the emittance,

$$(4.4.2) \quad \begin{aligned} \langle \epsilon_a S^{(a)} \rangle &= \sigma_{ij}^{(a)} \left\langle \frac{1}{2} \delta p_i \delta p_j + \text{terms in } \delta x \delta p \text{ and in } (\delta x)^2 \right\rangle \\ &= \epsilon_a \frac{\int d^3 x d^3 p S^{(a)} \exp(-S)}{\int d^3 x d^3 p \exp(-S)} \\ &= -\epsilon_a \left(\frac{\partial}{\partial \lambda} \ln \left(\int dx_a dp_a \exp(-\lambda S^{(a)}) \right) \right)_{\lambda=1} \\ &= \epsilon_a. \end{aligned}$$

It is the change of the emittances caused by IBS that we are trying to model, so the emittances are the parameters of interest to us here. The emittance growth is given by equation (4.4.3) (only the term with $\delta p_i \delta p_j$ remains because of the Df operator in the diffusion equation)

$$(4.4.3) \quad \frac{1}{\tau} = \frac{1}{\epsilon_a} \frac{d\epsilon_a}{dt} = \frac{1}{2} A_{ij}^{(a)} \frac{d}{dt} \langle \delta p_i \delta p_j \rangle.$$

First we need to rescale the longitudinal momenta to compensate for the Lorentz contraction, so we multiply the longitudinal momenta with a factor γ . Replacing the matrix $A_{ij}^{(a)}$ with $L_{ij}^{(a)}$ and expressing the derivative in terms of the kernel K_{ij} gives us for the growth rates

$$(4.4.4) \quad \begin{aligned} \frac{1}{\tau_a} &= \sum_{ij} K_{ij} L_{ij}^{(a)} \\ &= \frac{\pi^2 m \alpha^2 N (\log)}{\gamma \tilde{\Gamma}} \left\langle \int_0^\infty \frac{d\lambda \lambda^{1/2}}{(\det(L + \lambda I))^{1/2}} \left[\text{Tr} L^{(a)} \text{Tr} \left(\frac{1}{L + \lambda I} \right) - 3 \text{Tr} L^{(a)} \left(\frac{1}{L + \lambda I} \right) \right] \right\rangle, \end{aligned}$$

the fish brackets defining the average over the whole accelerator ring (in the simulations this integral will become a sum over the different lattice elements along the ring). Summing over the different planes actually simplifies the equation

$$(4.4.5) \quad \frac{1}{\tau} = \sum_a \frac{1}{\tau_a} = \frac{\pi^2 m \alpha N (\log)}{\gamma \tilde{\Gamma}} \left\langle \int_0^\infty \frac{d\lambda \lambda^{1/2}}{(\det(L + \lambda I))^{1/2}} \left[\text{Tr}(L + \lambda I) \text{Tr} \left(\frac{1}{L + \lambda I} \right) - 9 \right] \right\rangle.$$

Considering now the eigenvalues of the matrix L to obey : $\lambda_1 \geq \lambda_2 \geq \lambda_3 \geq 0$, equation (4.4.5) then simplifies to

$$(4.4.6) \quad \frac{1}{\tau} = \frac{\pi^2 m \alpha^2 N (\log)}{\gamma \tilde{\Gamma}} \left\langle (\lambda_1 - \lambda_2)^2 \int_0^\infty \frac{d\lambda \lambda^{1/2}}{(\lambda_1 + \lambda)^{3/2} (\lambda_2 + \lambda)^{3/2} (\lambda_3 + \lambda)^{1/2}} + 2 \text{ cyclic permutations} \right\rangle$$

Here we used

$$(4.4.7) \quad \begin{aligned} \det [L + \lambda I] &= \det P^{-1} \det [L + \lambda I] \det P \\ &= \det [P^{-1} L P + \lambda P^{-1} P] \\ &= \det \begin{bmatrix} \lambda_1 + \lambda & 0 & 0 \\ 0 & \lambda_2 + \lambda & 0 \\ 0 & 0 & \lambda_3 + \lambda \end{bmatrix}, \end{aligned}$$

with the columns of matrix P the eigenvectors of the matrix $L + \lambda I$. An important remark here is that if $\phi \neq 0$ (defined in equation (4.3.58)) the eigenvalues cannot all be equal, forcing the emittance to grow at least in one plane. The parameter H shown below is called the Dispersion Invariant, and assuming $\lambda_1 > \lambda_2 \approx \lambda_3$ it can be analytically calculated

$$(4.4.8) \quad H \equiv \left((\lambda_1 - \lambda_2)^2 \int_0^\infty \frac{d\lambda \lambda^{1/2}}{(\lambda_1 + \lambda)^{3/2} (\lambda_2 + \lambda)^{3/2} (\lambda_3 + \lambda)^{1/2}} + 2 \text{ cyclic permutations} \right)$$

$$(4.4.9) \quad = \left(\frac{2(\lambda_1 + 2\lambda_2)}{\sqrt{\lambda_2(\lambda_1 - \lambda_2)}} \sin^{-1} \left(\sqrt{\frac{\lambda_1 - \lambda_2}{\lambda_1}} \right) - 6 \right).$$

For the case $\lambda_1 > \lambda_2 > \lambda_3$, H can be expressed in terms of elliptic integrals of the first and second kind

$$(4.4.10) \quad F(\psi, k) = \int_0^\psi \frac{d\alpha}{\sqrt{1 - k^2 \sin^2 \alpha}}$$

$$(4.4.11) \quad E(\psi, k) = \int_0^\psi \sqrt{1 - k^2 \sin^2 \alpha} d\alpha,$$

where the parameters are defined as

$$(4.4.12) \quad \psi = \arcsin \left(\sqrt{\frac{\lambda_1 - \lambda_3}{\lambda_1}} \right)$$

and

$$(4.4.13) \quad k = \sqrt{\frac{\lambda_1(\lambda_2 - \lambda_3)}{\lambda_2(\lambda_1 - \lambda_3)}},$$

ultimately resulting in the three integrals:

$$(4.4.14) \quad \begin{aligned} \int_0^\infty \frac{d\lambda \lambda^{1/2}}{(\lambda_1 + \lambda)^{3/2} (\lambda_2 + \lambda)^{3/2} (\lambda_3 + \lambda)^{1/2}} &= \frac{2}{(\lambda_1 - \lambda_2)} \left[\frac{2}{(\lambda_1 - \lambda_2)} \left\{ \sqrt{\frac{\lambda_2}{\lambda_1 - \lambda_3}} E(\psi, k) - 1 \right\} \right. \\ &\quad \left. + \frac{1}{\sqrt{\lambda_2(\lambda_1 - \lambda_3)}} \left\{ E(\psi, k) + \frac{\lambda_3}{\lambda_2 - \lambda_3} (E(\psi, k) + F(\psi, k)) \right\} \right] \end{aligned}$$

$$\begin{aligned}
(4.4.15) \quad \int_0^\infty \frac{d\lambda \lambda^{1/2}}{(\lambda_1 + \lambda)^{3/2} (\lambda_3 + \lambda)^{3/2} (\lambda_2 + \lambda)^{1/2}} &= \frac{2}{(\lambda_1 - \lambda_2)} \sqrt{\frac{\lambda_2}{(\lambda_1 - \lambda_3)^3}} \\
&\quad \left[E(\psi, k) + \left(\frac{\lambda_2 - \lambda_1}{\lambda_2 - \lambda_3} \right) \{E(\psi, k) - F(\psi, k)\} - \sqrt{\frac{\lambda_1 - \lambda_3}{\lambda_2}} \right] \\
(4.4.16) \quad \int_0^\infty \frac{d\lambda \lambda^{1/2}}{(\lambda_2 + \lambda)^{3/2} (\lambda_3 + \lambda)^{3/2} (\lambda_1 + \lambda)^{1/2}} &= \frac{2}{(\lambda_1 - \lambda_2)(\lambda_2 - \lambda_3)} \left\{ 1 + \left[\sqrt{\frac{\lambda_2}{(\lambda_1 - \lambda_3)}} - \frac{2\sqrt{\lambda_2(\lambda_1 - \lambda_3)}}{(\lambda_2 - \lambda_3)} \right] E(\psi, k) \right. \\
&\quad \left. + \frac{(\lambda_2 + \lambda_3)(\lambda_1 - \lambda_2)}{(\lambda_2 - \lambda_3)\sqrt{\lambda_2(\lambda_1 - \lambda_3)}} \right\}
\end{aligned}$$

Depending on the specific case some of the above integrals will need to be calculated to determine the IBS growth rates. In particle tracking simulations this means that for each macro particle⁷ on the mesh we need to evaluate these integrals at each point in time where we would like to track it (usually after some number of turns in the machine), and with these results update the positions in phase-space of the tracked macro particles. Overall parameters can then be calculated from the updated phase-space coordinates. The fact that most of these integrals cannot be solved analytically in most cases is the reason for the different models I describe further in this text (see Chapter 5). Each model has a different approach for solving these integrals using different assumptions. In any case the above equations should convince the reader that evaluating them can be time and resource consuming. So if we want to simulate the behavior of the beam over an acceptable time-window with respect to IBS, within a reasonable time-frame, an efficient numerical approach is necessary. We conclude the discussion of the BM calculations by stating the growth rate expressed in function of the dispersion invariant,

$$(4.4.17) \quad \frac{1}{\tau} = \frac{\pi^2 \alpha^2 m N (\log)}{\gamma \Gamma} \langle H(\lambda_1, \lambda_2, \lambda_3) \rangle,$$

together with a property of the dispersion invariant that might be handy in its evaluation,

$$(4.4.18) \quad H(a\lambda_1, a\lambda_2, a\lambda_3) = H(\lambda_1, \lambda_2, \lambda_3).$$

⁷A macro particle is a particle in the computer simulation representing a number of real particles in the machine. The number of real particles associated with a macro particle can be set in the simulation software. The more macro particles are chosen the less real particles they represent and the better the simulation should approach the behavior of the real particles within the beam. Of course more macro particles means more integrations thus immediately translates in longer simulation times. Thus choosing the number of macro particles in a simulation is a trade-off between simulation time and accuracy.

Alternatives to the Bjorken-Mtingwa Model

5.1. Introduction

There are different models available to calculate IBS growth rates of the emittances. One of the first models describing a method that is widely used is the Piwinski Model. In subsection 5.2 I give a short overview of the different steps in the model. The Piwinski model treats the scattering of the particles in a classical relativistic way making it more accessible as a first introduction to IBS. Other models start from the BM formulas but introduce some assumptions to simplify the calculations of the integrals that appear in the derivations. In the next sections I will go through the models that are implemented in the particle tracking software. This particle tracking software, written in FORTRAN, that we used to simulate the IBS effects in the LHC was developed by Roderik Bruce (CERN/LUND University) and Mike Blaskiewicz (BNL) in collaboration with John Jowett (CERN).

5.2. The Piwinski Model

5.2.1. Introduction. To understand the effects of IBS one usually starts by reading the Piwinski Model as an introduction to the subject. The method used by Piwinski to calculate IBS growth rates is pretty straightforward and the physics is clear. The different steps in the calculations can be summarized as [6]:

- Transform the momenta of the two colliding particles into their CMS system
- Calculate the momentum changes due to the collision
- Transform the momenta after collision back to the lab system
- Calculate the changes in emittance and in synchrotron oscillation amplitude
- Average over all scattering angles using the Rutherford scattering cross-section
- Average over all momenta and positions of colliding particles (in this model a Gaussian distribution is assumed)
- Observe the different behavior below and above transition energy
- Calculate the rise or damping times for the bunch dimensions.

5.2.2. The Equations. I will not go through the calculations of this model but only state the final results, noting that here $\beta'_{x,y}$ and $D'_{x,y}$ [9] are neglected. Gaussian distributions are assumed in all three planes. The growth rates are given by

$$\begin{aligned}
 \frac{1}{T_p} &= \left\langle A \frac{\sigma_h^2}{\sigma_p^2} f(a, b, q) \right\rangle, \\
 \frac{1}{T_x} &= \left\langle A \left[f\left(\frac{1}{a}, \frac{b}{a}, \frac{q}{a}\right) + \frac{D_x^2 \sigma_h^2}{\sigma_{x\beta}^2} f(a, b, q) \right] \right\rangle, \\
 \frac{1}{T_y} &= \left\langle A \left[f\left(\frac{1}{b}, \frac{a}{b}, \frac{q}{b}\right) + \frac{D_y^2 \sigma_h^2}{\sigma_{y\beta}^2} f(a, b, q) \right] \right\rangle,
 \end{aligned}
 \tag{5.2.1}$$

where

$$(5.2.2) \quad A = \frac{r_0^2 c N_b}{64 \pi^2 \beta^3 \gamma^4 \epsilon_x \epsilon_y \sigma_x \sigma_y},$$

$$(5.2.3) \quad \frac{1}{\sigma_h^2} = \frac{1}{\sigma_p^2} + \frac{D_x^2}{\sigma_{x\beta}^2} + \frac{D_y^2}{\sigma_{y\beta}^2},$$

$$(5.2.4) \quad a = \frac{\sigma_h \beta_x}{\gamma \sigma_{x\beta}}, \quad b = \frac{\sigma_h \beta_y}{\gamma \sigma_{y\beta}}, \quad q = \sigma_h \beta \sqrt{\frac{2d}{r_0}},$$

$$(5.2.5) \quad P^2 = a^2 + (1 - a^2) u^2, \quad Q^2 = b^2 + (1 - b^2) u^2,$$

$$(5.2.6) \quad f(a, b, q) = 8\pi \int_0^1 \left(2 \ln \left[\frac{q}{2} \left(\frac{1}{P} + \frac{1}{Q} \right) - 0.577... \right] \right) \frac{1 - 3u^2}{PQ} du,$$

and the function f has the property

$$(5.2.7) \quad f(a, b, q) + \frac{1}{a^2} f\left(\frac{1}{a}, \frac{b}{a}, \frac{q}{a}\right) + \frac{1}{b^2} f\left(\frac{1}{b}, \frac{a}{b}, \frac{q}{b}\right) = 0.$$

The constant r_0 represents the classical radius of the particles¹ in the beam, d is the minimum of the beam radii in the x and y plane and is related to the impact parameter or the (log) factor in BM, $\epsilon_{x,y} = \frac{\sigma_{x,y}^2}{\beta_{x,y}}$ are the transverse emittances and N_b is the number of particles in the bunch for bunched beams or in the beam for unbunched beams. The $\sigma_{x,y\beta}$ refer to the standard deviation of the Betatron amplitude of the particles in the beam with respect to the closed orbit for the momentum deviation σ_p , thus not incorporating its Dispersion. The number 0.577... is the Euler-Mascheroni constant.²

5.2.3. Remarks on Simulations with Piwinski Model. The Piwinski formulas can now be applied in two ways for the particle tracking algorithms. One way is to apply the formulas to all the parameters averaged over the ring. These averaged values are produced using the MAD-X program 6 . This approximation is often referred to as a smooth lattice approximation and speed is the main advantage of this approach. The formulas above can be evaluated fast enough so that they can be done during the simulation run. The downside of this method is that it is known to overestimate the IBS growth, which is partially solved in the simulation software by weighting the growth rates with a factor that is used as an input to the simulation program. A weighting factor of 0.9 in most cases leads to a good agreement with the other models.

In a second approach the growth rates are determined over all the lattice elements around the accelerator ring and are then summed over. This method is of course much slower than the previous approach but gives more accurate values for the growth rates. In this approach there are two different algorithms implemented in the simulation software, one using the classical Piwinski equations (5.2.1) and another also using the equations (5.2.1) but the term $\frac{D_x^2}{\sigma_{x\beta}^2}$ is replaced by the dispersion invariant $H = D_x^2 + \frac{(\beta_x D'_x - 0.5 D_x \beta'_x)^2}{\beta_x}$, hence β'_x and D'_x are now taking into account loosening somewhat the restrictions in the classical Piwinski model (I will refer to this last algorithm as piwimodified in the rest of this text).

To handle the speed problem and make the software more flexible, the simulation software was extended with an algorithm called interpolat. To apply this algorithm in the simulations one needs to add an external file to the simulation folder containing precalculated growth rates over a lattice of the input parameters : the emittances in the transverse planes, the bunch length and the momentum spread (ie. $\epsilon_x, \epsilon_y, \sigma_s$ and σ_p). The big advantage of this method is that any model can be used to generate this table of growth rates in the file. Here these growth rates are calculated using the piwimodified algorithm that was put in a separate program dedicated to producing such table files. In this way one can choose an acceptable lattice and create the needed table file off line (not during the actual simulation). The interpolat algorithm then uses trilinear

¹The classical radius of an ion with respect to the proton radius is given by $R = R_0 A^{1/3}$ assuming spherical charge distributions for the nuclei.

²The Euler-Mascheroni constant is defined as $\int_1^\infty \left(\frac{1}{[x]} - \frac{1}{x} \right) dx$

interpolation on the lattice in this external file to calculate the growth rates during the simulation run and thus recuperating partially the speed loss by reusing the external file for different simulations.

I will compare the results of these different approaches in the part on simulations further in this text (see 7.3).

5.3. The Bane Model

5.3.1. Introduction. The discussion and use of the Bane Model [11] is motivated by a search for a time efficient algorithm to use in the simulations. Although this model also makes use of an external file, no integrals have to be calculated during the simulation and only a one dimensional interpolation needs to be done instead of a trilinear interpolation as in the interpolat method.

5.3.2. The equations. To simplify the calculations Bane introduced a new function $g(\alpha)$. Assuming that $a, b \ll 1$ with equations (5.3.1) and (5.3.2)

$$(5.3.1) \quad \frac{1}{\sigma_H^2} = \frac{1}{\sigma_p^2} + \frac{H_x}{\epsilon_x} + \frac{H_y}{\epsilon_y}$$

$$(5.3.2) \quad a = \frac{\sigma_H}{\gamma} \sqrt{\frac{\beta_x}{\epsilon_x}}, \quad b = \frac{\sigma_H}{\gamma} \sqrt{\frac{\beta_y}{\epsilon_y}}$$

the function $g(\alpha)$ is given by equation (5.3.3).

$$(5.3.3) \quad g(\alpha) = \frac{2\sqrt{\alpha}}{\pi} \int_0^\infty \frac{du}{\sqrt{1+u^2}\sqrt{\alpha^2+u^2}}.$$

With this new function the growth rate equations become

$$(5.3.4) \quad \begin{aligned} \frac{1}{T_p} &\approx \frac{r_0^2 c N (\log)}{16 \gamma^3 \epsilon_x^{3/4} \epsilon_y^{3/4} \sigma_s \sigma_p^3} \left\langle \sigma_H g\left(\frac{a}{b}\right) (\beta_x \beta_y)^{-1/4} \right\rangle \\ \frac{1}{T_{x,y}} &\approx \frac{\sigma_p^2 \langle H_{x,y} \rangle}{\epsilon_{x,y}} \frac{1}{T_p} \end{aligned}$$

where the $H_{x,y}$ refer to the Dispersion Invariants in the transverse planes. The behavior of Bane's $g(\alpha)$ is plotted in figure 5.3.1.

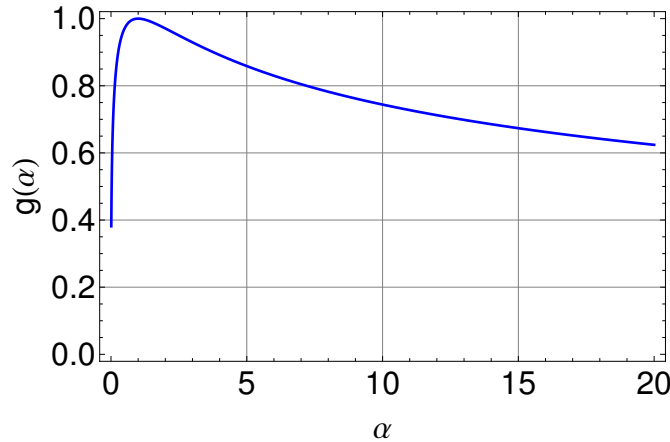


FIGURE 5.3.1. Bane's $g(\alpha)$]

Bane shows in his paper that the high-energy limit of his approximation is the same as for the piwimodified algorithm. So the Bane algorithm is best suited for simulations at high energy.

5.4. The Nagaitsev Model

5.4.1. Introduction. Just like the Bane Model the discussion of the Nagaitsev Model [18] is motivated by looking for a time efficient algorithm for calculating the IBS growth rates. The Nagaitsev algorithm however does not rely on an approximating function like the Bane algorithm but is based on Carlson's symmetric elliptical integral of the second kind that is defined in equation (5.4.1)

$$(5.4.1) \quad R_D(x, y, z) = \frac{3}{2} \int_0^\infty \frac{dt}{\sqrt{(t+x)(t+y)(t+z)^3}},$$

which has the properties

$$(5.4.2) \quad R_D(x, x, x) = x^{-3/2}$$

$$(5.4.3) \quad R_D(x, y, z) + R_D(y, z, x) + R_D(z, x, y) = \frac{3}{\sqrt{xyz}}$$

$$(5.4.4) \quad R_D(hx, hy, hz) = h^{-3/2} R_D(x, y, z).$$

The fact that there exists a very efficient numerical algorithm [1] to calculate the integral in (5.4.1) makes this algorithm fast enough to calculate the integrals in the PTS during the simulation run, so that no precalculated external file is necessary. The advantage of using these integrals is that the accuracy is determined by the numerical algorithm for calculating the integral that can be set in the algorithm and not by some approximating function like in the Bane Model, making this the most accurate model implemented in the PTS. A disadvantage is that this model does not take vertical dispersion into account while the Bane Model does. I attempted to use these integrals to incorporate vertical dispersion but this failed because the introduction of vertical dispersion creates negative eigenvalues for the matrix A as defined in (4.1.3). The Carlson integral $R_D(x, y, z)$ described here unfortunately can only be calculated when z is positive, $x \geq 0$, $y \geq 0$ and not zero at the same time. In the Nagaitsev Model (x, y, z) are the eigenvalues of the A matrix making incorporation of vertical dispersion by use of Carlson integrals impossible. This algorithm has been implemented in the PTS by myself and Roderik Bruce, adding a new algorithm to the set already available in the PTS.

A more detailed discussion of the numerical algorithm and Carlson's integrals can be found in [1].

5.4.2. The equations. Equation (5.4.5) shows how in [18] the IBS growth rates (equations (4.4.5)) are rewritten as a function Ψ of these Carlson symmetric elliptical integrals of the second kind.

$$(5.4.5) \quad \frac{1}{\tau} = \frac{2\pi^2 N c r_{p, Pb}^2 M^3 (\log)}{3\gamma\Gamma} \int_0^C \frac{ds}{C\sqrt{\lambda_1\lambda_2\lambda_3}} \left[\lambda_1 \Psi\left(\frac{1}{\lambda_1}, \frac{1}{\lambda_2}, \frac{1}{\lambda_3}\right) + \text{two cyclic permutations} \right]$$

$$\Psi(x, y, z) = -2xR_D(y, z, x) + yR_D(z, x, y) + zR_D(x, y, z)$$

Nagaitsev now only considered uncoupled betatron motion and neglected contributions of the vertical dispersion. With these assumptions the action variables for the different planes can be written as

$$(5.4.6) \quad J_x = \frac{1}{2\beta_x} (x - D_x \delta)^2 + \frac{\beta_x}{2} \left(x' - \frac{\beta'_x}{2\beta_x} x - \phi_x \delta \right)^2$$

$$(5.4.7) \quad J_y = \frac{1}{2\beta_y} y^2 + \frac{\beta_y}{2} \left(y' - \frac{\beta'_y}{2\beta_y} y \right)^2$$

$$(5.4.8) \quad J_s = \frac{s^2}{2k_s} + \frac{k_s}{2} \delta^2$$

with

$$(5.4.9) \quad \phi_x = D'_x - \frac{\beta'_x D_x}{2\beta_x}$$

Now defining

$$(5.4.10) \quad a_x = \frac{\beta_x}{\epsilon_x}$$

$$(5.4.11) \quad a_y = \frac{\beta_y}{\epsilon_y}$$

$$(5.4.12) \quad \sigma_x = \sqrt{D_x^2 \sigma_p^2 + \beta_x \epsilon_x}$$

$$(5.4.13) \quad \sigma_y = \sqrt{\beta_y \epsilon_y}$$

$$(5.4.14) \quad a_s = a_x \left(\frac{D_x^2}{\beta_x^2} + \Phi^2 \right) + \frac{1}{\sigma_p^2}$$

$$(5.4.15) \quad a_1 = \frac{1}{2} (a_x + \gamma^2 a_s)$$

$$(5.4.16) \quad a_2 = \frac{1}{2} (a_x - \gamma^2 a_s)$$

$$(5.4.17) \quad \lambda_1 = a_y$$

$$(5.4.18) \quad \lambda_2 = a_1 + \sqrt{a_2^2 + \gamma^2 a_x^2 \phi_x^2}$$

$$(5.4.19) \quad \lambda_3 = a_1 - \sqrt{a_2^2 + \gamma^2 a_x^2 \phi_x^2}$$

$$(5.4.20) \quad R_1 = \frac{1}{\lambda_1} R_D \left[\frac{1}{\lambda_2}, \frac{1}{\lambda_3}, \frac{1}{\lambda_1} \right]$$

$$(5.4.21) \quad R_2 = \frac{1}{\lambda_2} R_D \left[\frac{1}{\lambda_3}, \frac{1}{\lambda_1}, \frac{1}{\lambda_2} \right]$$

$$(5.4.22) \quad R_3 = \frac{1}{\lambda_3} R_D \left[\frac{1}{\lambda_1}, \frac{1}{\lambda_2}, \frac{1}{\lambda_3} \right] = 3 \sqrt{\frac{\lambda_1 \lambda_2}{\lambda_3}} - \frac{\lambda_1}{\lambda_3} R_1 - \frac{\lambda_2}{\lambda_3} R_2$$

where the λ 's are the eigenvalues of matrix A (see equation (4.1.3)). Now using

$$(5.4.23) \quad \begin{aligned} \frac{1}{\tau} &= \frac{1}{\epsilon_x} \frac{d\epsilon_x}{dt} + \frac{1}{\epsilon_y} \frac{d\epsilon_y}{dt} + \frac{1}{\sigma_p^2} \frac{d\sigma_p^2}{dt} \\ &= \frac{2\pi^2 N c r_{p,Pb}^2 M^3 (\log)}{3\gamma\Gamma} \end{aligned}$$

$$(5.4.24) \quad \int_0^C \frac{ds}{C \sqrt{\lambda_1 \lambda_2 \lambda_3}} \left[\lambda_1 \Psi \left(\frac{1}{\lambda_1}, \frac{1}{\lambda_2}, \frac{1}{\lambda_3} \right) + \text{two cyclic permutations} \right]$$

$$(5.4.25) \quad \Gamma = 8\pi^3 \beta^3 \gamma^3 M^3 c^3 \epsilon_x \epsilon_y \sigma_s \sigma_p$$

where β is the relativistic parameter here and not the Optical Function, allows us to write for the different growth rates

$$(5.4.26) \quad \frac{d\sigma_p^2}{dt} = \frac{N r_p^2 c (\log)}{12\pi \beta^3 \gamma^5 \sigma_s} \int_0^C \frac{S_p}{C \sigma_x \sigma_y} ds$$

$$(5.4.27) \quad \frac{d\epsilon_y}{dt} = \frac{N r_p^2 c (\log)}{12\pi \beta^3 \gamma^5 \sigma_s} \int_0^C \frac{\beta_y}{C \sigma_x \sigma_y} \Psi \left[\frac{1}{\lambda_1}, \frac{1}{\lambda_2}, \frac{1}{\lambda_3} \right] ds$$

$$(5.4.28) \quad \frac{d\epsilon_x}{dt} = \frac{N r_p^2 c (\log)}{12\pi \beta^3 \gamma^5 \sigma_s} \int_0^C \frac{\beta_x}{C \sigma_x \sigma_y} \left[S_x + \left(\frac{D_x^2}{\beta_x^2} + \phi_x^2 \right) S_p + S_{xp} \right] ds$$

Here C is the accelerators circumference, r_p the classical radius of the particles, (\log) the BM parameter³ (that we chose to set to 20 in our simulations, but different values can be set in the input file for the PTS simulation) and

$$(5.4.29) \quad S_p = \frac{\gamma^2}{2} \left[2R_1 - R_2 \left(1 - \frac{3a_2}{\sqrt{a_2^2 + \gamma^2 a_x^2 \phi_x^2}} \right) - R_3 \left(1 + \frac{3a_2}{\sqrt{a_2^2 + \gamma^2 a_x^2 \phi_x^2}} \right) \right]$$

$$(5.4.30) \quad S_x = \frac{1}{2} \left[2R_1 - R_2 \left(1 + \frac{3a_2}{\sqrt{a_2^2 + \gamma^2 a_x^2 \phi_x^2}} \right) - R_3 \left(1 - \frac{3a_2}{\sqrt{a_2^2 + \gamma^2 a_x^2 \phi_x^2}} \right) \right]$$

$$(5.4.31) \quad S_{xp} = \frac{3\gamma^2 \phi_x^2 a_x}{\sqrt{a_2^2 + \gamma^2 a_x^2 \phi_x^2}} (R_2 - R_3)$$

All of the above equations are now implemented in the FORTRAN code of the PTS.

5.5. The Zimmerman Model

5.5.1. Introduction. This model, developed by Frank Zimmerman at CERN [25], is based on the BM Model but incorporates horizontal Dispersion and vertical Dispersion. This model is implemented in the MAD-X (See Chapter 6) software, but not in the PTS software, because evaluating the integrals would increase the simulation to much to be practical. It is also known that there is an error in this model, caused by a typo in the calculation in Mathematica where Frank Zimmerman used a regular multiplication instead of a matrix multiplication in one of the equations. I have been working on correcting these equations, my corrected version and some cases comparing the two sets of equations are shown in subsection 5.5.3.

5.5.2. The Equations. The L-matrices (compare to equations 4.3.55, 4.3.56 and 4.3.57 in the BM Model) used by Frank Zimmerman are given by

$$(5.5.1) \quad L^{(h)} = \frac{\beta_x}{\epsilon_x} \begin{pmatrix} 1 & -\gamma\phi_x & 0 \\ -\gamma\phi_x & \gamma^2 \frac{H_x}{\beta_x} & 0 \\ 0 & 0 & 0 \end{pmatrix}$$

$$(5.5.2) \quad L^{(l)} = \frac{\gamma^2}{\sigma_\delta^2} \begin{pmatrix} 0 & 0 & 0 \\ 0 & 1 & 0 \\ 0 & 0 & 0 \end{pmatrix}$$

$$(5.5.3) \quad L^{(v)} = \frac{\beta_y}{\epsilon_y} \begin{pmatrix} 0 & 0 & 0 \\ 0 & \gamma^2 \frac{H_y}{\beta_y} & -\gamma\phi_y \\ 0 & 0 - \gamma\phi_y & 1 \end{pmatrix}$$

where

$$(5.5.4) \quad \phi_{x,y} \equiv D'_{x,y} - \frac{\beta'_{x,y} D_{x,y}}{2\beta_{x,y}}$$

$$(5.5.5) \quad H_{x,y} = \frac{D_{x,y}^2 + \beta_{x,y}^2 \phi_{x,y}^2}{\beta_{x,y}}$$

³At the time of writing we were working on implementing the online calculation of the Coulomb Logarithm based on the equations on page 635 in [21].

With all of the above definitions the IBS growth rates can be written as (equations (8) in [25])

$$\begin{aligned}
 (5.5.6) \quad \frac{1}{\tau_x} &= \frac{\pi^2 r_0^2 v_c m^3 N (\log)}{\gamma \Gamma} \left[\frac{\gamma^2 H_x}{\epsilon_x} \right] \int_0^\infty \frac{d\lambda \lambda^{1/2} [a_x \lambda + b_x]}{(\lambda^3 + a\lambda^2 + b\lambda + c)^{3/2}} \\
 \frac{1}{\tau_y} &= \frac{\pi^2 r_0^2 v_c m^3 N (\log)}{\gamma \Gamma} \left[\frac{\beta_y}{\epsilon_y} \right] \int_0^\infty \frac{d\lambda \lambda^{1/2} [a_y \lambda + b_y]}{(\lambda^3 + a\lambda^2 + b\lambda + c)^{3/2}} \\
 \frac{1}{\tau_l} &= \frac{\pi^2 r_0^2 v_c m^3 N (\log)}{\gamma \Gamma} \left[\frac{\gamma^2}{\sigma_\delta^2} \right] \int_0^\infty \frac{d\lambda \lambda^{1/2} [a_l \lambda + b_l]}{(\lambda^3 + a\lambda^2 + b\lambda + c)^{3/2}}
 \end{aligned}$$

where

$$\begin{aligned}
 a &= \gamma^2 \left(\frac{H_x}{\epsilon_x} + \frac{H_y}{\epsilon_y} \right) + \frac{\gamma^2}{\sigma_\delta^2} + \left(\frac{\beta_x}{\epsilon_x} + \frac{\beta_y}{\epsilon_y} \right) \\
 b &= \left(\frac{\beta_x}{\epsilon_x} + \frac{\beta_y}{\epsilon_y} \right) \left(\frac{\gamma^2 D_x^2}{\epsilon_x \beta_x} + \frac{\gamma^2 D_y^2}{\epsilon_y \beta_y} + \frac{\gamma^2}{\sigma_\delta^2} \right) + \frac{\beta_x \beta_y}{\epsilon_x \epsilon_y} \gamma^2 (\phi_x^2 + \phi_y^2) + \frac{\beta_x \beta_y}{\epsilon_x \epsilon_y} \\
 c &= \frac{\beta_x \beta_y}{\epsilon_x \epsilon_y} \left(\frac{\gamma^2 D_x^2}{\epsilon_x \beta_x} + \frac{\gamma^2 D_y^2}{\epsilon_y \beta_y} + \frac{\gamma^2}{\sigma_\delta^2} \right) \\
 a_x &= 2\gamma^2 \left(\frac{H_x}{\epsilon_x} + \frac{H_y}{\epsilon_y} + \frac{1}{\sigma_\delta^2} \right) - \frac{\beta_x H_y}{H_x \epsilon_y} + \frac{\beta_x}{H_x \gamma^2} \left(\frac{2\beta_x}{\epsilon_x} - \frac{\beta_y}{\epsilon_y} - \frac{\gamma^2}{\sigma_\delta^2} \right) \\
 b_x &= \left(\frac{\beta_x}{\epsilon_x} + \frac{\beta_y}{\epsilon_y} \right) \left(\gamma^2 \left(\frac{H_x}{\epsilon_x} + \frac{H_y}{\epsilon_y} \right) + \frac{\gamma^2}{\sigma_\delta^2} \right) - \gamma^2 \left(\frac{\beta_x^2}{\epsilon_x^2} \phi_x^2 + \frac{\beta_y^2}{\epsilon_y^2} \phi_y^2 \right) + \left(\frac{\beta_x}{\epsilon_x} - 4 \frac{\beta_y}{\epsilon_y} \right) \frac{\beta_x}{\epsilon_x} + \\
 &\quad \frac{\beta_x}{\gamma^2 H_x} \left(\frac{\gamma^2}{\sigma_\delta^2} \left(\frac{\beta_x}{\epsilon_x} - \frac{2\beta_y}{\epsilon_y} \right) + \frac{\beta_x \beta_y}{\epsilon_x \epsilon_y} + \gamma^2 \left(\frac{2\beta_y^2}{\epsilon_y^2} \phi_y^2 - \frac{\beta_x^2}{\epsilon_x^2} \phi_x^2 \right) \right) + \frac{\beta_x H_y}{H_x \epsilon_y} \left(\frac{\beta_x}{\epsilon_x} - \frac{2\beta_y}{\epsilon_y} \right) \\
 a_l &= 2\gamma^2 \left(\frac{H_x}{\epsilon_x} + \frac{H_y}{\epsilon_y} + \frac{1}{\sigma_\delta^2} \right) - \frac{\beta_x}{\epsilon_x} - \frac{\beta_y}{\epsilon_y} \\
 b_l &= \left(\frac{\beta_x}{\epsilon_x} + \frac{\beta_y}{\epsilon_y} \right) \left(\gamma^2 \left(\frac{H_x}{\epsilon_x} + \frac{H_y}{\epsilon_y} \right) + \frac{\gamma^2}{\sigma_\delta^2} \right) - 2 \frac{\beta_x \beta_y}{\epsilon_x \epsilon_y} - \gamma^2 \left(\frac{2\beta_y^2}{\epsilon_y^2} \phi_y^2 + \frac{\beta_x^2}{\epsilon_x^2} \phi_x^2 \right) \\
 a_y &= -\gamma^2 \left(\frac{H_x}{\epsilon_x} + \frac{2H_y}{\epsilon_y} + \frac{\beta_x H_y}{\beta_y H_x} + \frac{1}{\sigma_\delta^2} \right) + 2\gamma^2 \frac{H_y}{\beta_y} \left(\frac{H_y}{\epsilon_y} + \frac{H_x}{\epsilon_x} \right) + \frac{2\gamma^4 H_y}{\beta_y \sigma_\delta^2} - \left(\frac{\beta_x}{\epsilon_x} - \frac{2\beta_y}{\epsilon_y} \right) \\
 b_y &= \gamma^2 \left(\frac{\beta_y}{\epsilon_y} - \frac{2\beta_x}{\epsilon_x} \right) \left(\frac{H_x}{\epsilon_x} + \frac{1}{\sigma_\delta^2} \right) + \left(\frac{\beta_y}{\epsilon_y} - \frac{4\beta_x}{\epsilon_x} \right) \frac{\gamma^2 H_y}{\epsilon_y} + \frac{\beta_x \beta_y}{\epsilon_x \epsilon_y} + \gamma^2 \left(\frac{2\beta_x^2}{\epsilon_x^2} \phi_x^2 - \frac{\beta_y^2}{\epsilon_y^2} \phi_y^2 \right) \\
 &\quad + \frac{\gamma^4 H_y}{\beta_y} \left(\frac{\beta_x}{\epsilon_x} + \frac{\beta_y}{\epsilon_y} \right) \left(\frac{H_y}{\epsilon_y} + \frac{1}{\sigma_\delta^2} \right) + \left(\frac{\beta_x}{\epsilon_x} + \frac{\beta_y}{\epsilon_y} \right) \gamma^4 \frac{H_x H_y}{\beta_y \epsilon_x} - \gamma^4 \frac{H_y}{\beta_y} \left(\frac{\beta_y^2}{\epsilon_y^2} \phi_y^2 + \frac{\beta_x^2}{\epsilon_x^2} \phi_x^2 \right)
 \end{aligned}$$

5.5.3. Corrected Version. The equations below show my corrected version of the equations used by Frank Zimmerman. If an equation form the above set is not repeated it means that I had the same result.

	Original	Corrected	Difference
τ_d	2.37826	2.37826	0.
τ_x	7.9507	7.95335	-0.00265161
τ_y	4215.21	4204.57	10.6421

FIGURE 5.5.1. Comparison Zimmerman Corrected and Uncorrected

	Original	Corrected	Difference
τ_d	4.77163	4.77238	-0.000752538
τ_x	14.688	14.6943	-0.00634605
τ_y	9108.93	9092.39	16.5441

FIGURE 5.5.2. Comparison Zimmerman Corrected and Uncorrected

$$\begin{aligned}
a_{x,corrected} &= -\frac{\beta_x}{\sigma_\delta^2 H_x} + \frac{6\beta_x^2 \phi_x^2}{H_x \epsilon_x} + \frac{\frac{2\beta_x^2}{\epsilon_x} - \frac{\beta_x \beta_y}{\epsilon_y}}{\gamma^2 H_x} - \frac{H_y \beta_x}{H_x \epsilon_y} + 2\gamma^2 \left(\frac{1}{\sigma_\delta^2} + \frac{H_x}{\epsilon_x} + \frac{H_y}{\epsilon_y} \right) - \frac{2\beta_x}{\epsilon_x} - \frac{\beta_y}{\epsilon_y} \\
b_{x,corrected} &= \frac{\beta_x^2}{\sigma_\delta^2 H_x \epsilon_x} - \frac{\beta_x^3 \phi_x^2}{H_x \epsilon_x^2} + \gamma^2 \left(\frac{H_x \beta_x}{\epsilon_x^2} + \frac{H_y \beta_x}{\epsilon_x \epsilon_y} + \frac{H_x \beta_y}{\epsilon_x \epsilon_y} + \frac{H_y \beta_y}{\epsilon_y^2} + \frac{\beta_x}{\sigma_\delta^2 \epsilon_x} + \frac{\beta_y}{\sigma_\delta^2 \epsilon_y} \right) + \\
&\quad \frac{\beta_x^2 \beta_y}{\gamma^2 H_x \epsilon_x \epsilon_y} - \frac{2\beta_x \beta_y}{\sigma_\delta^2 H_x \epsilon_y} + \frac{6\beta_x^2 \phi_x^2 \beta_y}{H_x \epsilon_x \epsilon_y} + \frac{2\beta_x \beta_y^2 \phi_y^2}{H_x \epsilon_y^2} + \frac{H_y \beta_x^2}{H_x \epsilon_x \epsilon_y} - \frac{2H_y \beta_x \beta_y}{H_x \epsilon_y^2} \\
&\quad + \frac{\beta_x^2}{\epsilon_x^2} - \gamma^2 \left(\frac{\beta_x^2 \phi_x^2}{\epsilon_x^2} + \frac{\beta_y^2 \phi_y^2}{\epsilon_y^2} \right) - \frac{4\beta_x \beta_y}{\epsilon_x \epsilon_y} \\
a_{y,corrected} &= \gamma^4 \left(\frac{2H_x H_y}{\epsilon_x \beta_y} + \frac{2H_y}{\sigma_\delta^2 \beta_y} + \frac{2H_y^2}{\beta_y \epsilon_y} \right) + \gamma^2 \left(-\frac{1}{\sigma_\delta^2} - \frac{H_y \beta_x}{\epsilon_x \beta_y} - \frac{H_x}{\epsilon_x} - \frac{2H_y}{\epsilon_y} + \frac{6\beta_y \phi_y^2}{\epsilon_y} \right) - \frac{\beta_x}{\epsilon_x} + \frac{2\beta_y}{\epsilon_y} \\
b_{y,corrected} &= \gamma^4 \left(\frac{H_y \beta_x}{\sigma_\delta^2 \epsilon_x \beta_y} - \frac{H_y \beta_x^2 \phi_x^2}{\epsilon_x^2 \beta_y} + \frac{H_y^2 \beta_x}{\epsilon_x \beta_y \epsilon_y} + \frac{H_x H_y \beta_x}{\epsilon_x^2 \beta_y} + \frac{H_x H_y}{\epsilon_x \epsilon_y} - \frac{H_y \beta_y \phi_y^2}{\epsilon_y^2} + \frac{H_y}{\sigma_\delta^2 \epsilon_y} + \frac{H_y^2}{\epsilon_y^2} \right) \\
&\quad + \gamma^2 \left(-\frac{2H_x \beta_x}{\epsilon_x^2} - \frac{4H_y \beta_x}{\epsilon_x \epsilon_y} + \frac{H_x \beta_y}{\epsilon_x \epsilon_y} + \frac{H_y \beta_y}{\epsilon_y^2} - \frac{2\beta_x}{\sigma_\delta^2 \epsilon_x} + \frac{2\beta_x^2 \phi_x^2}{\epsilon_x^2} + \frac{6\beta_x \beta_y \phi_y^2}{\epsilon_x \epsilon_y} + \frac{\beta_y}{\sigma_\delta^2 \epsilon_y} - \frac{\beta_y^2 \phi_y^2}{\epsilon_y^2} \right) \\
&\quad + \frac{\beta_x \beta_y}{\epsilon_x \epsilon_y} \\
b_{s,corrected} &= \gamma^2 \left(\frac{H_x \beta_x}{\epsilon_x^2} + \frac{H_y \beta_x}{\epsilon_x \epsilon_y} + \frac{H_x \beta_y}{\epsilon_x \epsilon_y} + \frac{H_y \beta_y}{\epsilon_y^2} + \frac{\beta_x}{\sigma_\delta^2 \epsilon_x} - \frac{\beta_x^2 \phi_x^2}{\epsilon_x^2} + \frac{\beta_y}{\sigma_\delta^2 \epsilon_y} - \frac{\beta_y^2 \phi_y^2}{\epsilon_y^2} \right) - \frac{2\beta_x \beta_y}{\epsilon_x \epsilon_y}
\end{aligned}$$

In figures 5.5.1 and 5.5.2 two cases are shown where I compared the beam lifetimes in the different planes calculated with the equations in [25] and with the corrected equations that are shown above. The results are not really surprising. As was assumed by many people all the deviations are within the one percent level, well below the level where it would make a significant difference for the simulations.

As one can expect from the above equations evaluating the integrals takes some time, so for particle tracking this model would be very time consuming. Instead, as I will explain in more detail in the part on simulations, we used this algorithm implemented in MAD-X to generate the growth rates on a lattice of different beam (emittances) and machine settings (RF Voltage). Using interpolation we then compared the simulations with measured data.

Part 3

Simulations

Simulations based on MAD-X

6.1. Introduction MAD-X

MAD is a terminal based software tool developed at CERN for designing accelerators and doing accelerator simulations¹. In MAD, accelerators are described as a sequence of elements (an example of a sequence file is given in appendix D.1) and as strength files containing the strength settings for the different magnets in the machine for a specific set-up (injection, collision 3.5 TeV,...). Different modules in the software then allow for studying the behavior of the machine and extract properties of the machine. For instance one can extract the Beta-Functions at a certain interval around the ring (see figure 6.1.1).

But MAD can do a lot more: it has the ability to return all sorts of data for different settings chosen by the user. This means that to run a simulation with MAD the user will have to give some settings as input for the simulation and choose what data he/she wants as output. An example of a simple MAD-X program is given in appendix D.2.

¹The X means that it is the 10th version of the software.

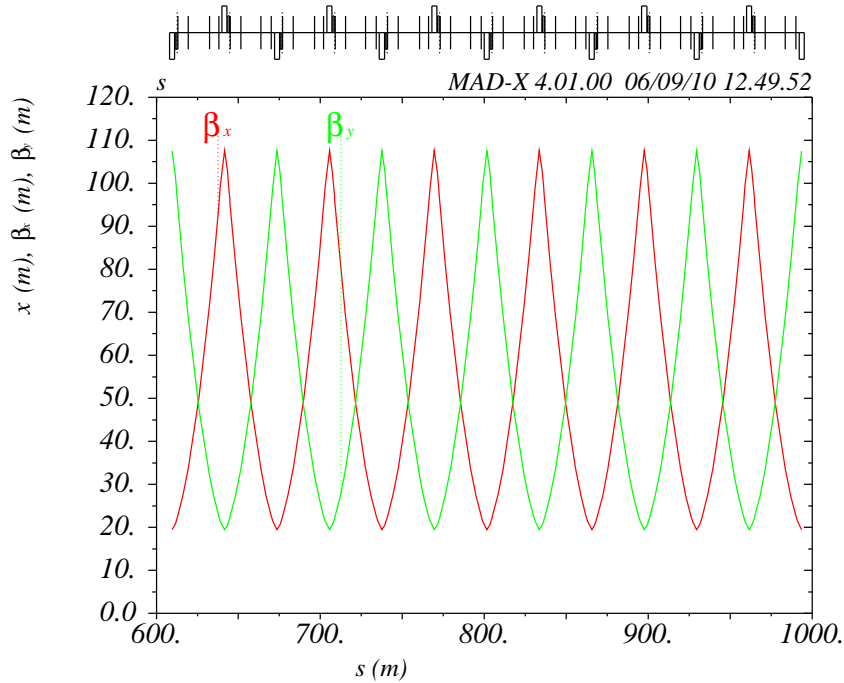


FIGURE 6.1.1. Example of output plot in MAD-X.

The input of the program consists of the sequence file of the accelerator and the settings for the beam. The output of this little program includes a file with the Optical Functions (or Twiss parameters, saved as “Twiss.out”, see appendix D.3 for a part of that file) and two plots, one plot with the Beta-Functions for the transverse planes (see figure 6.1.1) and one plot with the Dispersion Function for the horizontal plane (see figure 6.1.2). I do not wish to go deeper into the details of MAD here, because I did not use MAD in the form that was just described here, and it is not the purpose of this text to describe the MAD language and its functionality. Instead of using MAD as described in the examples in the different appendices MAD was used in a Mathematica environment as will be explained in the next section.

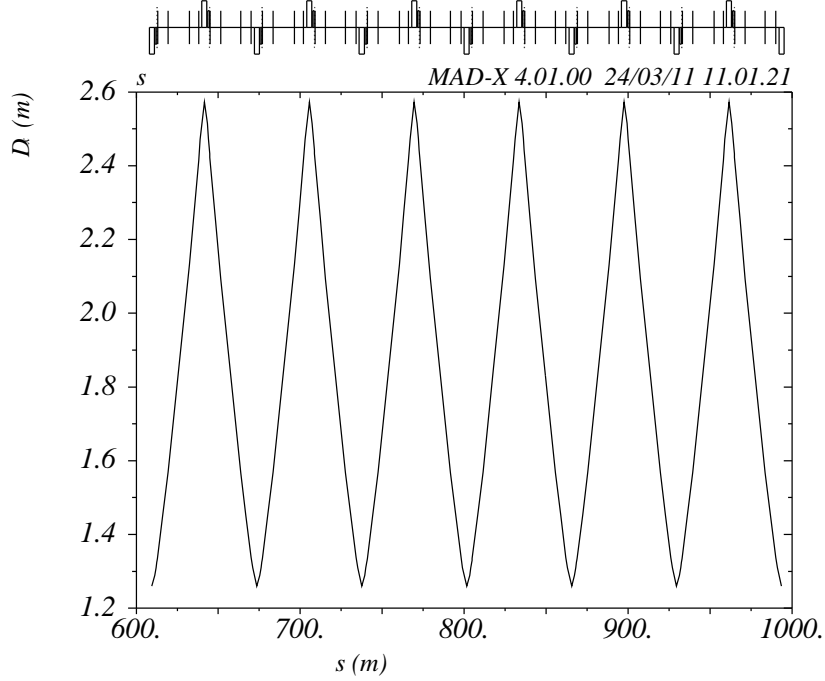


FIGURE 6.1.2. Example of output plot MAD-X of the Horizontal Dispersion Function

6.2. Mathematica and MAD-X: Madtomma

To increase functionality and simplify the user interface John Jowett (CERN) and collaborators developed a collection of Mathematica packages that allow the user to run MAD directly from within the Mathematica environment, thus giving the user the ability to apply all the functionalities available in Mathematica on the data output of the MAD software. This collection of packages is referred to as Madtomma (MAD to Mathematica). This largely increases the efficiency of the work described in this text. Using these packages the settings for the simulations can be done with a single or with a short sequence of commands in Mathematica resulting in a “*.tfs” file for each beam. These tfs files contain all the requested output for the settings that the user has given as input.

The implemented functions in these packages also allow for an easy visualization and analysis of this data. For example requesting the Beta-Functions and the Dispersion Functions at specific elements or plotting them over an interval along the ring as I did in the previous section becomes very easy and results in some very nice plots. An example of such a plot is shown in figure 6.2.1. This plot also displays, next to

the Beta-Functions and the Dispersion Functions in both planes, a graphical representation of the elements and their names over the range for which I requested the data².

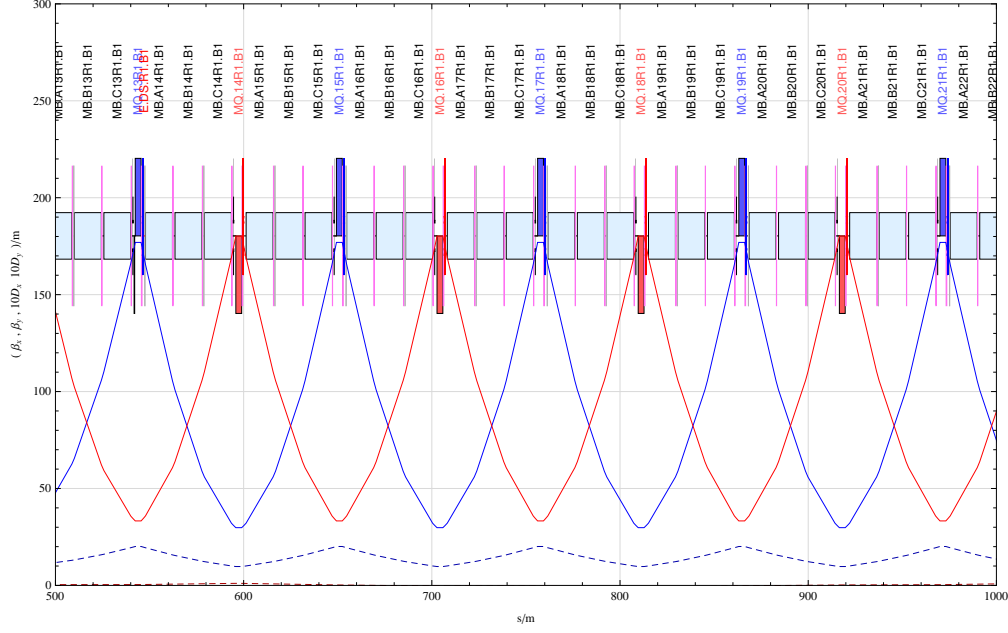


FIGURE 6.2.1. Beta-Functions with Mathematica

6.3. IBS Simulations with MAD-X

In this section I will try to give an overview of the approach we used in the early stages of my internship at CERN, when trying to simulate the IBS growth rates using MAD-X. As discussed before (see Chapter 5), MAD-X uses the model developed by Frank Zimmerman.

To do the actual simulation we used Mathematica as an interface with MAD-X using the Madtomma packages. As mentioned in the previous section MAD-X needs some input to be able to run a simulation. In our case this input consists of the RF Voltage applied in the RF-cavities and the beam parameters (see figure 6.3.1 for an example of beam settings).

Beam Parameters
SEQUENCE → LHCB1
BV → 1
ENERGY → 450.
PARTICLE → PROTON
KBUNCH → 2808
NPART → 1.15×10^{11}
EX → $7.8189334452152 \times 10^{-9}$
EY → $7.8189334452152 \times 10^{-9}$
ET → 0.00005355
SIGE → 0.000306
SIGT → 0.175

FIGURE 6.3.1. Beam Parameters

²The light blue boxes represent the main bending magnets, the blue boxes represent focusing (in the horizontal plane for beam 1) quadrupoles and the red boxes represent defocusing (in the horizontal plane for beam 1) quadrupoles.

These are a lot of parameters to play with, but we are only interested in some of them. The total number of bunches (“KBUNCH”) in a beam is not very important for now, since the formulas for calculating the growth rates are for a single bunch in a bunched beam and MAD-X assumes then that all the bunches have the same initial settings. A question that immediately emerges here is of course what happens if the bunches do not have the same initial settings. One could in principle solve this by extracting the initial data for a specific bunch and simulate this specific bunch, but unfortunately extracting bunch specific data is not that straightforward since the LHC and its instrumentation are still under commissioning (see also section 6.4). At this stage I did not have the knowledge yet to access this bunch specific data so we used averages over all the bunches at that time. By the time this individual bunch data became available and I developed the skills to extract this data we had already changed to the particle tracking simulation codes. So for comparison of simulations with individual bunch data I refer the reader to the particle tracking simulations further in this text (see Chapter 7) .

Another parameter that is not that relevant in these simulations is the number of particles in each bunch of the beam (“NPART”) . The reason for this is that the IBS lifetimes τ scale with the inverse of the intensities, so once we have a simulation result for a particular number of particles in a bunch (I_0) we just need to apply a rescaling as shown in equation 6.3.1 to have the lifetimes for a bunch with a different number of particles (I).

$$(6.3.1) \quad \tau(I) = \tau(I_0) \frac{I_0}{I}.$$

Because of the current limitations set on the LHC with respect to the beam energies used the simulations were restricted to injection energy (450 GeV) and top energy at the time of writing (3.5 TeV).

In my first simulations round beams were assumed, meaning that the emittance in the horizontal and vertical plane (ϵ_x, ϵ_y) are assumed to be the same. Later, in the particle tracking simulations, this assumption was relaxed to incorporate non-round beams.

The list of parameters and ranges we used for protons and ions in the simulations with MAD-X are summarized in table 1 (emittances are normalized³).

Parameter	Range
RF Voltage	1 – 16 Mega Volt
ϵ_x	2.0 – 4.0 $\mu\text{m rad}$ (0.2 – 3.2 μmrad for ions)
ϵ_y	2.0 – 4.0 $\mu\text{m rad}$ (0.2 – 3.2 μmrad for ions)
ϵ_s	0.5 – 2.5 eVs (0.3 – 4.5 eVs for ions)
Energy	450/3500 GeV

TABLE 1. Simulations Parameters

Under the assumption of round beams this reduces to a three-dimensional lattice at a certain energy. The results of these simulations are a set of three lifetimes⁴ (Horizontal, Vertical and Longitudinal) in each lattice point. In figure 6.3.2 we show the lifetimes for protons and ions at an energy of 3.5 TeV in function of the longitudinal and transverse emittances for a fixed RF voltage of 8 Mega Volt (the growth rates are then the reciprocals of these lifetimes). Notice the large difference between the horizontal and vertical lifetimes. One can immediately see that the expected IBS lifetimes for ions are smaller than for protons when using the same settings, which means that we expect the ion fills to be shorter than the proton ones. Using these data sets we created interpolating functions for the lifetimes over the lattice that were then used to compare

³The different choices for the emittances for protons and ions come from the differences in expected/measured injection conditions for the beam and the difference in the relativistic gamma factor for both particle species (3730.26 for protons at 3.5 TeV and 1481.7 for ions at 3.5 TeV equivalence) giving rise to different normalized emittances for the same geometric emittances. Where the geometric emittances are the non-normalized emittances.

⁴Running these simulations is quite time consuming. This particular simulation needed about ten hours to complete.

the simulations with the data extracted from the LHC Logging Database, where the measured data for the different fills⁵ is stored.

6.4. Data Extraction from Measurement Devices and related issues

As in any physics experiment, data from a measurement always comes with some issues (accuracy, calibration, errors,...) that are sometimes difficult to resolve. In this section I will go through some of the issues that I encountered when working with measured data.

In the previous section I already mentioned that the simulations software needs some input parameters, the initial beam conditions. This means that we already need some initial data to put in the simulations. Note that we are not trying to simulate the initial conditions here but we are trying to simulate the changes over time of some of the beam parameters starting from some known initial conditions.

The most relevant input parameters to discuss with respect to measured data here are the emittances and the bunch lengths, so I will go through some of the issues related to extracting and interpreting this data. In the LHC the emittances are not measured directly but are derived from the beam sigmas by use of the equation $\epsilon_N = \gamma \frac{\sigma_\beta^2}{\beta}$.

The bunch length data was collected from the Beam Quality Monitors (BQM) and from the ATLAS Luminous Region data. The BQM basically measures the four sigma bunch length in seconds, to get the actual bunch length this data needs to be multiplied by the speed of light and divided by four. The BQM data is very handy because it logs the bunch length for all the bunches in the accelerator, and it even keeps data for all the 3564 slots in the beam (the slots correspond to the locations in the RF fields along the ring where a bunch can occur). What is less handy about this is that it is a large matrix of data when longer time intervals are considered, immediately introducing the associated memory problems that come with this fact. To deal with these memory problems I used different approaches to extract and load the data. A discussion of these different approaches would lead me too far so I will not discuss them further.

The ATLAS Luminous Region data does not have this feature but averages over all the colliding bunches at the ATLAS interaction point. The Luminous Region data is also a little bit more complicated to understand because it convolutes the bunch lengths ($\Sigma_s = \sqrt{\sigma_{s1}^2 + \sigma_{s2}^2}$, where Σ_s is the longitudinal luminous vertex size) of the colliding beams, which makes it impossible to extract the bunch lengths for each beam separately. The Luminous Region data is acquired by the ATLAS detector and comes down to a measurement of the luminous vertex size in the detector. A discussion of Luminous Region measurements falls outside of the scope of this text, but a discussion of this subject can be found in [22].

The essential point for the longitudinal Luminous Region data is that one needs to divide the recorded sigmas by the square root of two (with the assumption that the bunches in both beams have the same bunch length). In comparing the bunch length data from ATLAS with the BQM I found that they agree within reasonable limits, from which I decided to continue working with the BQM data for further analysis. An example of the comparison of the two data sets is shown in figure 6.4.1.

For the transverse emittances I used four different measurement devices. The first device is called a wire scanner, which is basically a wire that is moved through the beam, in this way acquiring the beam profile. Different wire scanners are used in both planes. The wire scanners are believed to be the most reliable devices and are often used to cross calibrate the devices that I will discuss in a moment. A big disadvantage of the wire scanners is that they can only be used at low energy and with low beam intensities, because otherwise the wire is destroyed by the beam. I mainly used this data to cross-check the data from the other devices and also at injection where almost no other data is available.

The second device I used was the Beam Gas Injection detectors (BGI), which are based on beam particles scattering off on gas molecules that are injected in the beam pipe. Unfortunately these detectors are not

⁵A fill is a designation used in accelerator physics to refer to a specific time window in the machine. Usually this window starts on injection of the first particles (filling) in the machine and ends after the beam dump and ramp down of the magnets. So the machine operation consists of these fills intermediated with technical stops, machine cycling (resetting for the next fill), etc.. Some fills are specifically dedicated to machine or instrumentation studies in opposition to the physics fills. The physics fills are the ones we studied here.

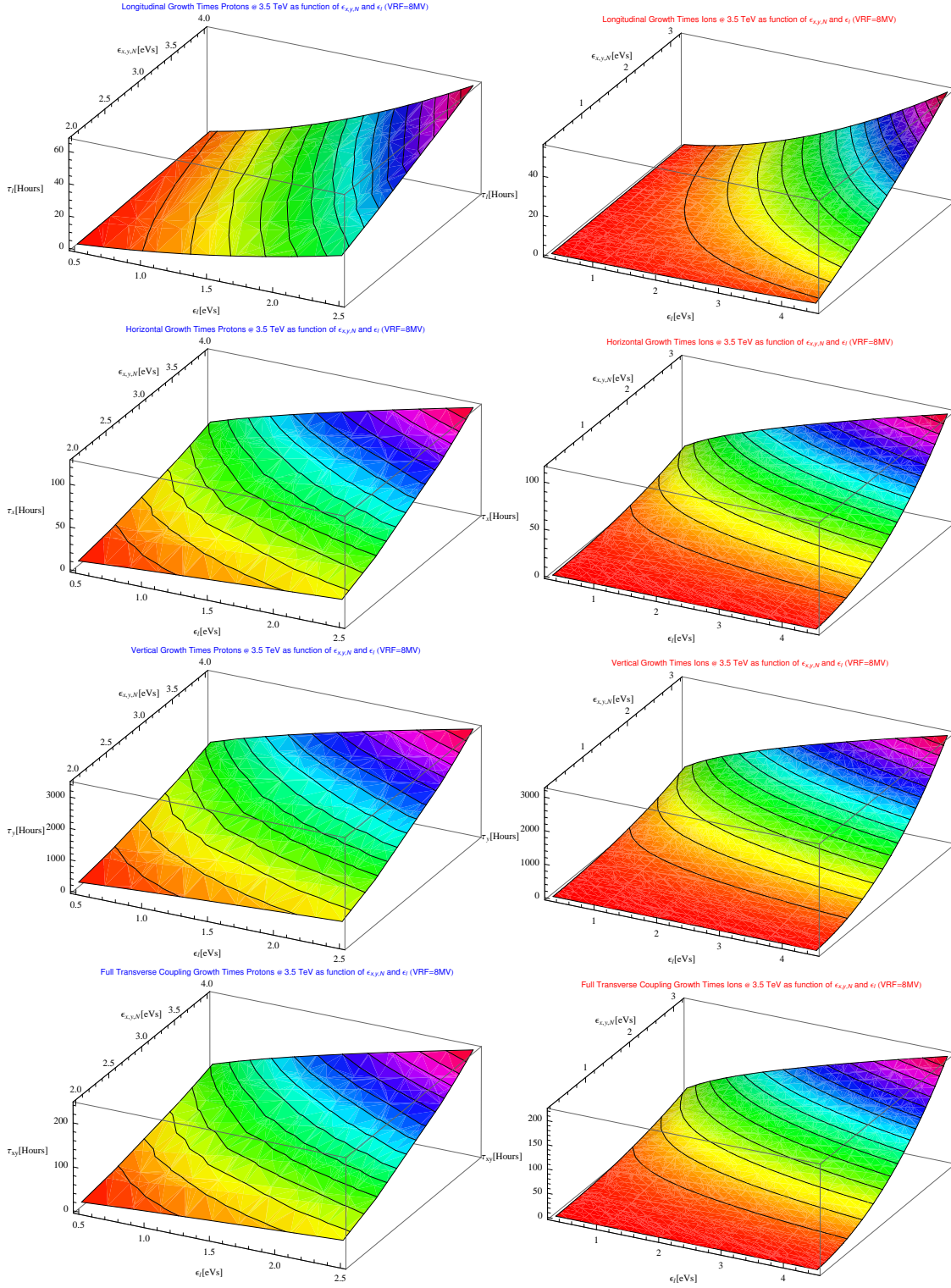


FIGURE 6.3.2. Lifetimes for Protons and Ions for VRF = 8 Mega Volt @ 3.5 TeV

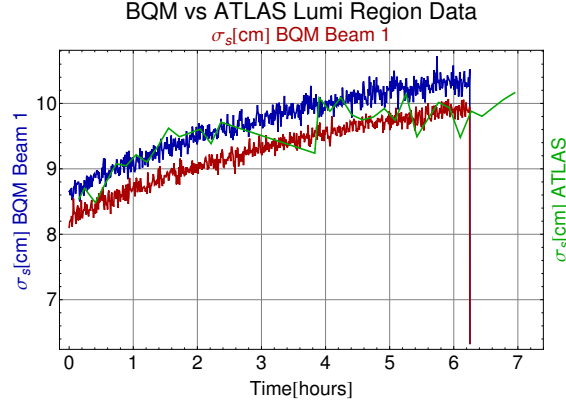


FIGURE 6.4.1. BQM vs ATLAS Luminous Region Data

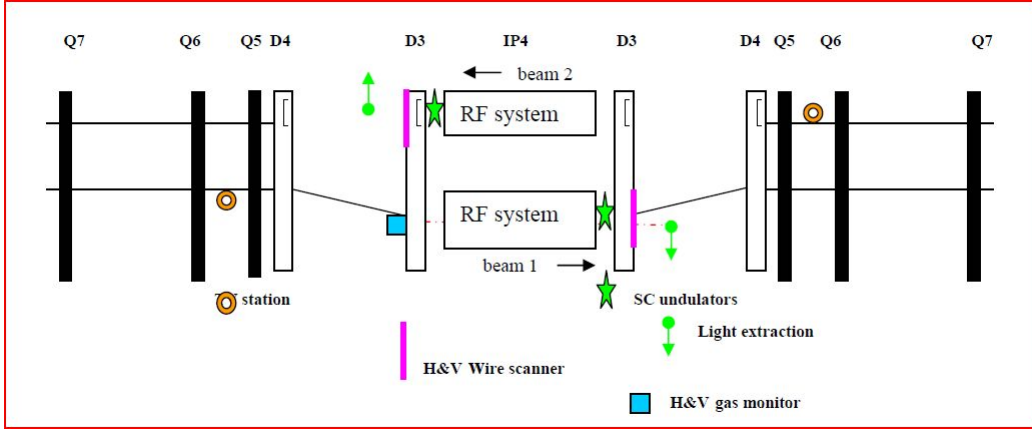


FIGURE 6.4.2. BSRTS Layout (source: chapter 13 in [2])

well calibrated yet (factors two of difference with the other devices can be found and expected) and still under comissioning. This of course strongly limits the use of this device for the simulations.

As a third device I used the ATLAS Luminous Region data for the transverse planes. Again here the same remark as for the bunch length measurements, both beam sizes are convoluted so here also no separate data for the individual beams. The convolution is done according to equation 6.4.1

$$(6.4.1) \quad \sigma_{L,x,y} = \frac{1}{\sqrt{\frac{1}{\sigma_{x,y,1}^2} + \frac{1}{\sigma_{x,y,2}^2}}},$$

which means that under the assumption of equal beam size for both beams, the Luminous Region beam sigma data for the transverse planes needs to be multiplied with a factor $\sqrt{2}$. Note that the Luminous Region data averages over all the colliding bunches, just as for the bunch lengths.

As a fourth and final device I used the Beam Synchrotron Light Monitors (BSRTS). The BSRTS are the most complex data sets I used. To explain how I used them I need to go a little bit deeper into how they work.

In figure 6.4.2 a schematic layout of the synchrotron monitors at IP4 is shown. At low energy (injection) the particles are steered over a superconducting undulator (the green stars in figure 6.4.2) that makes the beam oscillate and makes the particles in the beam send out synchrotron light. This light is then extracted from the beam pipe and focused by a set of mirrors with energy dependent settings (they are moved into place by a set of motors). This focused synchrotron light is then captured by a camera that can be compared

Ions		450 GeV	3500 GeV
B1	H	0.60	0.40
	V	0.99	0.65
B2	H	0.60	0.55
	V	0.50	0.40

FIGURE 6.4.3. Correction factors

with a usual CCD camera. From the synchrotron light spot size on the CCD chip the beam sigmas are then derived. At collision energy the bending of the beam in the D3 dipole magnets (beam separation magnets to the left and to the right of IP4, see figure 6.4.2) is sufficient to create synchrotron light.

I hope this makes it clear that calibrating this system or making an estimate of the absolute accuracy of this data is far from simple or straightforward. During my internship I received different sets of correcting factors to apply to the data by using the formula $\sigma_{corrected} = \sqrt{\sigma_{meas}^2 - \sigma_{corr\ factor}^2}$. Figure 6.4.3 shows the different correcting factors [7] I used to get initial data for the simulations and later to compare the simulations with the data for the Ion run in 2010.

But why do I choose to rely on such a complex measurement device? The advantage of the BSRTS is that during the 2010 runs this was the only device, as far as I know, that was able to log individual bunch data for the transverse planes. Since the simulation software (MAD-X and particle tracking) simulates essentially a single bunch, this becomes valuable data to compare with the simulations. But extracting the individual bunch data is also not as straightforward as one would expect. Before explaining the algorithm I used to separate the data for the individual bunches from the complete data set, I need to mention that there is another variable stored in the Logging Database that is related to the BSRTS.

This variable stores the data acquisition gate delays of the BSRTS. Without going any further into the electronic implementation of this system this variable tells the BSRTS when and how long they have to log data with respect to the beam turn clock (a kind of synchronizing clock for the whole machine). The Gate Delays are expressed in units of 0.2 times the number of the RF bucket along the ring with respect to the location of the detector. So it is in this variable that the information is stored about which bunch is being sampled and for how long it is being sampled. Figure 6.4.4 shows an example of this gate delay data for both beams: notice that it takes some time to scan through all the bunches, which translates into a low number of data points for the entire fill. A future goal is to have a periodic scheme to sample through the bunches, but in the 2010 runs this was not implemented yet and often the gate delays were set manually by an operator in the control room making it a “bit” harder to figure out which data point belongs to which bunch. By relating the intervals of the settings of the gate delays with the BSRTS measured data I was able to extract bunch by bunch data. Figure 6.4.5 shows the Mathematica implementation of this algorithm⁶.

The four devices I described above return data for the beam sigmas but not for the emittances. To get the emittances the values of the Beta-Functions at the locations of the measurement devices are needed. This means that an optics calculation with Madtomma is needed to determine them (they are returned in the tfs files mentioned before). Again here the BSRTS need some special attention because the synchrotron light is not created at the BSRTS devices, but at the locations of the D3 magnets or the superconducting

⁶I implemented this function in a Mathematica Package building on the LHCMD package developed by John Jowett (CERN) and on the LoggedServiceUtils Package developed by Heiko Damerau (CERN) in an attempt to automate some of the data-extraction and analysis.

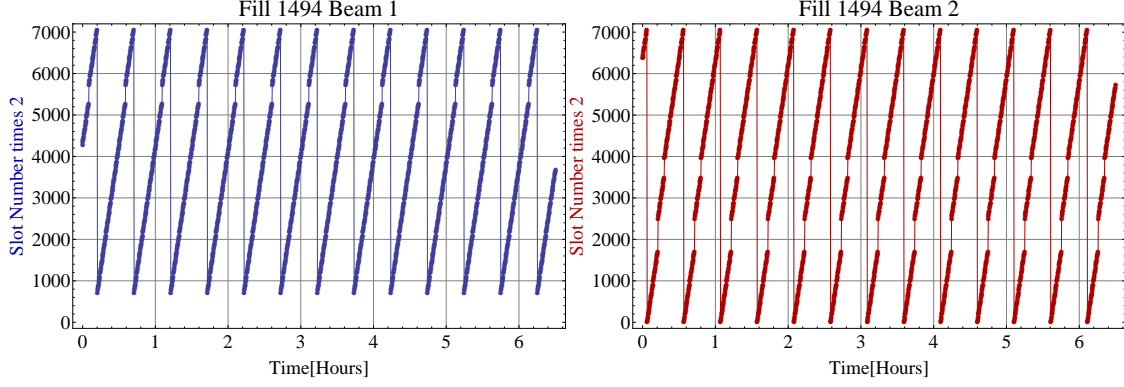


FIGURE 6.4.4. Example of Gate Delay Data (Fill 1494)

```

GD = Transpose[{(Drop[LHCBSRCTLgd[start, stop, beam], 1][[All, 1]] - (start + 3600 * ($TimeZone - 1))) / 3600,
  Drop[LHCBSRCTLgd[start, stop, beam], 1][[All, 2]]];
(*try making faster with {(#1-start)/3600, #2}&/@Drop[LHCBSRCTLgd[start, stop, beam], 1]*)
GDI = Flatten /@ Transpose[{GD, RotateLeft[GD][[All, 1]]];
bsrts = LHCBGIBSRTS[start, stop, Device -> "BSRTS", Beam -> beam, Plane -> "x", BSRTSCorrections -> optsBSRTSCorrections,
  tfsFile -> optstfsFile];
f[t1_, t2_] := Select[bsrts, t1 < #[[1]] < t2 &];
datax = Mean /@ Drop[Map[f[#[[1]], #[[3]]] &, GDI], 1];
sigmax = Table[Table[datax[[j + i]], {j, 0, Length[datax] - nobunch, nobunch}], {i, 1, nobunch}];
bsrts = LHCBGIBSRTS[start, stop, Device -> "BSRTS", Beam -> beam, Plane -> "y", BSRTSCorrections -> optsBSRTSCorrections,
  tfsFile -> optstfsFile];
f[t1_, t2_] := Select[bsrts, t1 < #[[1]] < t2 &];
datay = Mean /@ Drop[Map[f[#[[1]], #[[3]]] &, GDI], 1];
sigmay = Table[Table[datay[[j + i]], {j, 0, Length[datay] - nobunch, nobunch}], {i, 1, nobunch}];
If[beam === 1,
  rotate = If[GD[[1, 2]] < 713, Round[(GD[[1, 2]] - 713) / 2] + 3564, Round[(GD[[1, 2]] - 713) / 2]];
  {Delete[RotateLeft[sigmax, Position[LHCBCFTRPositionBunches[fillnumber, beam], rotate][[1, 1]] - 1],
  Position[RotateLeft[sigmax, Position[LHCBCFTRPositionBunches[fillnumber, beam], rotate][[1, 1]] - 1], Mean[{}]]],
  Delete[RotateLeft[sigmay, Position[LHCBCFTRPositionBunches[fillnumber, beam], rotate][[1, 1]] - 1],
  Position[RotateLeft[sigmay, Position[LHCBCFTRPositionBunches[fillnumber, beam], rotate][[1, 1]] - 1], Mean[{}]]],
  ,
  If[beam === 2,
    rotate = If[GD[[1, 2]] < 2498, Round[(GD[[1, 2]] - 2498) / 2] + 3564, Round[(GD[[1, 2]] - 2498) / 2]];
    {Delete[RotateLeft[sigmax, Position[Flatten[LHCBCFTRPositionBunches[fillnumber, beam], rotate][[1, 1]] - 1],
    Position[RotateLeft[sigmax, Position[Flatten[LHCBCFTRPositionBunches[fillnumber, beam], rotate][[1, 1]] - 1], Mean[{}]]],
    Delete[RotateLeft[sigmay, Position[Flatten[LHCBCFTRPositionBunches[fillnumber, beam], rotate][[1, 1]] - 1],
    Position[RotateLeft[sigmay, Position[Flatten[LHCBCFTRPositionBunches[fillnumber, beam], rotate][[1, 1]] - 1], Mean[{}]]],
    , LHCBSRTsbunchdata::invalid_beam = "Invalid beam number";
    Message[LHCBSRTsbunchdata::invalid_beam]
  ]

```

FIGURE 6.4.5. Decomposing the BSRTS data in individual bunch data

undulators depending on the energy. One needs to be careful to use the correct Beta-Function values for the different cases.

In comparing the data to the simulations I noticed that BSRTS data and ATLAS Luminous Region data do not fully agree with each other. I wanted to quantify the difference and check if there is a certain structure in this difference or not. To check this I convoluted the data of the BSRTS according to equation 6.4.2

$$(6.4.2) \quad \sigma_L = \frac{\sqrt{\beta_L}}{\sqrt{\frac{\beta_1}{\sigma_1^2} + \frac{\beta_2}{\sigma_2^2}}},$$

to see what values would come out for the Luminous Region vertex size using beam sizes based on the BSRTS data. I then compared the calculated luminous region sigmas with the ones logged by ATLAS. Figure 6.4.6

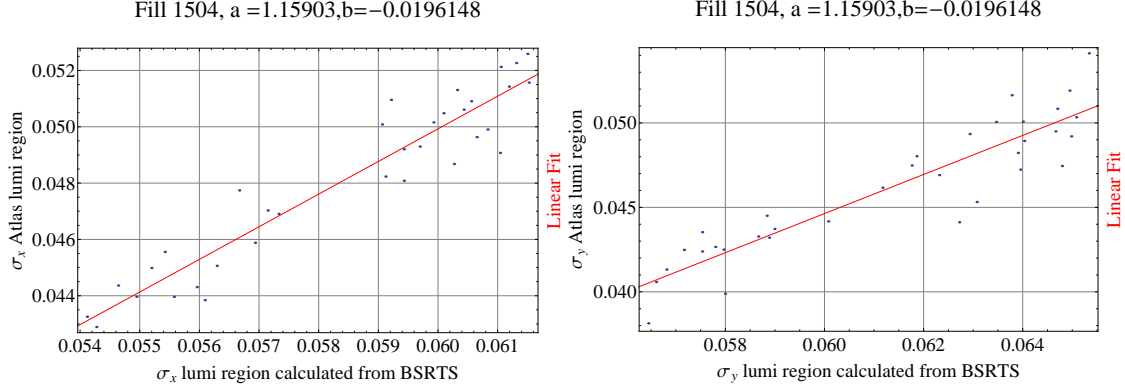


FIGURE 6.4.6. Example of ATLAS Luminous Region Data vs BSRTS calculated Luminous Region Data

Fill	a_x	b_x	a_y	b_y
1494	0.992736	-0.00597806	0.351937	0.0387482
1496	1.01073	-0.00674657	0.694422	0.00942032
1504	1.15903	-0.0196148	1.15718	-0.0247983
1505	1.42408	-0.0309851	0.0464273	0.0403765
1511	0.785287	0.0126304	1.18032	-0.0241121
1514	0.622468	0.0216643	1.07265	-0.0213164
1520	0.64778	0.0197748	-0.0281858	0.0485419
1532	1.03444	-0.0109959	1.42622	-0.0406114
1533	0.62633	0.0136882	0.295226	0.0341639
1534	1.09509	-0.0125012	1.10934	-0.0142333
1535	1.38129	-0.0245967	0.765086	0.00888326
1536	2.52545	-0.135958	0.852634	-0.0195738
1540	-0.170953	0.0551481	-0.135298	0.0694247

FIGURE 6.4.7. Linear Fit Parameters for Lumi Region

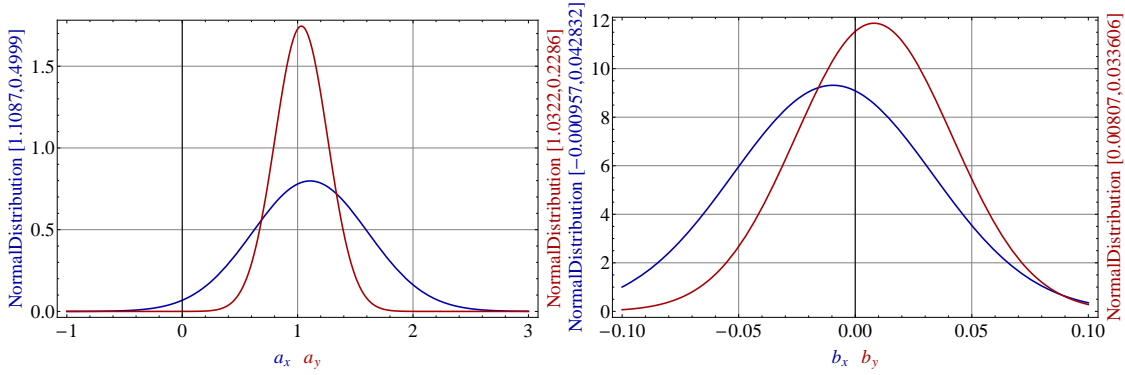


FIGURE 6.4.8. Gaussian Fits for the Linear Fit parameters

shows such a comparison for fill 1504 together with a linear model fit $\sigma_{L,ATLAS} = (a\sigma_{L,BSRTS} + b)$. Figure 6.4.7 shows the values of the linear model fit parameters for both planes for all the Ion Fills from 2010 that had sufficient data to do this analysis. Some values deviate strongly because the BSRTS device was not working properly or some changes in the settings were made during the fill. I selected some of these parameters to fit them with a Gaussian, and the results of these fits are shown in figure 6.4.8. As will become clear further in this text, one has to be careful in considering the absolute values of the BSRTS.

6.5. Comparing the simulations with data

There are several ways in which the data can be compared with the simulations. As I accumulated knowledge and insight into the used analysis techniques, data and measurement devices, it was necessary to adapt my methods of comparison. In the following sections I will go through the different approaches used for the simulations using the created interpolating functions based on the IBS lifetimes output of MAD-X.

6.5.1. Comparing Lifetimes. One possible approach is to make use of equation (6.5.1) to calculate the lifetimes of the data and compare these with the simulated lifetimes. The procedure used to do this can be summarized in the following steps:

- (1) Download the logged data, smoothen the data (beam sigmas $\sigma_x, \sigma_y, \sigma_s$) and create an interpolating function for the smooth data.⁷
- (2) Calculate $\frac{1}{\sigma} \frac{d\sigma}{dt}$ using equation (6.5.1) for the derivative at a number of points (taking a factor of two into account when comparing lifetimes to the emittance lifetimes⁸).
- (3) Use the data to determine the emittances and average intensities (giving the average number of particles per bunch⁹) at the points mentioned in (2) and extract the used RF voltage from the logged data.
- (4) Use the interpolation functions to calculate the lifetimes at the points from (2) using the data from (3) as input for the interpolation functions.
- (5) Compare the lifetimes calculated from the data with the ones calculated from the IBS interpolation functions.

$$(6.5.1) \quad \frac{df(t)}{dt} = \frac{f(t_2) - f(t_1)}{t_2 - t_1}$$

As an example I show the horizontal and vertical beam sigmas (σ_x, σ_y) measured by the Synchrotron Light Monitors (BSRTS¹⁰) for beam 1 before and after smoothing both for protons (Figure 6.5.1) and for ions (Figure 6.5.2).

At the time of these first comparisons I was not aware of the fact that the BSRTS devices scan through the different bunches in the beam, either manually by intervention of an instrument operator or automatically using a gate delay for the data acquisition. Due to the individual differences between the bunches, a strong averaging over somewhat lengthy periods of time was needed to have a more or less smooth curve for the data. This effect can clearly be seen for ions in figure 6.5.2, where even after extensive smoothing the scanning through the bunches is still observable.

The fact that this effect is more clear for ions is actually a consequence of IBS. As one can see in figure 6.3.2, the lifetimes for ions are shorter than the lifetimes for protons, showing that the IBS effect is stronger for ions than for protons. This means that individual ion bunches will experience a faster emittance (beam size) blow-up than bunches with protons would experience.

In the LHC the bunches are not injected all at the same time, so bunches that are injected first can grow under influence of IBS while the other bunches are being injected. This results in a larger spread in the emittances for the individual bunches for ions than for protons. The oscillations seen in the curves in the bottom plot of figure 6.5.2 are caused by this effect. To solve this averaging problem bunch by bunch data is needed.

This bunch by bunch data became available to me when I learned how to extract individual bunch data from the BSRTS and after the device was adequately commissioned for delivering bunch by bunch data (for the longitudinal plane, bunch by bunch data was already available in the logging database from the BQM) allowing me to compare the data for a single bunch with the simulation.

⁷I used the MovingAverage and Interpolation command in Mathematica for doing the smoothing of the data and creating the interpolation functions. The interpolating functions are needed because the sampling rates and times are not identical for the different data sets. So if we want to compare different data at a certain point in time, this data might not be available at that specific time due to this difference in sampling. To estimate “missing” data at that time point I used the standard interpolation function that is implemented in Mathematica (Interpolation[data set]).

⁸This comes from $\frac{d\sigma}{\sigma dt} = \frac{1}{2} \frac{d\epsilon}{\epsilon dt}$.

⁹Once we know this average, rescaling the lifetimes is possible by use of equation 6.3.1.

¹⁰Corrected according the procedure outlined in [7]

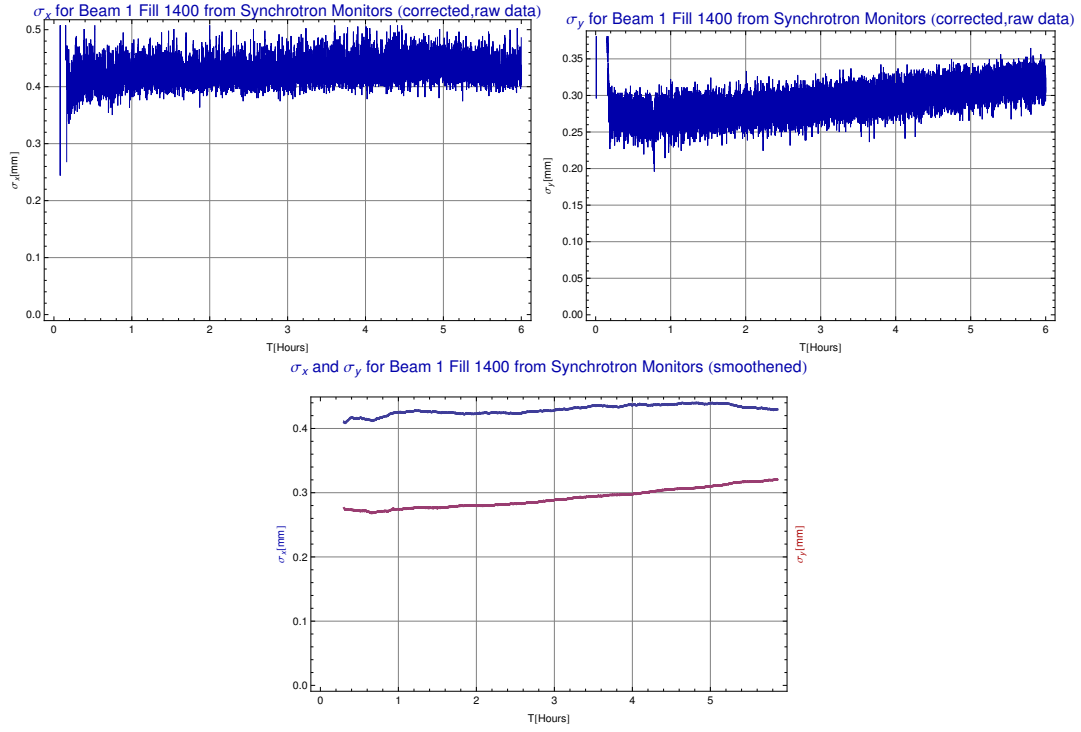


FIGURE 6.5.1. BSRTS raw and smoothed data for proton fill 1400

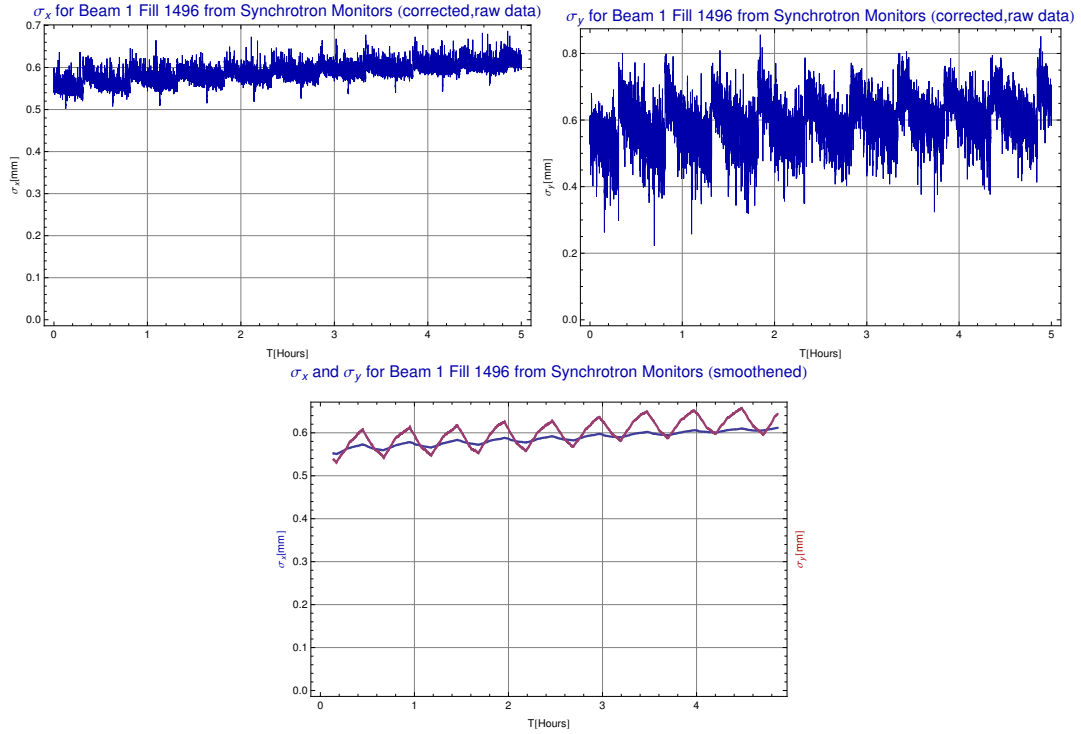


FIGURE 6.5.2. BSRTS raw and smoothed data for ion fill 1496

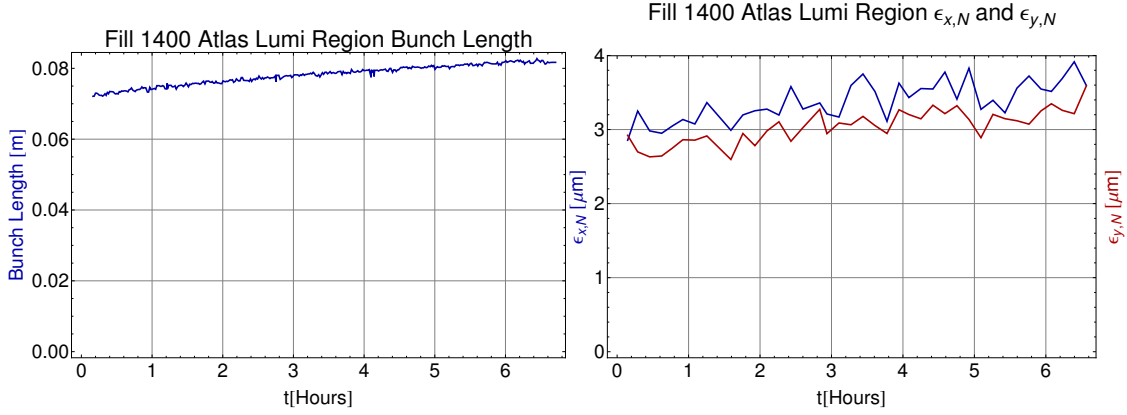


FIGURE 6.5.3. Atlas Luminous Region Data for proton fill 1400

Since at the time of this first comparison of lifetimes the individual bunch data was not yet available Atlas Luminous Region data was used for the emittances in this approach, which averages over the bunches and convolutes the values for both beams as discussed before. The raw Luminous Region data for proton fill 1400 is shown in figure 6.5.3 as an example. Figure 6.5.4 shows the results using the procedure outlined above for proton fills 1400 and 1440. Some of these plots were published in the Evian Conference Proceedings [8]. The blue curves are IBS simulations where I used emittances calculated from Atlas Luminosity and beam intensities data, by use of equation (6.5.2), as input in the IBS interpolating functions for calculating the lifetimes.

$$(6.5.2) \quad \epsilon_{xy,N}(t) = \frac{\gamma I_1(t) I_2(t) k_c f}{4\pi \beta^* L(t) k_{b1} k_{b2}},$$

where γ is the relativistic gamma factor, $f = 11245$ Hz is the particle revolution frequency in the machine, $L(t)$ is the luminosity measured by the Atlas detector in function of time, $\beta^* = 3.5$ m is the value of the β -function at the Atlas interaction point, k_c is the number of colliding bunches at Atlas, (k_{b1}, k_{b2}) are the respective number of bunches in beam 1 and beam 2 and $(I_1(t), I_2(t))$ are the respective intensities of beam 1 and beam 2 in function of time.

The red curves are IBS simulations where I used the emittances from the Atlas Luminous Region data as input for the interpolation functions. Both simulations assume round beams. The yellow curves are the lifetimes calculated from the Atlas Luminous Region data for the longitudinal and transverse emittance by use of equation (6.5.1). Figure 6.5.5 shows the results for ion fills 1496, 1504 and 1511.

From the plots for protons one would be compelled to conclude that the used model for IBS is not sufficient to explain the beam lifetimes in the transverse planes, while in the ion plots the agreement seems to be much better. The method described above is clearly highly susceptible to errors and to the method of smoothing the data. In equation (6.5.1) we divided two small numbers, giving rise to the effects that can be seen in figure 6.5.5 where there are violent changes in the lifetimes calculated from the data. At least for ions the model seems to look promising.

6.5.2. Comparing Emittances. Another, more reliable, approach is to calculate the emittances from the beam sigma data and compare the growth of these emittances with simulations. In this simulation I again make use of the IBS interpolation functions created using MAD-X but in a different way than in the approach described in subsection 6.5.1. The procedure used here can be written as

- (1) Use measured data to decide on some initial values of the input parameters for the simulation.
- (2) Create a function that uses as input the emittances, a point in time and interpolating functions for the beam intensity constructed by taking the average over all the bunches using data from the FBCT (Fast Beam Current Transformers, a device that measures the intensities of the individual bunches. For ions this measured data has to be divided by 82 because the FBCT measures charges

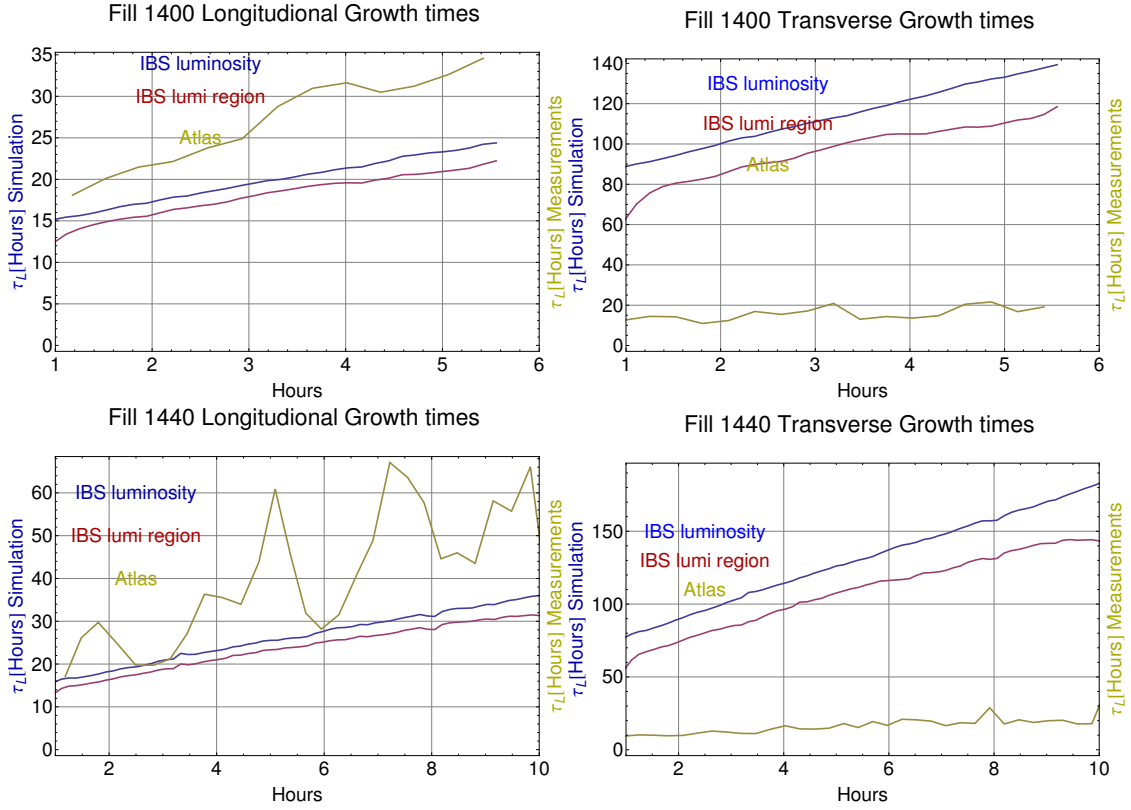


FIGURE 6.5.4. Comparing Lifetimes for proton fills 1400 and 1440 [8]

in the bunches and the Lead nuclei have a charge of 82+ in the LHC). The function returns new updated values for the emittances and a new time point according to equation (6.5.3)

$$(6.5.3) \quad f(\epsilon_{xy}, \epsilon_l, t) = \left(\epsilon_{xy} \exp \left[\frac{t}{\left(\frac{I[t]}{I_{sim}} \tau_{xy} \right)} \right], \epsilon_l \exp \left[\frac{t}{\left(\frac{I[t]}{I_{sim}} \tau_l \right)} \right], t + \frac{100}{3600} \right).$$

The function makes the emittances grow for a hundred seconds (hence $t + \frac{100}{3600}$) using the lifetimes calculated at the input values for the emittances (rescaled to the measured intensities with respect to the intensities assumed in the simulation, calculated at the input values for the emittances).

- (3) Use the initial data from measurements in the function described in equation (6.5.3).
- (4) Evaluate this function on itself for a number of times to simulate the emittance growths (I used the NestList command in Mathematica to accomplish this).
- (5) Compare the resulting data set from (4) with measurements.

The results of this approach for protons are shown in figure 6.5.6 for fill 1400 and in figure 6.5.7 for fill 1440. Results for ions are shown in figure 6.5.8 for fill 1496, in figure 6.5.9 for fill 1504 and in figure 6.5.10 for fill 1511. Again some of these plots have been published in [8]

6.6. Conclusions

The top left plots in figures 6.5.6, 6.5.7, 6.5.8, 6.5.9 and 6.5.10 seem to indicate that the used model for IBS in MAD-X overestimate the bunch growths in the longitudinal plane, while the plots on the second and third row indicate an underestimation of the transverse bunch growths. The top right plots in figures 6.5.6, 6.5.7, 6.5.8, 6.5.9 and 6.5.10 show that I can more or less force the simulated longitudinal growths to correspond better with the measured one by increasing the transverse initial emittances used, while if I want

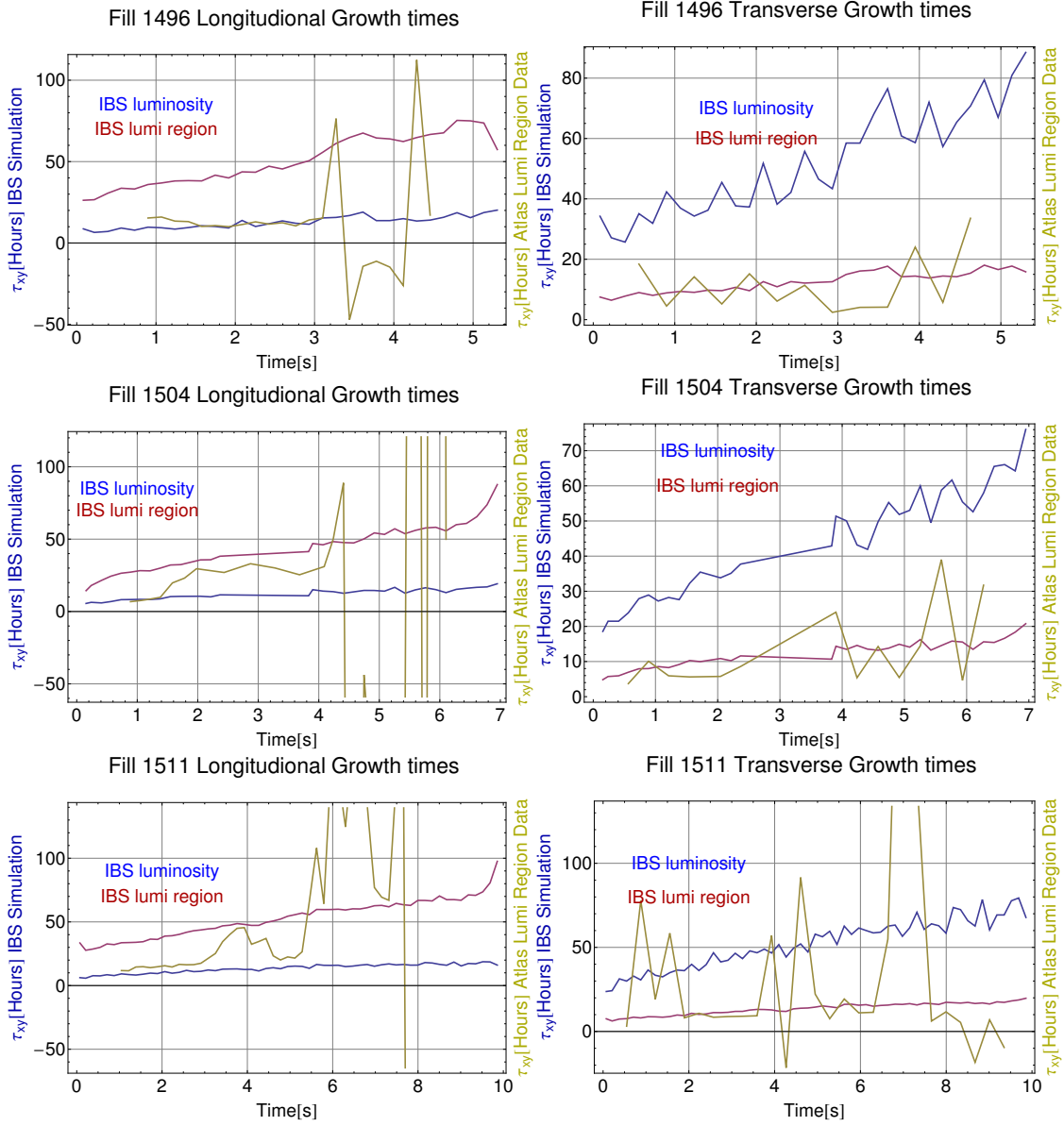


FIGURE 6.5.5. Comparing Lifetimes for ion fills 1496,1504 and 1511 [8]

to do the same for the transverse growths I need to strongly decrease the initial longitudinal emittances. The decrease of the initial longitudinal emittances needed is so strong that it reaches unrealistic levels, while the increase in the initial transverse emittances would still be acceptable. Under the assumption that the longitudinal data would be correct the question then arises if we can trust our model or if maybe the transverse data is not accurate. It would be easy to say that there is something wrong with the model, for sure in the simplified simulations of the previous sections where I didn't take radiation damping and losses or blow-up due to collisions at the interaction points (ATLAS,CMS,...) into account. But as will become clear in the section on particle tracking simulations, where collisions and radiation damping are taken into account, the same phenomenon appears.

On the other hand there is an unexplained phenomenon observed in the LHC, which is referred to as "THE HUMP", this hump blows up the transverse emittance in beam 2, especially in the vertical plane.

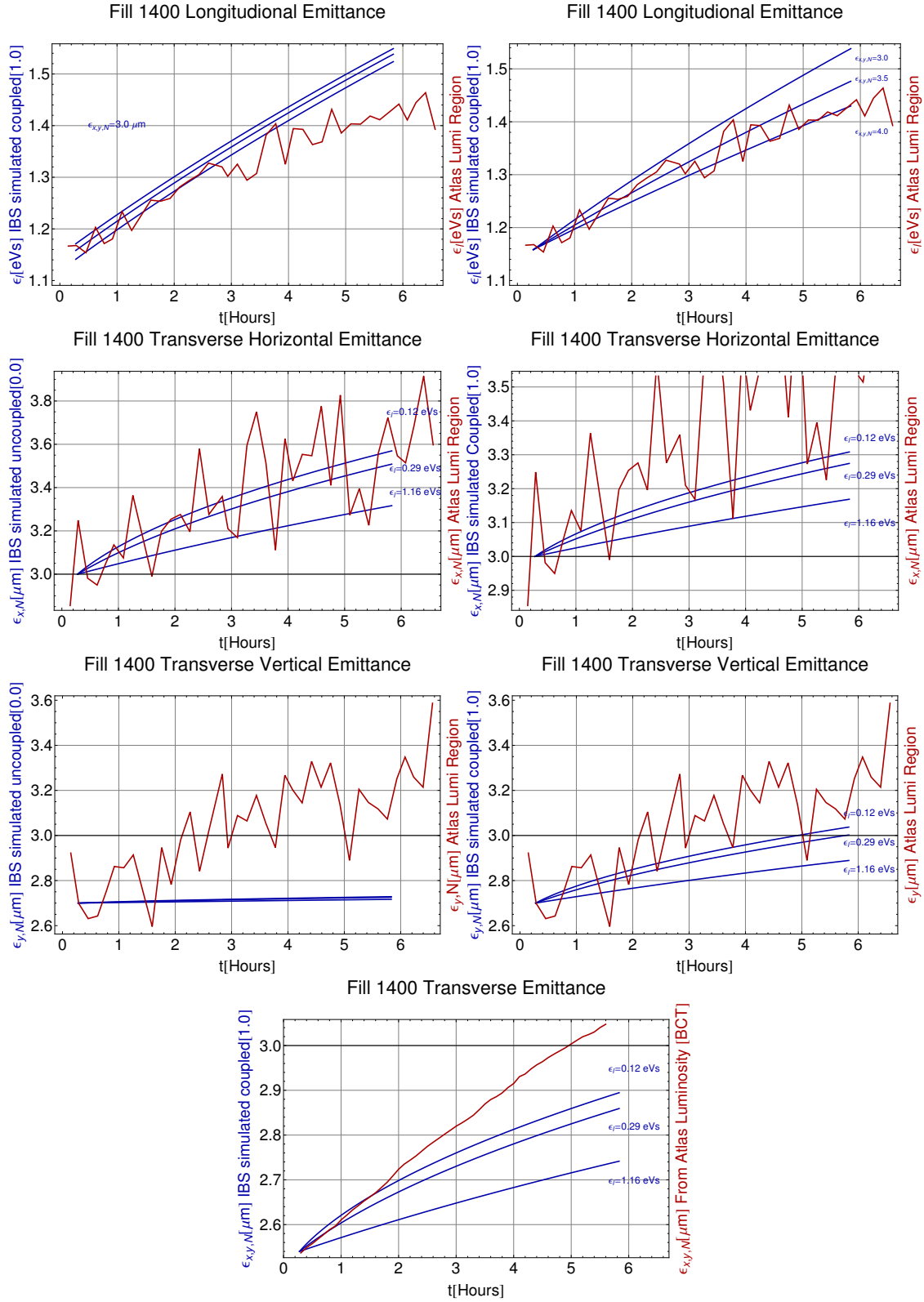


FIGURE 6.5.6. Emittance growth simulation vs data for proton fill 1400

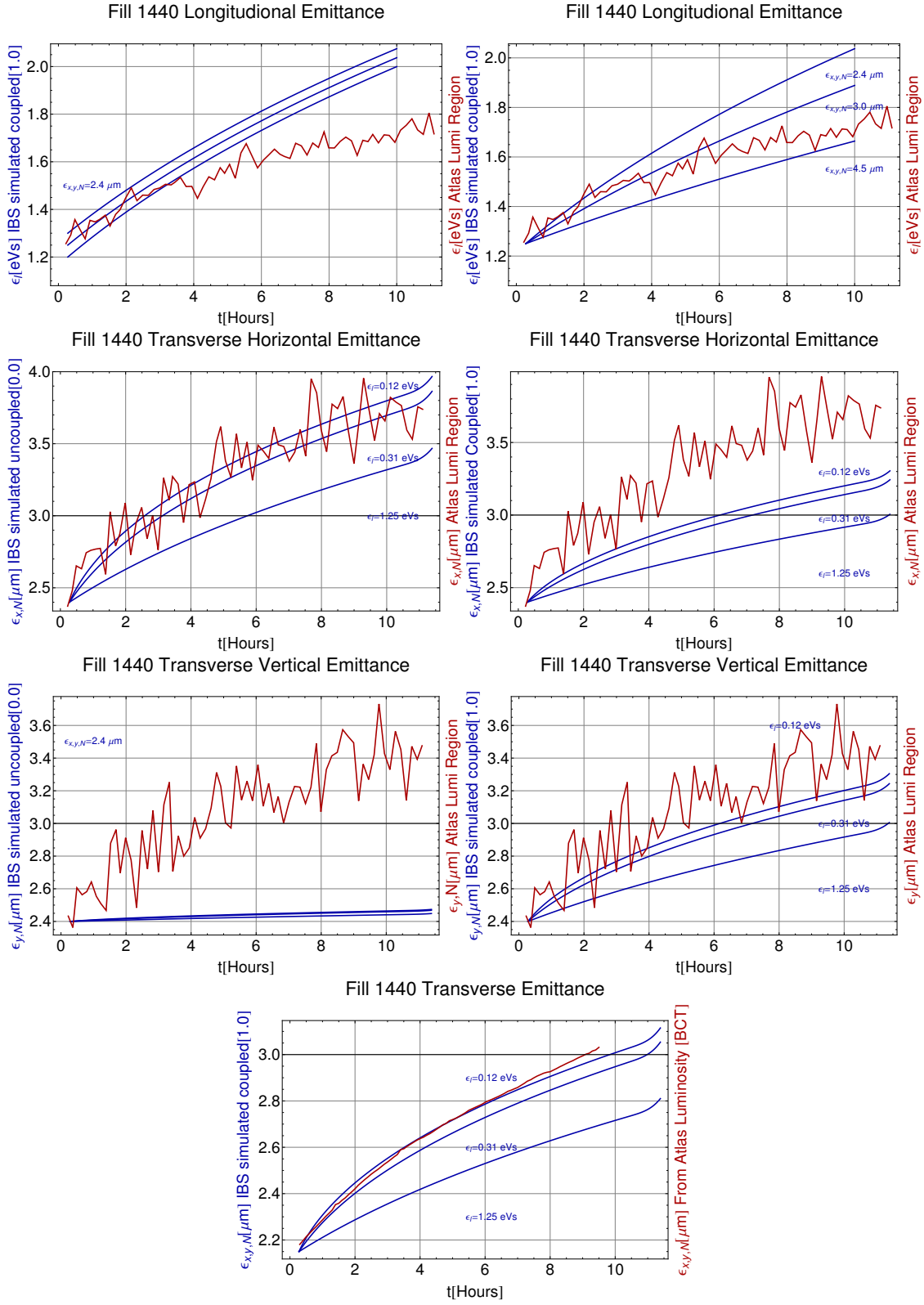


FIGURE 6.5.7. Emittance growth simulation vs data for proton fill 1440

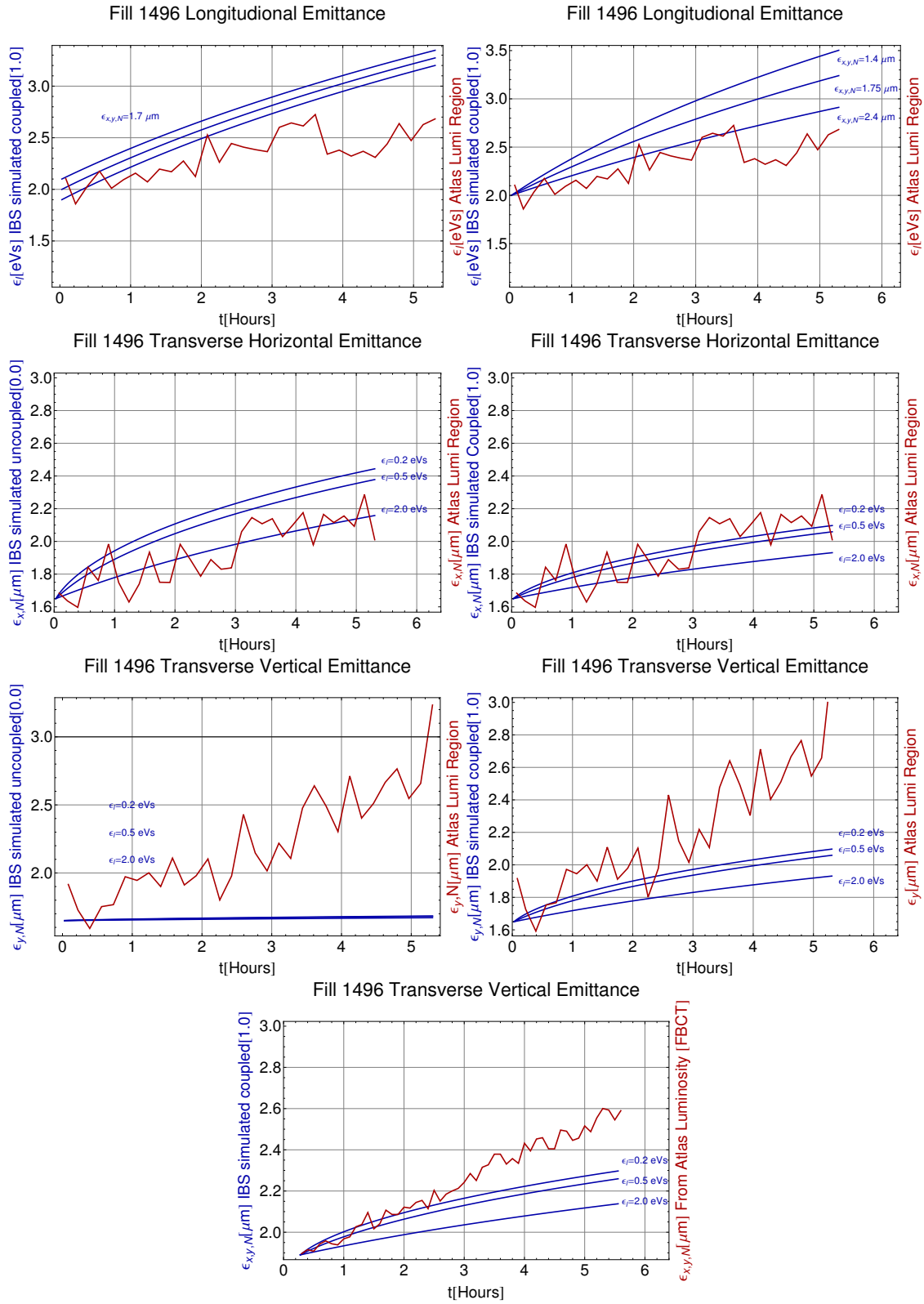


FIGURE 6.5.8. Emittance growth simulation vs data for ion fill 1496

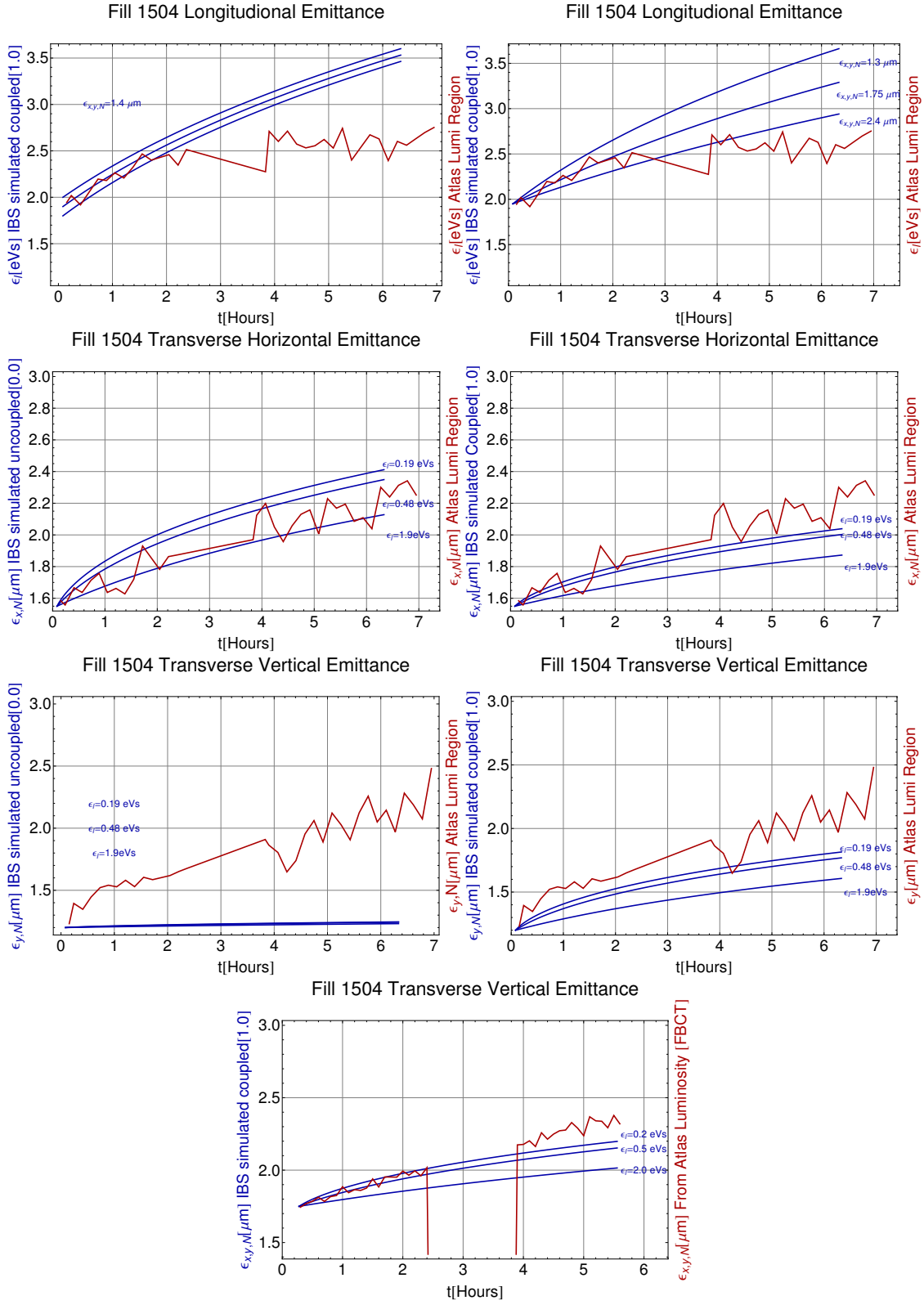


FIGURE 6.5.9. Emittance growth simulation vs data for ion fill 1504

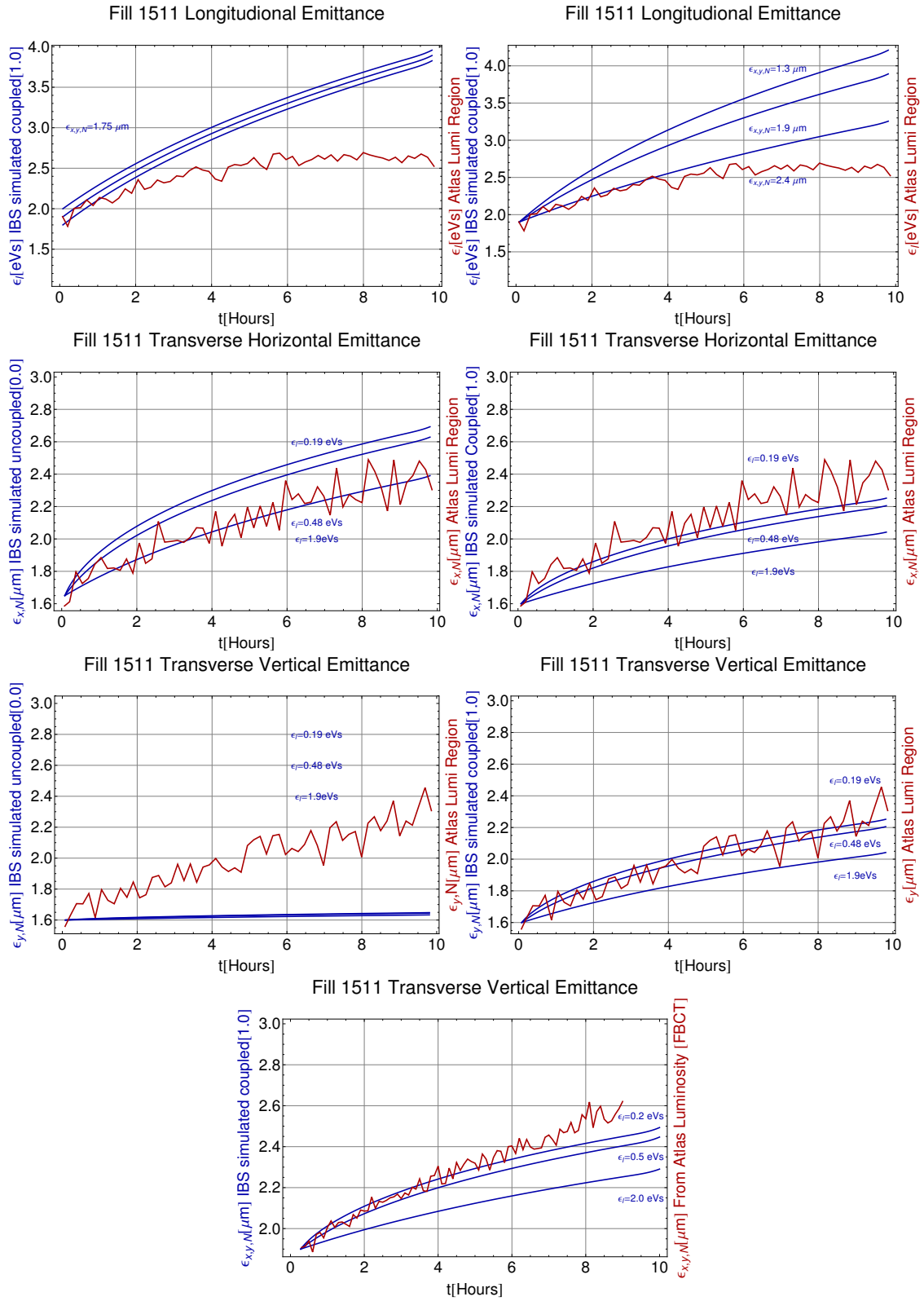


FIGURE 6.5.10. Emittance growth simulation vs data for ion fill 1511

Since in the above simulations I used the data from Atlas Luminous Region, I used the convoluted beam sizes. This means that the data I used has this hump effect integrated into it, so for sure for beam 1 I expect smaller transverse emittances than the data I used here shows. Because the simulations only account for the effect caused by IBS this might explain the difference in transverse growth rates between simulation and data.

Let me now turn to the particle tracking simulations in the hope that they will shed some more light on the above mentioned problems.

Particle Tracking Simulations

7.1. Introduction

In Particle Tracking Simulations (PTS) for accelerators one tracks the particles in the beam through the machine to study the behavior of the beam in the accelerator. The particle tracking algorithm is started by generating an initial particle distribution in phase-space to form the initial beam and then moves these particles through the machine keeping track of their individual behavior. The beam parameters in the machine at a certain point in time are then derived from the newly calculated distribution of these tracked particles. Usually this initial particle distribution has some assumptions about the initial conditions, in the simulations we assumed that the initial particle distribution was Gaussian in all the phase-space planes $((x, p_x), (y, p_y), (s, p_s))$. This choice is motivated by the fact that the IBS calculations in this text are for Gaussian distributed beams and that the bunches injected into the LHC from the SPS are known to be approximately Gaussian.

The PTS software is not designed to simulate the entire LHC beam but simulates a single LHC bunch. The simulation of the luminosity is then realized by assuming that the LHC contains a number of copies (number of bunches in the machine for the specific fill that we want to compare with the simulation) of this bunch. This means that in comparing the simulations with data we will need bunch by bunch data to study the IBS growths of a single bunch but that we need to use averages when we want to compare the simulations with luminosity data. Fortunately for the Ion runs the BSRTS were sometimes scanning through all the bunches giving us access to bunch by bunch data, while on the other hand the luminosity data published in the logbook by ATLAS is averaged over the colliding bunches so that we do not need to do the averaging locally anymore.

A single LHC bunch contains an enormous number of particles (in the order of 10^{11} for protons and in the order of 10^7 for ions), trying to track all of them would lead to unrealistic simulation times. The simulation software solves this by replacing a number (set by the user in the input for the simulation) of real particles by a so called macro particle. Instead of tracking all the real particles the software then tracks these macro particles, which brings the simulation times needed within acceptable levels (in the order a few hours up to a day, depending on the specific settings).

The software implementing the PTS algorithms was developed in FORTRAN by Roderik Bruce (CERN/LUND university) and Mike Blaskiewicz (BNL) in collaboration with John Jowett (CERN) who were so kind to make their algorithms available to me and answering any questions I had.

7.2. Simulations

To run a simulation the software needs some input files, one file that sets all the parameters for the simulation, another file which describes the optical lattice of the accelerator (“tfs” file) and depending on the IBS algorithm a file containing the IBS lifetimes calculated on a lattice (similar to what I did using MAD-X but using one of the models discussed in 5). The most relevant settings in the input file for this text are the initial beam emittances, intensities, number of bunches and assumed coupling between the transverse planes or not. In Appendix D.4 an example of such an input file is shown. The input file also allows the user to choose the algorithm that the simulation will use for determining the IBS lifetimes, the algorithms implemented at the time of writing are discussed in part 2 and a comparison of simulations with the different models is shown in section 7.3. Beam parameters are of course not only affected by IBS and since the goal is to get the simulations to agree with measured data as good as possible the software allows

the user to activate effects caused by radiation damping and collisions at the interaction points by setting a flag in the simulation input file. A discussion of these effects fall outside the scope of this text.

The file containing the description of the optical lattice, for the specific settings of the machine with respect to the fill that we want to compare with simulations, is a "*.tfs" file generated as output from the MAD-X software. This file needs to be generated independent of the simulation software by the user (using MAD-X).

Combining all this input the PTS software returns as output a number of files containing the data with the beam properties stored at the different time intervals (set by the user in the input file) during the simulation. To analyze the simulation results and compare them with the measured data we imported the simulation output files and the logged measured data in Mathematica. Then standard Mathematica functions were used to visualize both data and simulations. In the next sections I will show and discuss these results.

7.3. Comparing IBS algorithms

In this section I show some plots comparing the simulation results using different IBS algorithms but the same input beam parameters. Figure 7.3.1 shows a comparison for the different implemented models for beam 1 (similar plots for beam 2 can be found in figure D.5.1 in appendix D.5). The plots show that the models agree fairly well for all the simulated parameters with exception of the transverse emittance growths. The Piwinski smooth model is known to overestimate the IBS growth rates, but by setting the IBS strength parameter to 0.9 instead of 1.0 this model also agrees with the other models. These simulations were very time consuming as can be seen in figure 7.3.2, the total simulation time was 3874 minutes (or 2.7 days).

Based on these plots and on the returned simulation times we had decided to continue in this work with the Nagaitsev algorithm. Note in these plots already that when one assumes that the transverse planes are uncoupled the beam size should shrink in the vertical plane according to our models.

7.4. Comparing the simulations with data

The time has now come to compare the measurements of the 2010 Ion runs with simulations. We will show two examples here, one where the agreement with the simulations can be considered to be quite good (Ion Fill 1511) and one where the agreement seems less good (Ion Fill 1494).

The data we used to compare with the simulations is extracted from the LHC Logging Database, this data is automatically corrected according to the latest available correction factors and calibrations. Because of this we did not need to worry about correcting or calibrating the downloaded data, with one exception: the BSRTS data. The BSRTS data needs some additional corrections which were made available to me by Federico Roncarolo [7] from the Beam Instrumentation team. As I will show in the discussion below these BSRTS corrections are not complete in my opinion.

Ion Fill 1511 is an example where the agreement is quite good between measured data and simulation. Figure 7.4.1 shows a summary of that specific fill while the figures 7.4.2 and 7.4.3 show the comparison of the measured data with the simulations.

Both figures have two columns. In the left columns the measured data shown is the data extracted from the Logging Database as discussed before and the BSRTS data that is additionally corrected using the correction procedure from Federico Roncarolo (see also the discussion on this subject in section 6.4). The simulation plotted in the left column uses this data as input to set the initial conditions in the PTS input file. In the right column the data shown is again extracted from the Logging Database but we corrected the data from the BSRTS another time based on the ATLAS luminosity data. To explain how this new correction was done I first refer to equation (7.4.1) to show the relation between the different transverse emittances of both beams and the luminosity.

$$(7.4.1) \quad L(t) = \frac{\gamma I_1(t) I_2(t) k_c f}{2\pi \beta^* \sqrt{(\epsilon_{x1} + \epsilon_{x2})(\epsilon_{y1} + \epsilon_{y2})} k_{b1} k_{b2}},$$

where γ is the relativistic gamma factor (here equal to 1481.77), $f = 11245$ Hz is the particle revolution frequency in the machine, $L(t)$ is the luminosity measured by the ATLAS detector in function of time,

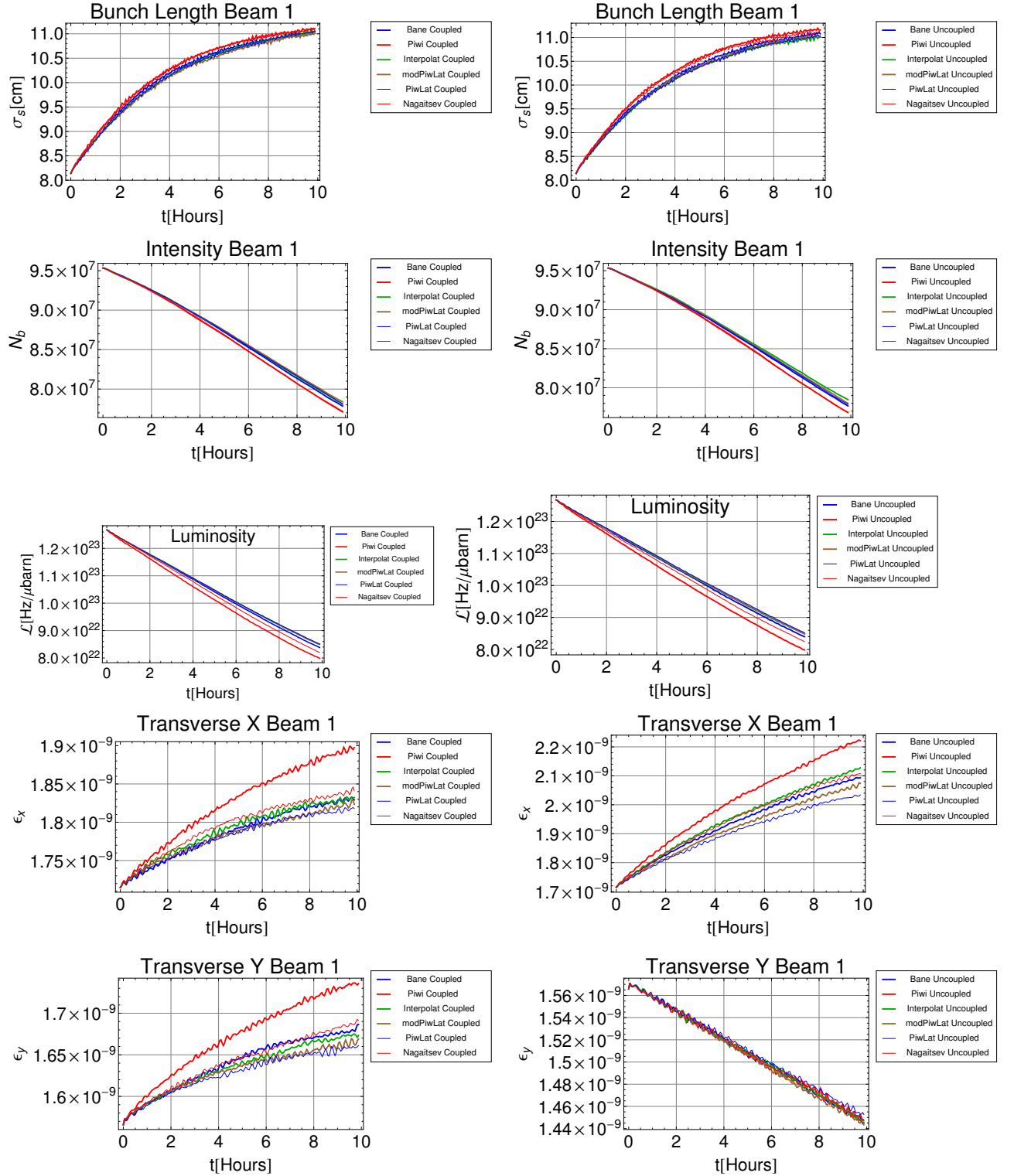


FIGURE 7.3.1. Comparison between the different Models

```

COLLIDER TIME EVOLUTION: run finished normally
*****
real    43m11.406s
user    0m5.012s
sys     42m49.969s

real    3874m14.484s
user    1m13.369s
sys     3857m53.186s
tmertens@tmertens-VirtualBox:~/shared/TESTCOLLIDER/co

```

FIGURE 7.3.2. Time of Simulation

Fillnumber	1511	
Nr of bunches	beam 1	beam 2
	121	121
Nr colliding bunches	ATLAS/CMS	ALICE
	113	114
INJPHYS	Mon 22 Nov 2010 21:13:51	Mon 22 Nov 2010 21:56:24
RAMP	Mon 22 Nov 2010 21:56:24	Mon 22 Nov 2010 22:21:49
FLATTOP	Mon 22 Nov 2010 22:21:49	Mon 22 Nov 2010 22:24:39
SQUEEZE	Mon 22 Nov 2010 22:24:39	Mon 22 Nov 2010 22:47:25
ADJUST	Mon 22 Nov 2010 22:47:25	Mon 22 Nov 2010 23:00:17
STABLE	Mon 22 Nov 2010 23:00:17	Tue 23 Nov 2010 09:00:28
BEAMDUMP	Tue 23 Nov 2010 09:00:28	Tue 23 Nov 2010 09:12:27
RAMPDOWN	Tue 23 Nov 2010 09:12:27	Tue 23 Nov 2010 09:23:36
SETUP	Tue 23 Nov 2010 09:23:36	Tue 23 Nov 2010 10:03:36
FILL	Mon 22 Nov 2010 19:34:48	Tue 23 Nov 2010 10:03:32

FIGURE 7.4.1. Fill 1511 Summary

$\beta^* = 3.5\text{m}$ is the value of the Beta-Function at the ATLAS interaction point, k_c is the number of colliding bunches at ATLAS, (k_{b1}, k_{b2}) are the respective number of bunches in beam 1 and beam 2 and $(I_1(t), I_2(t))$ are the respective intensities of beam 1 and beam 2 in function of time.

Considering that the absolute values of the BSRTS data can deviate from the actual values quite strongly and looking at equation (7.4.1) I was under the impression that the emittances calculated from this data were too large. This lead me to try to apply another correction to the BSRTS data. To do this correction I considered the top left plot in figure 7.4.2 and calculated the ratio between the simulated luminosity (blue curve) and the measured luminosity of the ATLAS detector (green curve) at $t = 0$. I then used this ratio as a correction factor for the initial transverse emittances ($\epsilon'_0 = R\epsilon_0$). From this ϵ'_0 the difference $\epsilon'_0 - \epsilon_0$ is determined and then subtracted from the other BSRTS data to get the corrected values, so basically applying a vertical downward translation on the BSRTS data. This correction procedure is also motivated by the fact that Federico Roncarolo explained to me that the absolute values of the BSRTS data are very “unstable” in the sense that they should be treated with care in their values but that the relative values should be correct. This means that the slopes of the BSRTS data can be trusted, but not the absolute values. The procedure I applied here to correct the BSRTS data is basically identical to the one described in section 6.4 and in [7] but with different values for different fills. Note that the same correction factor was used for the x and the y plane, agreement with simulations (see below) would probably improve if different correction factors were used for the different planes. Due to time limitations I was not able to optimize these corrections to have a different correction in the two transverse planes. The simulations in the right columns of figures 7.4.2 and 7.4.3 used this corrected data as input for the initial conditions of the simulation.

From the plots in the left columns of figures 7.4.2 and 7.4.3 it is clear that the simulation does not agree well with the measured data¹. But when I use the corrected data from BSRTS following the procedure discussed above the agreement becomes much better as can be seen in the right columns of figures 7.4.2 and 7.4.3. The luminosity and intensities agree amazingly well as can be seen in the two top right plots in figure

¹Blue and Red curves are respectively the simulated values for beam 1 and beam 2. The Green and the Brown curves are respectively the data for beam 1 and beam 2. In the Luminosity plots the Blue curve is the simulation, the Red curve represents the calculated values using equation (7.4.1) and the Green curve is the luminosity measured by ATLAS rescaled to two colliding bunches.

7.4.2. The simulation also seems to give a fairly good agreement for the vertical plane (lower right plot in figure 7.4.3). The bunch length data and the data for the horizontal plane seem not to agree very well (lower right plot in figure 7.4.2 and top right plot in figure 7.4.3) with the simulations. A possible explanation for this is that our simulations does not take effects as beam-beam effects and the up until now unexplained HUMP into consideration. Both these effects are known to blow up the beam size. In my opinion we are missing a transverse effect in our simulations. The motivation for this statement comes from the fact that if the simulations would include such an extra effect that makes the transverse beam size grow faster but does not affect the longitudinal beam size, the bunch lengths would grow slower because of larger transverse emittances (as can be seen in figures 6.3.2, showing the lifetimes for different beam sizes/emittances). This slower growth would make the simulation curves for the bunch length converge to the measured data and would increase the growth in the transverse plane (horizontal here) making the transverse simulation curves converge to the measured data.

The effects I described above are consistently present in the other comparisons with simulations I did (see Appendix D.6). The only exceptions are those fills where the HUMP shows up, blowing up the vertical beam size and causing faster loss of particles. In these cases the simulations deviate strongly for all the parameters: luminosity, intensity, bunch length and transverse emittances. An example of this is Ion Fill 1494 shown in figures 7.4.5 and 7.4.6. A summary of this fill is shown in figure 7.4.4. For this fill one can clearly see a transverse effect turning on and off around 1.5 hours and around 4.5 hours during the fill. Notice that this effect is much stronger for beam 2 than for beam 1. All simulations include the radiation damping effect which is assumed negligible at the currently used energies, radiation lifetimes are a factor 5 to 10 larger than the IBS lifetimes, and all simulations were done with full coupling between the x and y plane.

7.5. Conclusions

The various plots I showed in the previous section show the strong dependence on accurate data when comparing measured data to simulations. The fact that the LHC and its instruments are still under commissioning makes it hard to draw clear conclusions from the comparisons I made.

The comparison of data with particle tracking simulations show the same trend as the comparison with the simulations based on MAD-X (cfr. conclusions in section 6.6): transverse growth is underestimated and longitudinal growth is overestimated.

From the observations in section 7.4 and subsection 6.5.2, considering that our simulations do not take effects such as the HUMP, beam-beam (which is believed to be a quite strong effect in the LHC),... into account I would conclude that the models that we have to describe IBS are fairly good. This is motivated by the fact that the measured data for the luminosity and intensities correspond very well to the simulations.

The plots and the discussion on the corrections I applied to the data also show that there is still much work to be done on the beam instrumentation part of the LHC. On the other hand, assuming that our models for IBS are correct, the plots demonstrate that there are some strong effects besides IBS operating on the beam size in the LHC. It would be interesting to extend the particle tracking software to try to model these effects and see if there is anything there we do not fully understand.

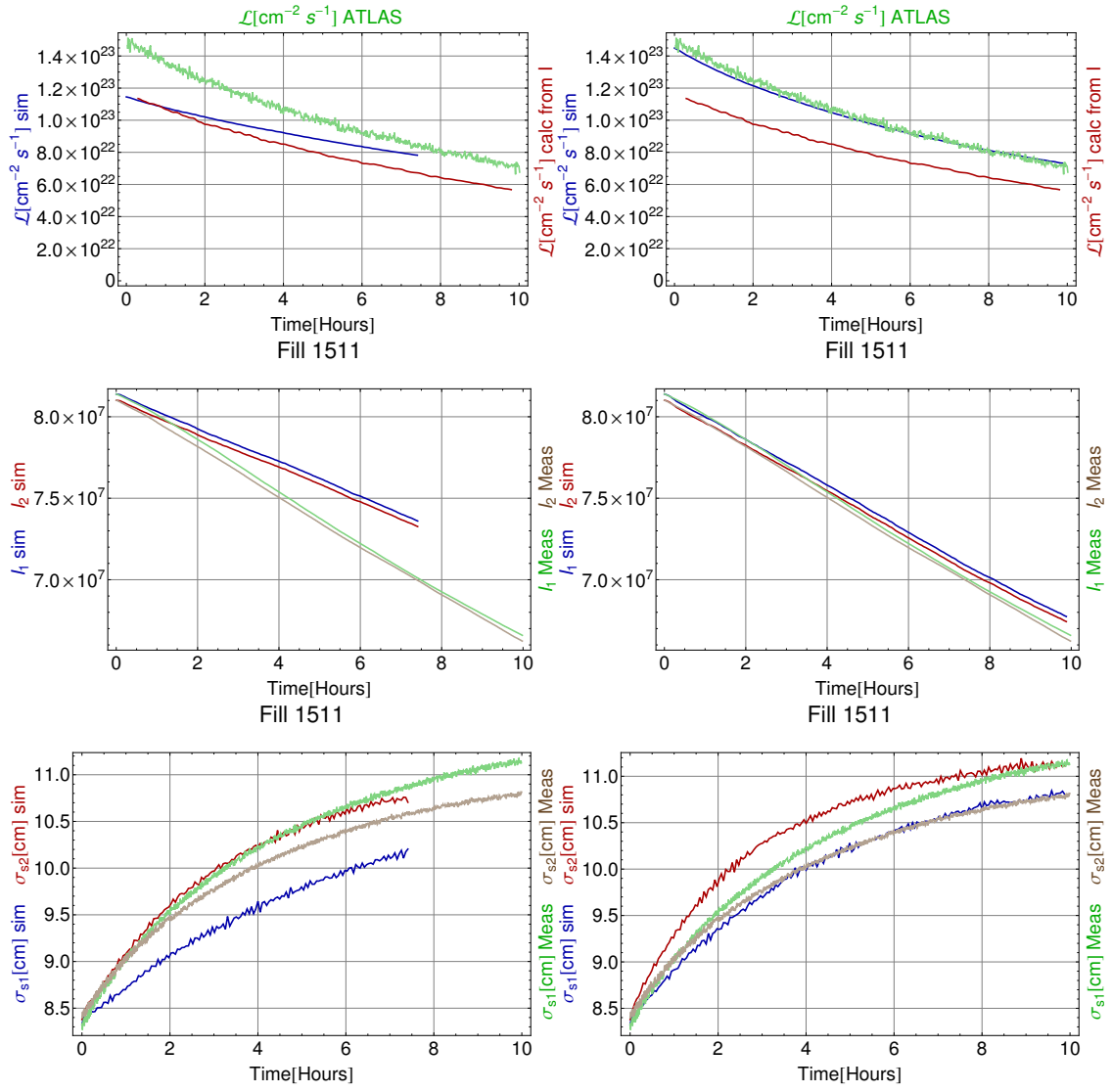


FIGURE 7.4.2. Fill 1511-1

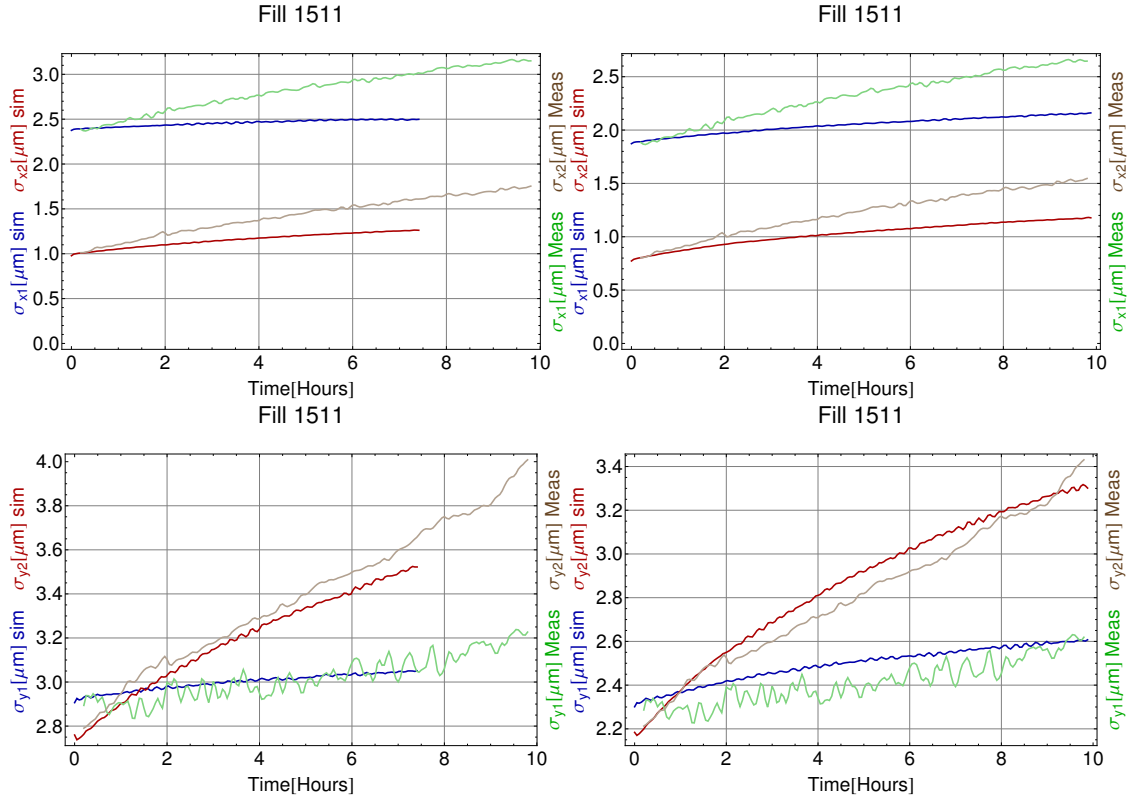


FIGURE 7.4.3. Fill 1511-2

Fillnumber	1494	
Nr of bunches	beam 1	beam 2
	121	121
Nr colliding bunches	ATLAS/CMS	ALICE
	113	114
INJPROT	Tue 16 Nov 2010 00:01:18	Tue 16 Nov 2010 01:14:44
INJPHYS	Tue 16 Nov 2010 01:14:44	Tue 16 Nov 2010 02:13:13
PRERAMP	Tue 16 Nov 2010 02:13:13	Tue 16 Nov 2010 02:15:25
RAMP	Tue 16 Nov 2010 02:15:25	Tue 16 Nov 2010 02:41:32
FLATTOP	Tue 16 Nov 2010 02:41:32	Tue 16 Nov 2010 02:44:32
SQUEEZE	Tue 16 Nov 2010 02:44:32	Tue 16 Nov 2010 03:15:10
ADJUST	Tue 16 Nov 2010 03:15:10	Tue 16 Nov 2010 03:29:43
STABLE	Tue 16 Nov 2010 03:29:43	Tue 16 Nov 2010 10:00:03
BEAMDUMP	Tue 16 Nov 2010 10:00:03	Tue 16 Nov 2010 10:07:13
RAMPDOWN	Tue 16 Nov 2010 10:07:13	Tue 16 Nov 2010 10:41:48
SETUP	Tue 16 Nov 2010 10:41:48	Tue 16 Nov 2010 10:54:17
FILL	Mon 15 Nov 2010 23:49:45	Tue 16 Nov 2010 10:53:56

FIGURE 7.4.4. Fill 1494 Summary

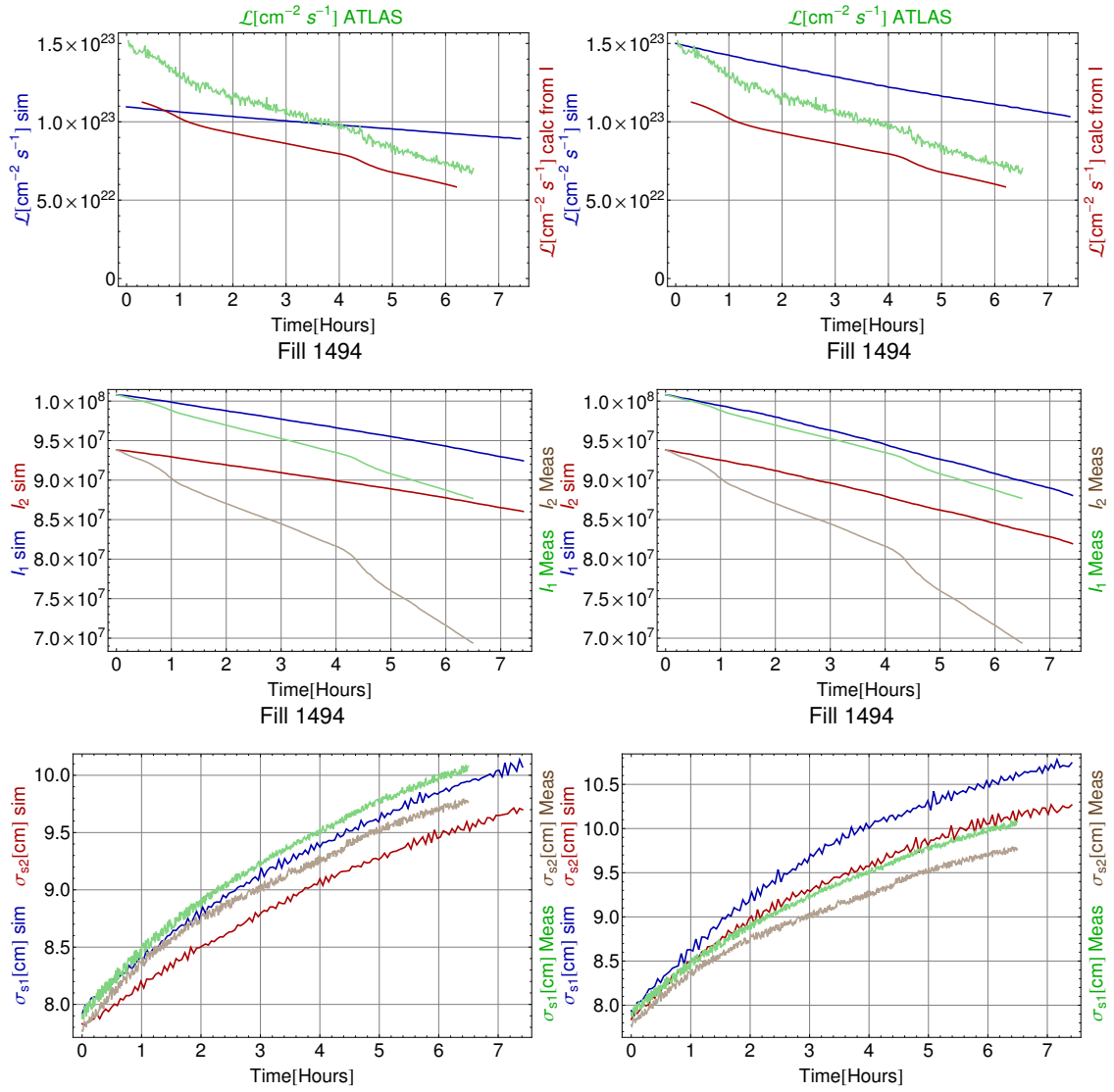


FIGURE 7.4.5. Fill 1494-1

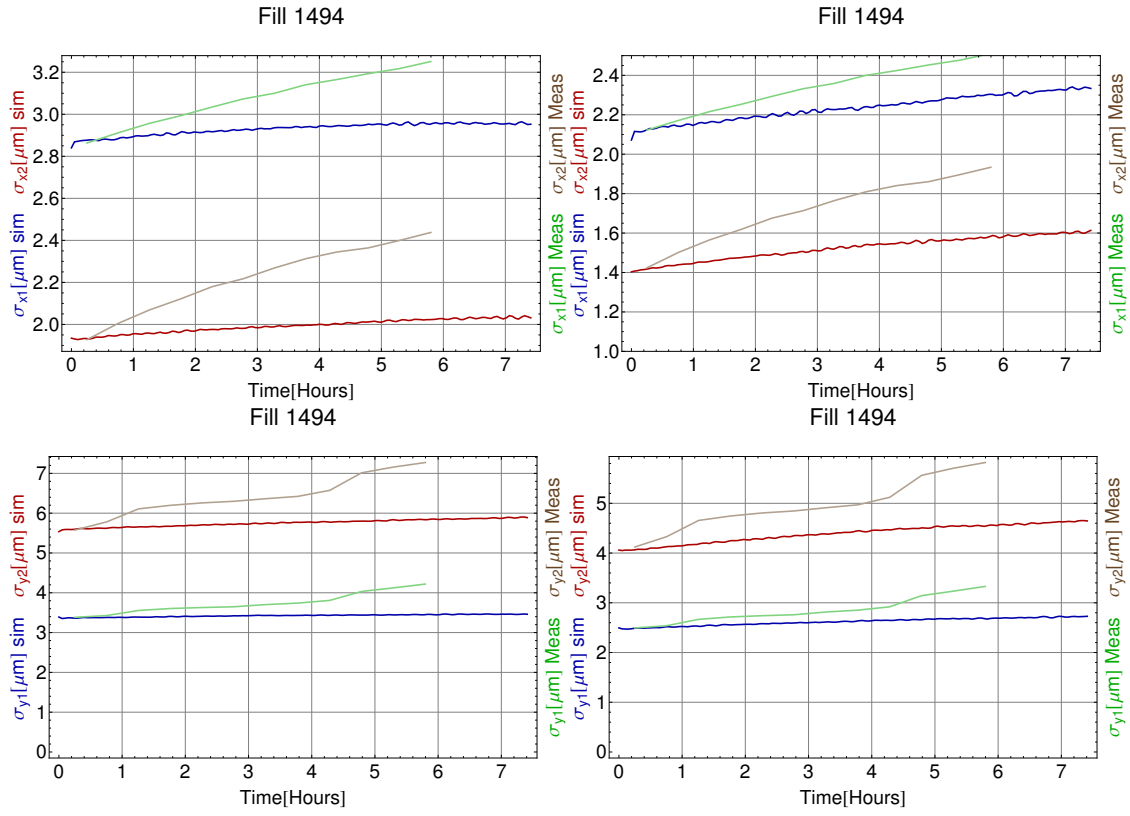


FIGURE 7.4.6. Fill 1494-2

Final conclusions and acknowledgments

8.1. Summary and Final Conclusions

In part one of this text I gave a short overview of some concepts used in Accelerator Physics, restricting myself to the most relevant for the subject of this thesis, Intrabeam Scattering. There exist several models for IBS, but in this text I chose to discuss the model presented by Bjorken and Mtingwa in [14] in detail, motivated by the close relation of their approach with particle physics and my background in particle physics.

Part two of my thesis goes through most of BM's calculations and gives a description of the reasoning that is applied to model IBS. In this part, one can also find an overview of the other IBS models that are implemented in the simulation software that was used.

Two different approaches to compare the simulations with the measured data were used, one approach was based on simulations done with the MAD-X software (see Chapter 6) and another approach was based on simulations done with a Particle Tracking code (see Chapter 7). They are described in part three of this thesis.

When comparing data with simulations, both approaches (sections 6.6 and 7.5) show a consistent picture: in both cases the simulations overestimate the bunch length growth but underestimate the growth in the transverse planes. The plots comparing the Particle Tracking Simulations with the (corrected) data seem to show that our models are fairly good in predicting the luminosity and the intensity of the beams when the HUMP is not present. As discussed in section 7.5 I would conclude from this that our models for IBS are good but that there are other processes affecting the transverse growths of the beams that are not implemented in the used simulation software (beam-beam effects, the HUMP,...). During one of the group meetings a model used at Tevatron it was brought to our attention that Betatron Noise might contribute strongly to transverse beam blow-up. During the finishing months of my internship we will try to implement this effect in the simulation software to check if this is true or not.

In chapters 6 and 7 I restricted myself in comparing data with simulations during physics, meaning that the beams were in collision at 3.5 TeV. It would be interesting to see if the same picture, as described above, would emerge at injection energy (450 GeV) without the beams in collision. Unfortunately the data that is available on the beam sizes at injection energy is very limited, combined with the fact that the beams usually are not kept at injection energy for a long time makes it very hard to gather enough data to use as input in the simulation software or to compare with simulations.

Instruments will improve and new measuring devices will be (already have been) commissioned during 2011 opening up the possibility to investigate IBS at injection energy for the Ion run in 2011.

8.2. Acknowledgments

I would like to thank a number of people who have helped me to understand and explore the subject of this thesis, including the following: Roderik Bruce, Federico Roncarolo, Vera Kain, Giulia Papotti, Heiko Damerau and especially my supervisor John Jowett - all from CERN. Also, my supervisor - professor Miguel Sousa Da Costa of the University of Porto for the guidance during the writing of my thesis, professor Maria Augusta Santos (University of Porto) for accepting me as a master student and my girlfriend Lara for her comments. Not least, perhaps, I should thank my father, Julien, for his support and help with practical matters allowing me to focus on my thesis and studies. I hope that you have enjoyed reading this work and that you have found it interesting!

Tom Mertens

Bibliography

- [1] *Numerical Recipes in Fortran*. Cambridge University Press, 1996.
- [2] Lhc design report, volume 1. Technical report, Cern, 2004.
- [3] J.D. Bjorken and S.D. Drell. *Relativistic Quantum Mechanics*. Mc Graw-Hill, 1964.
- [4] Roderik Bruce. *Beam loss mechanisms in relativistic heavy-ion colliders*. PhD thesis, Lund University, 2009. CERN-THESIS-2010-030.
- [5] CAS CERN. *Transverse Beam Dynamics*, 2008. Power point presentation at CAS, Frascati Italy 2008.
- [6] CERN. *CAS proceedings, Advanced Accelerator Physics*, 1987.
- [7] CERN. *CAN WE GET A RELIABLE ON-LINE MEASUREMENT OF THE TRANSVERSE BEAM SIZE?*, 2010. Evian workshop.
- [8] CERN. *Emittance Preservation*, 2010. Evian proceedings.
- [9] A. Wu Chao and M. Tigner. *Handbook of Accelerator Physics and Engineering*. World Scientific, 1999.
- [10] T.P. Cheng and L.F. Li. *Gauge Theory of elementary particle physics*. Oxford Science, 2008.
- [11] EPAC2002. *A simplified Model of Intrabeam Scattering*, 2002. Stanford Linear Accelerator Center.
- [12] W. Herr. Student lectures be department, 2011. CERN BE Department.
- [13] J. Jacod and P. Protter. *Probability Essentials*. Springer, second edition edition, 2004.
- [14] S.K. Mtingwa J.D. Bjorken. Intrabeam scattering. *Part. Acc.*, 13:115–143, 1983.
- [15] K. Kubo and K. Oide. Intrabeam scattering in electron storage rings. *Physical Review Special Topics - Accelerators and Beams*, 4, 2001. PhysRevSTAB.4.124401.
- [16] S. Y. Lee. *Accelerator Physics*. World Scientific, 2004.
- [17] F. Mandl and G. Shaw. *Quantum Field Theory*. John Wile and Sons, 2008.
- [18] S. Nagaitsev. Intrabeam scattering formulas for fast numerical evaluation. *Physical Review Special Topics - Accelerators and Beams*, 8, 2005. PhysRevSTAB.8.064403.
- [19] PAC2001. *Quantum Statistics Correction to Intrabeam Scattering Rates*, 2001. Stanford Linear Accelerator Center.
- [20] M. Blaskiewicz R. Bruce, J.M. Jowett and W. Fisher. Time evolution of the luminosity of colliding heavy-ion beams in rhic and lhc. *Physical Review Letters Accelerators and Beams*, 2010.
- [21] D. Lide R. E. Cohen and G. Trigg. *AIP Physics Desk Reference*. Springer, 2003.
- [22] A. S. Fisher B. Lindquist A. Roodman J. M. Thompson W. Kozanecki, Y. Cai and M. Weaver. 1 interaction-point phase-space characterization using single-beam and luminous-region measurements at pep-ii *. *Nuclear Instruments and Methods in Physics Research A*, 607:293–321, 2009.
- [23] H. Wiedemann. *Particle Accelerator Physics*. Springer, 2006.
- [24] E. Wilson. *Introduction to Particle Accelerators*. Oxford University Press, 2001.
- [25] Frank Zimmerman. Intrabeam scattering with non-ultrarelativistic corrections and vertical dispersion for mad-x, 2006. CERN-AB-2006-002.

Part 4

Appendix

APPENDIX A

Canonical transformations

Hamilton's equations of motion are described in the variables (q, p) , the coordinates and the momenta [16]. There is another set of variables that can be useful to describe the equations of motion in, namely (Q, P) . These new variables are defined through a generating function G . G can be

$$(A.0.1) \quad F_1(q, Q, t); \quad F_2(q, P, t); \quad F_3(p, Q, t); \quad F_4(p, P, t)$$

Such a variable transformation is called a canonical transformation.

$$(A.0.2) \quad G = F_1(q, Q, t): \quad p = \frac{\partial F_1}{\partial q}, \quad P = -\frac{\partial F_1}{\partial Q}; \quad \mathcal{H}(Q, P, t) = H(q, p, t) + \frac{\partial F_1}{\partial t}$$

$$(A.0.3) \quad G = F_2(q, P, t): \quad p = \frac{\partial F_2}{\partial q}, \quad Q = \frac{\partial F_2}{\partial P}; \quad \mathcal{H}(Q, P, t) = H(q, p, t) + \frac{\partial F_2}{\partial t}$$

$$(A.0.4) \quad G = F_3(p, Q, t): \quad q = -\frac{\partial F_3}{\partial p}, \quad P = -\frac{\partial F_3}{\partial Q}; \quad \mathcal{H}(Q, P, t) = H(q, p, t) + \frac{\partial F_3}{\partial t}$$

$$(A.0.5) \quad G = F_4(p, P, t): \quad p = -\frac{\partial F_4}{\partial q}, \quad Q = \frac{\partial F_4}{\partial P}; \quad \mathcal{H}(Q, P, t) = H(q, p, t) + \frac{\partial F_4}{\partial t}$$

These transformations can be useful to reduce the equations to $\mathcal{H} = 0$. Finding the equations of motion is then equivalent to finding the generating function.

APPENDIX B

Betatron motion for off-momentum particles

Starting from

$$x'' - \frac{\rho + x}{\rho^2} = \frac{B_y}{B\rho} \frac{p_0}{p} \left(1 + \frac{x}{\rho}\right)^2$$

using $B_y = B_0 + B_1 x$

$$x'' - \frac{\rho + x}{\rho^2} = \frac{B_0 + B_1 x}{B\rho} \frac{p_0}{p} \left(1 + \frac{x}{\rho}\right)^2$$

Now defining $K(s) = \frac{B_1}{B\rho}$ and using $B_0 = \frac{-B\rho}{b_0}$ ($b_0 = 1$ in the normalization I used in the Bethe expansion) the above equation can be written as

$$x'' - \frac{\rho + x}{\rho^2} = \left(-\frac{1}{\rho} + K(s)x\right) \frac{p_0}{p} \left(1 + \frac{x}{\rho}\right)^2$$

Expanding to first order in $\frac{x}{\rho}$ leaves

$$\begin{aligned} x'' - \frac{\rho + x}{\rho^2} &= \left(-\frac{1}{\rho} + K(s)x\right) \frac{p_0}{p} \left(1 + 2\frac{x}{\rho}\right) \\ x'' - \frac{\rho + x}{\rho^2} &= -\frac{1}{\rho} \frac{p_0}{p} + \frac{p_0}{p} K(s)x - 2\frac{x}{\rho^2} \frac{p_0}{p} \end{aligned}$$

Using $\delta = \frac{\Delta p}{p_0}$

$$x'' - \frac{\rho + x}{\rho^2} = -\frac{1}{\rho(1+\delta)} + \frac{K(s)x}{(1+\delta)} - 2\frac{x}{\rho^2(1+\delta)}$$

and after reordering finally gives

$$x'' + x \left(\frac{1-\delta}{\rho^2(1+\delta)} - \frac{K(s)}{1+\delta} \right) = \frac{\delta}{(1+\delta)\rho}$$

APPENDIX C

Expression for the dispersion function

First rewriting the proposed expression

$$D(s) = M_{22}(s) \int_{s_0}^s \frac{1}{\rho} M_{11}(\tilde{s}) d\tilde{s} - M_{11}(s) \int_{s_0}^s \frac{1}{\rho} M_{22}(\tilde{s}) d\tilde{s}$$

with the notation from equation (2.5.7)

$$D(s) = S(s) \int_{s_0}^s \frac{1}{\rho} C(t) dt - C(s) \int_{s_0}^s \frac{1}{\rho} S(t) dt$$

Taking the first and second derivative

$$\begin{aligned} D' &= S' \int \frac{1}{\rho} C dt + S \frac{1}{\rho} C - C' \int \frac{1}{\rho} S dt - C \frac{1}{\rho} S \\ &= S' \int \frac{1}{\rho} C dt - C' \int \frac{1}{\rho} S dt \\ D'' &= S'' \int \frac{1}{\rho} C dt + S' \frac{1}{\rho} C - C'' \int \frac{1}{\rho} S dt - C' \frac{1}{\rho} S \\ &= S'' \int \frac{1}{\rho} C dt - C'' \int \frac{1}{\rho} S dt + \frac{1}{\rho} (CS' - SC') \\ &= S'' \int \frac{1}{\rho} C dt - C'' \int \frac{1}{\rho} S dt + \frac{1}{\rho} \det M \\ &= S'' \int \frac{1}{\rho} C dt - C'' \int \frac{1}{\rho} S dt + \frac{1}{\rho} \end{aligned}$$

Remember that S and C are solutions of the homogeneous Hill's equations of motions

$$\begin{aligned} S'' + KS &= 0 \\ C'' + KC &= 0 \end{aligned}$$

This gives for the second derivative of the dispersion

$$\begin{aligned} D'' &= -K \left(S \int \frac{1}{\rho} C dt + C \int \frac{1}{\rho} S dt \right) + \frac{1}{\rho} \\ &= -KD + \frac{1}{\rho} \end{aligned}$$

Or

$$D'' + KD = \frac{1}{\rho}$$

APPENDIX D

Simulations

D.1. Example of a Sequence File

```
circum = 6912.0;

ncell = 108;
lcell = circum/ncell;

lquad = 3.085;
lquad2 = lquad/2;
lmb = 6.260;
lmb2 = lmb/2;
lsex = 1.0;

mbsps: multipole , lrad = dummy, l=lmb, knl={2.0*pi/(8*ncell)};

qsps: quadrupole , l=lquad;
qf: qsps , k1:=kqf;
qd: qsps , k1:=kqd;
kqf = 1.46314747E-02;
kqd = -1.4643443E-02;

lsf: sextupole , l=lsex , k2:= ksf;
lsd: sextupole , l=lsex , k2:= ksd;
ksf = 2.02844420E-02;
ksd = -3.83942672E-02;

bpm: monitor , l=0.1;
ch: hkicker , l=0.1;
cv: vkicker , l=0.1;

cassps: sequence , refer=centre , l=circum;
start_machine: marker , at =0;

n=1;
while (n<ncell+1){
  qf: qf , at=(n-1)*lcell+lquad2;
  lsf: lsf , at=(n-1)*lcell+lquad2+2.5;
  ch:ch , at=(n-1)*lcell+lquad2+3.1;
  bpm: bpm , at=(n-1)*lcell+lquad2+3.2;
```

```

mbsps: mbsps,          at=(n-1)*lcell+lquad2+3.50;
mbsps: mbsps,          at=(n-1)*lcell+lquad2+9.90;
mbsps: mbsps,          at=(n-1)*lcell+lquad2+22.10;
mbsps: mbsps,          at=(n-1)*lcell+lquad2+28.50;
qd: qd,                at=(n-1)*lcell+lquad2+32.00;
lsd: lsd,              at=(n-1)*lcell+lquad2+34.50;
cv:cv,                 at=(n-1)*lcell+lquad2+35.10;
bpm: bpm,              at=(n-1)*lcell+lquad2+35.20;
mbsps: mbsps,          at=(n-1)*lcell+lquad2+35.50;
mbsps: mbsps,          at=(n-1)*lcell+lquad2+41.90;
mbsps: mbsps,          at=(n-1)*lcell+lquad2+54.90;
mbsps: mbsps,          at=(n-1)*lcell+lquad2+60.50;

n = n+1;
}
end_machine: marker, at = circum;
endsequence;

```

D.2. Example of a MAD-X program

```

title , s='test';

call , file="C:\Users\tmertens\madtest\cassps.seq";
option ,echo;

Beam, particle = proton , sequence=cassps , energy=450.0, npart=1.05E11, sigex = 4.5E-04;

use , sequence=cassps;

select , flag=twiss , column=name,s,betx,bety;

twiss ,save ,centre ,file=twiss.out;

plot , haxis=s, vaxis=x,betx, bety, colour = 100, range=qd[10]/qd[16];
plot , haxis=s, vaxis=dx, colour=100, range =qd[10]/qd[36];
stop;

```

D.3. Part of Twiss.out File

```

@ NAME           %05s "TWISS"
@ TYPE           %05s "TWISS"
@ SEQUENCE       %06s "CASSPS"
@ PARTICLE       %06s "PROTON"
@ MASS           %le      0.938272013
@ CHARGE         %le      1
@ ENERGY        %le      450
@ PC             %le      449.9990218
@ GAMMA          %le      479.6050546
@ KBUNCH         %le      1
@ BCURRENT       %le      0.0007296518407

```

```

@ SIGE           %le           0.00045
@ SIGT           %le           0
@ NPART          %le           1.05e+011
@ EX             %le           1
@ EY             %le           1
@ ET             %le           1
@ LENGTH         %le           6912
@ ALFA           %le           0.00168921016
@ ORBIT5         %le           0
@ GAMMATR        %le           24.33089909
@ Q1             %le           26.58000011
@ Q2             %le           26.61999911
@ DQ1            %le           0.04314791885
@ DQ2            %le           0.1368827693
@ DXMAX          %le           2.572345998
@ DYMAX          %le           0
@ XCOMAX         %le           0
@ YCOMAX         %le           0
@ BETXMAX        %le           107.5443181
@ BETYMAX        %le           107.4973056
@ XCORMS         %le           0
@ YCORMS         %le           0
@ DXRMS          %le           1.941458662
@ DYRMS          %le           0
@ DELTAP         %le           0
@ SYNCH_1        %le           0
@ SYNCH_2        %le           0
@ SYNCH_3        %le           0
@ SYNCH_4        %le           0
@ SYNCH_5        %le           0
@ TITLE          %01s "s"
@ ORIGIN          %19s "MAD-X 4.01.00 Win32"
@ DATE           %08s "10/09/10"
@ TIME           %08s "11.22.52"

```

* NAME	S	BETX	BETY
\$ %s	%le	%le	%le
"CASSPS\$START"	0	103.8655163	20.28397098
"START_MACHINE"	0	103.8655163	20.28397098
"QF"	1.5425	107.5443181	19.47450606
"DRIFT_0"	3.31375	102.790391	20.53014161
"LSF"	4.0425	99.4093121	21.3584847
"DRIFT_1"	4.5675	97.01509337	21.99682745
"CH"	4.6425	96.67590274	22.09086295
"BPM"	4.7425	96.22475325	22.21734949
"DRIFT_2"	4.9175	95.43827952	22.44174209
"MBSPS"	5.0425	94.87887975	22.60439225
"DRIFT_3"	8.2425	81.22989337	27.44060831
"MBSPS"	11.4425	68.87370267	33.57101393

"DRIFT_4"	17.5425	48.90078339	48.84203
"MBSPPS"	23.6425	33.62561087	68.81585796
"DRIFT_3"	26.8425	27.49099933	81.17455085
"MBSPPS"	30.0425	22.64918345	94.82743331
"DRIFT_5"	31.02125	21.426446	99.2617511
"QD"	33.5425	19.51348878	107.4973056
"DRIFT_0"	35.31375	20.57132767	102.7416292
"LSD"	36.0425	21.4012401	99.35936904
"DRIFT_1"	36.5675	22.04066861	96.96434406
"CV"	36.6425	22.13485616	96.62504132
"BPM"	36.7425	22.26154424	96.17374353
"DRIFT_2"	36.9175	22.48628626	95.38701356
"MBSPPS"	37.0425	22.64918345	94.82743331
"DRIFT_3"	40.2425	27.49099933	81.17455085
"MBSPPS"	43.4425	33.62561087	68.81585796
...			
"DRIFT_7"	6907.2425	82.86531691	26.76530531
"MBSPPS"	6910.0425	94.87887975	22.60439225
"DRIFT_5"	6911.02125	99.31172752	21.38364592
"END_MACHINE"	6912	103.8655163	20.28397098
"CASSPS\$END"	6912	103.8655163	20.28397098

D.4. Example of an input file for the PTS

```

*****      processes
*****
1      RFswitch      (set      to      1      to      activate
synchrotron      motion)
1      betatronSwitch (set      to      1      to      activate
betatron      motion)
1      raddampSwitch (set      to      1      to      activate
radiation      damping and      quantum excitation)
1      IBSSwitch      (set      to      1      to      activate      ibr)
1      collisionSwitch (set      to      1      to      activate
collisions)
*****      ring ,      general parameters
*****
15000  100000  20000.  100      12763      nturns , nMacro , timeRatio (=real      turns /
sim .      turns) , nwrite , iseed
55.7      26658.8832      1481.77      gammat , circ , gamma0 ,
0.      360      -1.21e7  35640      vrf , nharm , vrf2 , nharm2
64.31      59.32      2.      2.      0.      tunex , tuneY , chromx , chromy , dqmin (
coupling      between x-py ,      y-px)
208      82      2.5e-9      aatom , qatom , thib
LHCb2-collisionIons -6.503.tfs
*****      starting      conditions
*****

```

```

1.918374919177079e-9    2.8501707314477675e-9    7.750507395121951e7    emix1 ,
    emiy1 ,    pnumber1 ,    (parameters    for    beam1)
1.3456535825842876e-9    4.759923120206548e-9    7.858155395121951e7    emix2 ,
    emiy2 ,    pnumber2    (parameters    for    beam2)
3    longCoordMethod (0:parabolic    with    smoking ,    1:    read
    from    file ,    2:    bi-Gaussian ,    3:    pseudo-Gaussian ,
    exactly matched)
0.07781229518598619    0.0745484506446665    rmsBunchLen1 , ,    rmsBunchLen2
    (only    used    for    longCoordMethod=2,3)
0.0001137    0.0001137    rmsDelta1 ,rmsDelta2    (only    used    for
    longCoordMethod=2)
1.25e-9 1.25e-9 0.01    0.75    5    tauhat1 ,    tauhat2 ,
    bunchLenPrecis (for    longCoordMethod=3) ,    power (for
    longCoordMethod=0) ,    alint    (for    longCoordMethod=0)
/home/roderik/My_CERN_work/blaskiewicz-code/rhic-track-round-beams/allcoord-B1
-15000-from-old-run.txt
/home/roderik/My_CERN_work/blaskiewicz-code/rhic-track-round-beams/allcoord-B1
-15000-from-old-run.txt
*****    radiation    damping
*****
lattice radMethod:    can    be    manual (input next line), approx
    (smooth latt.    I4=0), or    lattice (rad.    int.,    twiss file
    required)
23519.    47072.    4.64e-12    7.43e-8 tradlong(s),tradperp(s),siglong (eq.
    sigma from raddamp-exit.),sigperp(m)    (only    used    with
    manual method)
2784.32 rho0    (dipole bend.    radius in    m,    used    only    with
    approx)
*****    IBS
*****
nagaitsev    ibsMethod:    can    be    piwiSmooth ,    piwLattice ,
    modPiwLatt ,    baneApprox    or    interpolat
1    20.    coupleIBS    (0    gives    separate    growth rates ,
    1    gives    same    growth in    x    and    y) ,
    coulomblog
1    500    fracibstot ,    nbins
ibs-rates-LHC-coll001.dat
gBaneTab.dat
***** collisions
*****
6a    collRoutine    (1d    is    slow    but    without assumptions
    on    distributions ,    6a    is    fast    with    assumed
    Gaussian    transverse)
1    515    noIPs    with    _different_    parameters ,sigI (cross
    section for    particle    removal in    collisions) ,

```

1 100 0 nbunches , longIntBins , angleSwitch (set
to one for alternating angle betw. hor. and
ver plane , used with 1d)
3.5 0. 3 betaSX , half crossing angle , multiplicity
(noIPs with these parameters) at first IP

D.5. Comparing simulation models (beam 2)

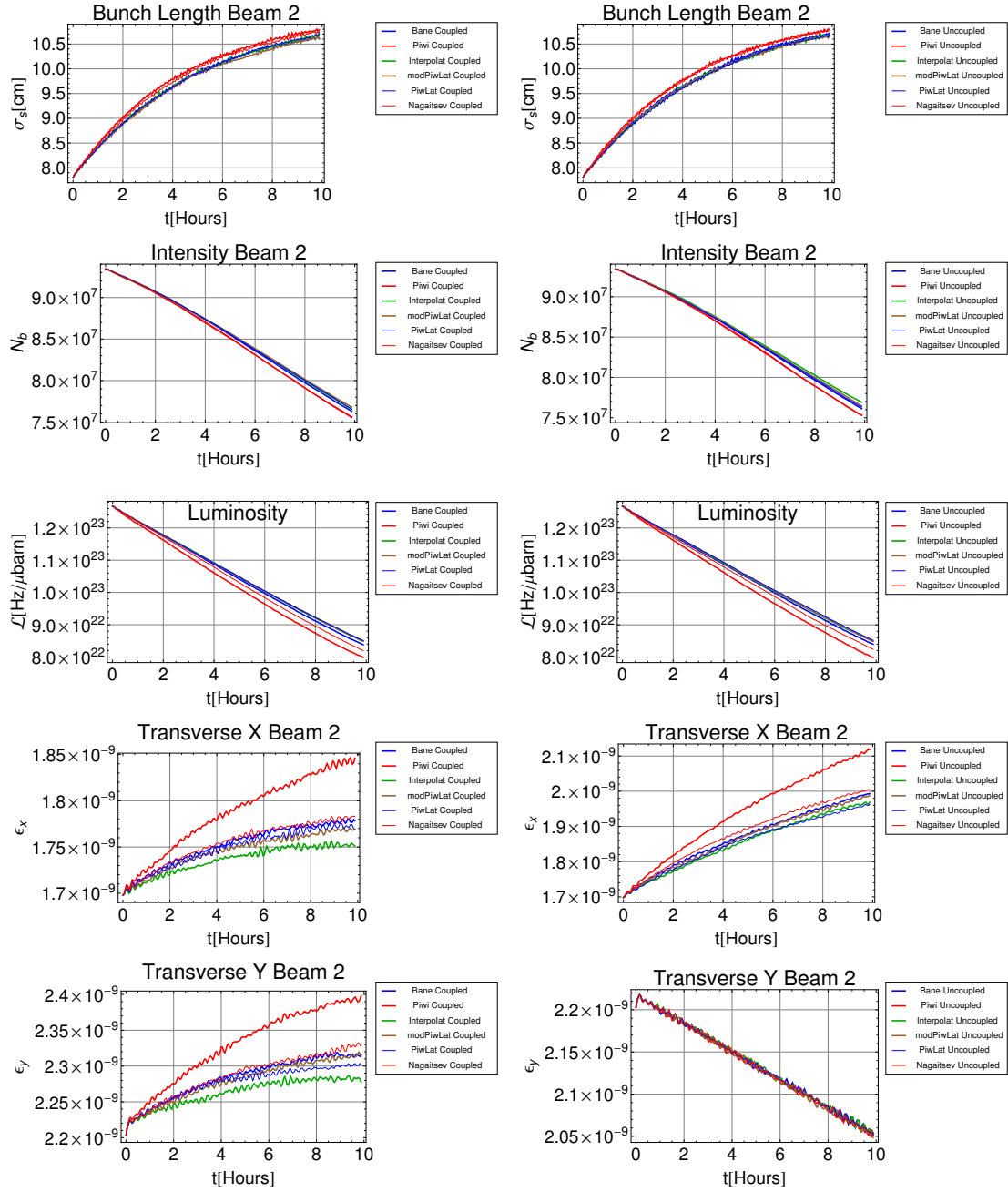


FIGURE D.5.1. Comparison between the different Models

D.6. Additional comparisons of data with PTS simulations

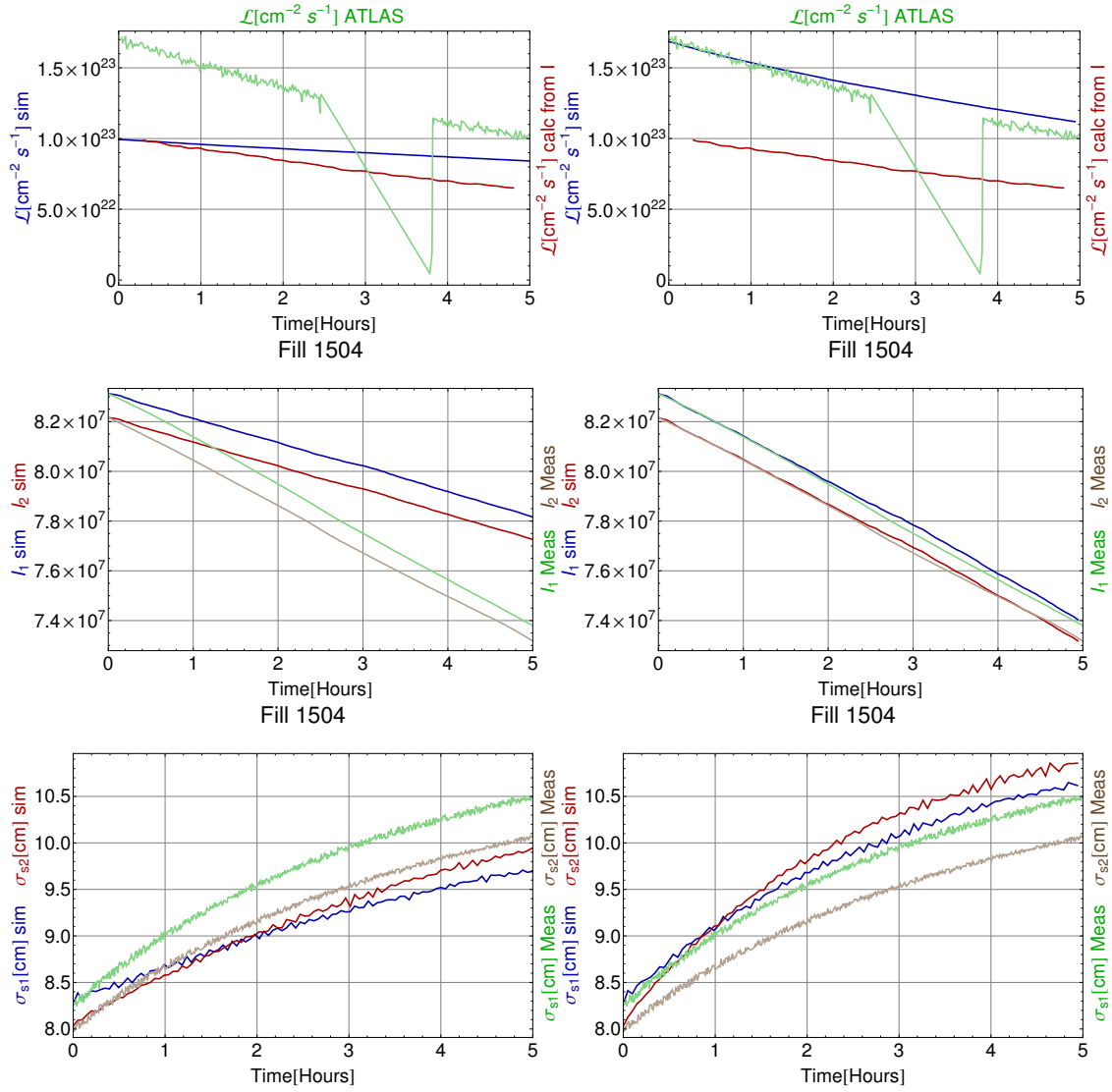


FIGURE D.6.1. Fill 1504-1

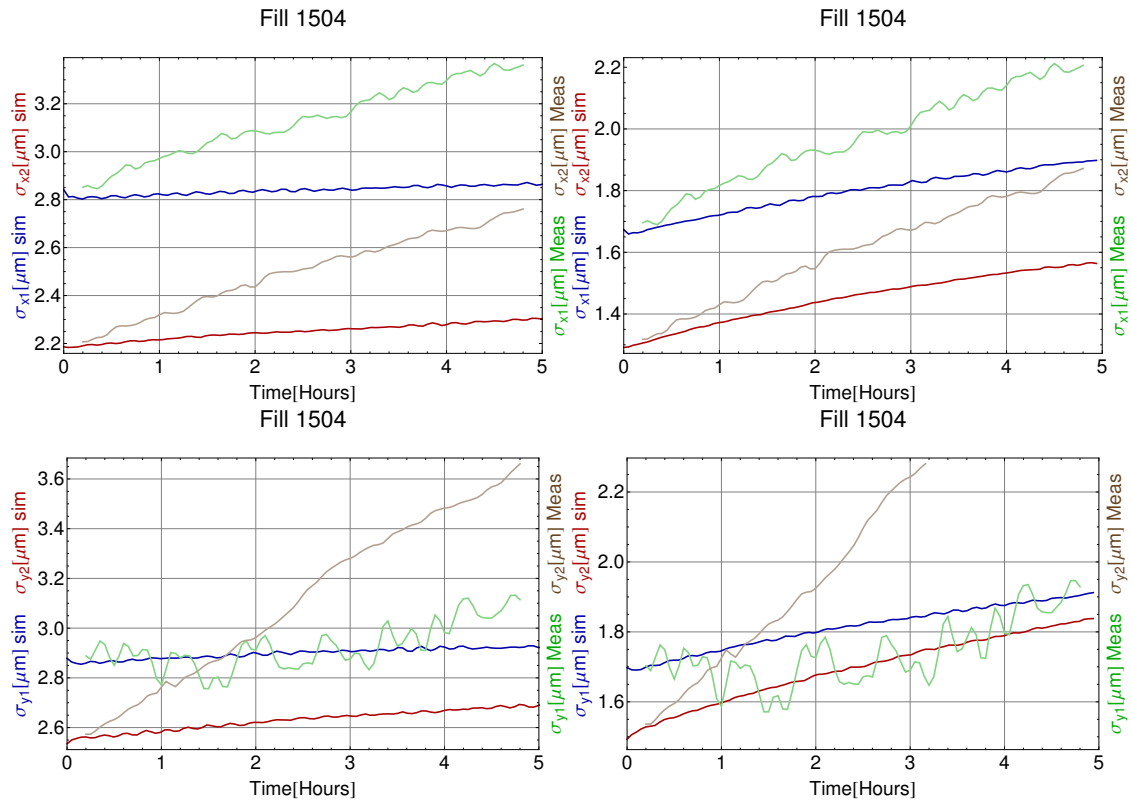


FIGURE D.6.2. Fill 1504-2

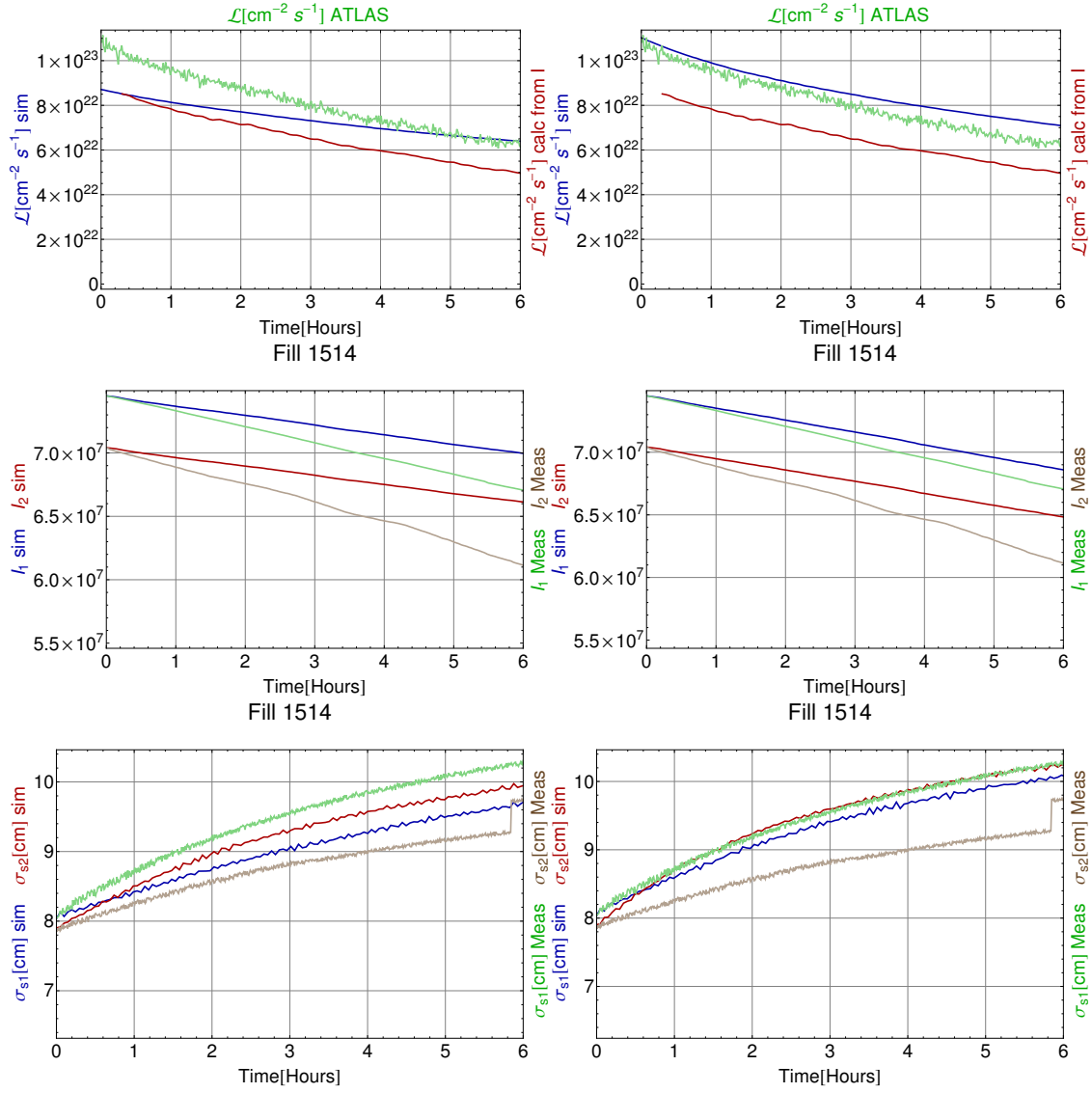


FIGURE D.6.3. Fill 1514-1

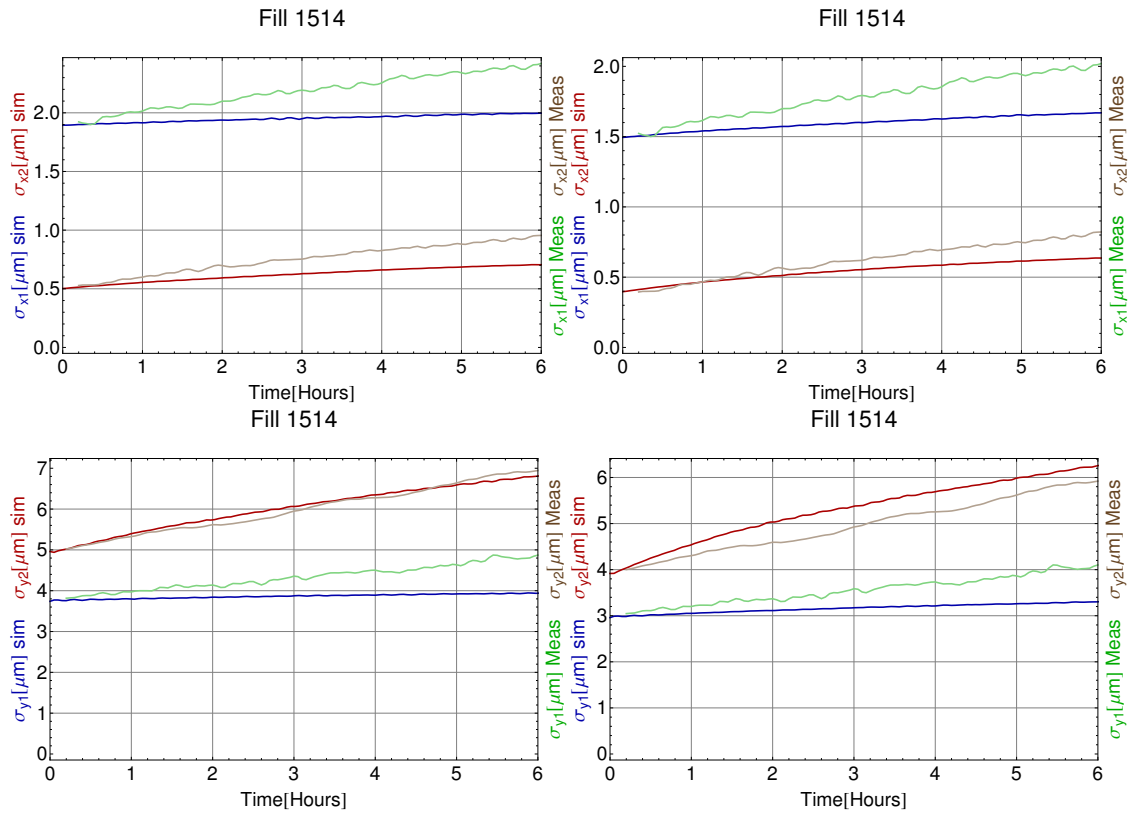


FIGURE D.6.4. Fill 1514-2